

CMS Draft Analysis Note

The content of this note is intended for CMS internal use and distribution only

2020/12/09

Archive Hash: 526beb7-D

Archive Date: 2020/12/09

Measurements of Higgs differential cross section and interpretations in $H \rightarrow ZZ \rightarrow 4\ell (\ell = e, \mu)$ channel

M. Bonanomi², M.S. Chen¹, Q.Y. Guo^{1,4}, T. Javaid^{1,4}, P. Milenovic⁵, V. Milosevic⁵, M. Ahmad⁷, C. Ochando², G. Ortona², R. Salerno², R. Sharma¹, T. Sculac³, and D. Sperka⁶

¹ IHEP, Beijing

² Laboratoire Leprince-Ringuet

³ University of Split

⁴ Beihang University

⁵ University of Belgrade

⁶ Boston University

⁷ Tsinghua University

Abstract

Properties of the Higgs boson are measured in the $H \rightarrow ZZ \rightarrow 4\ell (\ell = e, \mu)$ decay channel. A data sample of proton-proton collisions at a center-of-mass energy of 13 TeV is used, corresponding to an integrated luminosity of 137 fb^{-1} recorded by the CMS detector at the LHC. The fiducial cross section is measured with respect to several observables sensitive to production and decay of Higgs where the observed results are compared with POWHEG, MADGRAPH5 and NNLOPS theory predictions. The possible interpretations of the results are reported.

This box is only visible in draft mode. Please make sure the values below make sense.

PDFAuthor: Tahir Javaid

PDFTitle: Measurements of Higgs differential cross section and interpretations in HZZ4 "(=e,") channel

PDFSubject: CMS

PDFKeywords: CMS, your topics

Please also verify that the abstract does not use any user defined symbols

Acknowledgments**Contents**

1	Introduction	2
2	Datasets	3
2.1	Data	3
2.2	Simulation	7
3	Objects	10
3.1	Electrons	10
3.2	Muons	26
3.3	Photons for FSR recovery	36
3.4	Jets	36
3.5	Object Summary	41
4	Event Selection	43
4.1	Trigger Selection	43
4.2	Vertex Selection	43
4.3	ZZ Candidate Selection	43
4.4	Choice of the best ZZ Candidate	44
5	Background Estimation	45
5.1	Irreducible Backgrounds	45
5.2	Reducible Background	47
5.3	Rare Backgrounds	68
6	Signal Modelling	70
6.1	Signal modeling of the SM Higgs	70
7	Systematic uncertainties	72
7.1	Systematic uncertainties treatment when combining the data sets	73
8	Yields and distributions	74
8.1	Signal Region Yields	74
8.2	Signal Region Distributions	74
9	Results	78
9.1	Differential Cross Sections and EFT interpretations	79

31 1 Introduction

32 The ATLAS and CMS collaborations first reported the discovery of a new boson in 2012 [1,
 33 2] consistent with the standard model (SM) Higgs boson [3–8] based on proton-proton (pp)
 34 collisions delivered by the CERN LHC at a center-of-mass energy of $\sqrt{s} = 7\text{ TeV}$ in 2011 and
 35 8 TeV in 2012. Subsequent studies by CMS using the full LHC Run 1 data set in various decay
 36 channels and production modes and combined measurements from ATLAS and CMS [9–12]
 37 showed that the properties of the new boson are so far consistent with expectations for the SM
 38 Higgs boson.

39 The $H \rightarrow ZZ \rightarrow 4\ell$ decay channel ($\ell = e, \mu$) has a large signal-to-background ratio due to the
 40 complete reconstruction of the final state decay products and excellent lepton momentum res-
 41 olution and is one of the most important channels for studies of the Higgs boson’s properties.
 42 Measurements performed using this decay channel and the Run 1 data set include the deter-
 43 mination of the mass and spin-parity of the new boson [13–15], its width [16, 17] and fiducial
 44 cross sections [18], as well as tests for anomalous HVV couplings [15, 17].

45 This analysis note presents measurements of properties of the Higgs boson in the $H \rightarrow ZZ \rightarrow$
 46 4ℓ decay channel at $\sqrt{s} = 13\text{ TeV}$ using 137 fb^{-1} of pp collision data collected with the CMS
 47 experiment at the LHC in 2016, 2017 and 2018. Compared to the previous public result [19], the
 48 full available dataset has been fully re-analyzed, with several improvements:

- 49 • analysis of re-recoed 2016 data (17July2018 [20]) and v2 version of the Fall17MiniAOD
 50 for 2017 MC samples.
- 51 • estimation of rare backgrounds ($t\bar{t}+V$, $t\bar{t}+VV$, $VVV\dots$ where V stands for W or Z)
 52 from MC samples (see Section 5.3).
- 53 • development of a BDT combining identification and isolation observables to im-
 54 prove electron selection performance (2016), similar to what was already done for
 55 2017 and 2018 (see Section 3.1.2).
- 56 • improved measurement of lepton scale factors (see Sections 3.1.5, 3.2.5).
- 57 • in-depth studies of jets treatment (implementation of L1 pre-firing emulation for
 58 2016, 2017, removal of noisy jets in 2017, impact assessment of HEM 16/17 failures
 59 in 2018, new and improved Jet Energy Scale and Resolutions corrections for 2018),
 60 see Section 3.4.3.
- 61 • Jet PU-ID properly applied (only for jets with $30 < p_T < 50\text{ GeV}$) as recommended
 62 by the JetMET POG.
- 63 • DeepCSV b-tagging algorithm used for all three years.
- 64 • better binning for differential measurement (especially $p_T(H)$).
- 65 • several additional (production and as well as decay) observables studied with opti-
 66 mized binning.
- 67 • in addition to POWHEG AND NNLOPS, MADGRAPH5 IS USED AS ADDITIONAL
 68 THEORY PREDICTION TO FOR COMPARISON OF THE OBSERVED RESULTS.
- 69 • EFFECTIVE FIELD THEORY (EFT) INTERPRETATION OF DIFFERENTIAL MEASURE-
 70 MENTS ARE ALSO MADE.

2 Datasets

2.1 Data

2.1.1 Triggers and Datasets

This analysis uses a data sample recorded by the CMS experiment during 2016, 2017 and 2018, corresponding to 137 fb^{-1} of data.

The datasets used for 2016, 2017 and 2018 data taking are listed in Tables 1, 3, and 5, respectively, along with the integrated luminosity. The analysis relies on four different primary datasets (PDs), *DoubleMuon*, *MuEG*, *EGamma* (or *DoubleEG* and *SingleElectron* for 2016 and 2017), and *SingleMuon*, each of which combines a certain collections of HLT paths. To avoid duplicate events from different primary datasets, events are taken:

- from EGamma if they pass the diEle or triEle or singleElectron triggers,
- from DoubleMuon if they pass the diMuon or triMuon triggers and fail the diEle and triEle triggers,
- from MuEG if they pass the MuEle or MuDiEle or DiMuEle triggers and fail the diEle, triEle, singleElectron, diMuon and triMuon triggers,
- from SingleMuon if they pass the singleMuon trigger and fail all the above triggers.

The HLT paths used for 2016, 2017 and 2018 collision data are listed in Tables 2, 4 and 6, respectively.

Run-range	Dataset	Integrated luminosity
272007-275376	/DoubleMuon/Run2016B-17Jul2018-v1/MINIAOD /DoubleEG/Run2016B-17Jul2018-v1/MINIAOD /MuonEG/Run2016B-17Jul2018-v1/MINIAOD /SingleElectron/Run2016B-17Jul2018-v1/MINIAOD /SingleMuon/Run2016B-17Jul2018-v1/MINIAOD	5.892 fb^{-1}
275657-276283	/DoubleMuon/Run2016C-17Jul2018-v1/MINIAOD /DoubleEG/Run2016C-17Jul2018-v1/MINIAOD /MuonEG/Run2016C-17Jul2018-v1/MINIAOD /SingleElectron/Run2016C-17Jul2018-v1/MINIAOD /SingleMuon/Run2016C-17Jul2018-v1/MINIAOD	2.646 fb^{-1}
276315-276811	/DoubleMuon/Run2016D-17Jul2018-v1/MINIAOD /DoubleEG/Run2016D-17Jul2018-v1/MINIAOD /MuonEG/Run2016D-17Jul2018-v1/MINIAOD /SingleElectron/Run2016D-17Jul2018-v1/MINIAOD /SingleMuon/Run2016D-17Jul2018-v1/MINIAOD	4.353 fb^{-1}
276831-277420	/DoubleMuon/Run2016E-17Jul2018-v1/MINIAOD /DoubleEG/Run2016E-17Jul2018-v1/MINIAOD /MuonEG/Run2016E-17Jul2018-v1/MINIAOD /SingleElectron/Run2016E-17Jul2018-v1/MINIAOD /SingleMuon/Run2016E-17Jul2018-v1/MINIAOD	4.117 fb^{-1}
277772-278808	/DoubleMuon/Run2016F-17Jul2018-v1/MINIAOD /DoubleEG/Run2016F-17Jul2018-v1/MINIAOD /MuonEG/Run2016F-17Jul2018-v1/MINIAOD /SingleElectron/Run2016F-17Jul2018-v1/MINIAOD /SingleMuon/Run2016F-17Jul2018-v1/MINIAOD	3.186 fb^{-1}
278820-280385	/DoubleMuon/Run2016G-17Jul2018-v1/MINIAOD /DoubleEG/Run2016G-17Jul2018-v1/MINIAOD /MuonEG/Run2016G-17Jul2018-v1/MINIAOD /SingleElectron/Run2016G-17Jul2018-v1/MINIAOD /SingleMuon/Run2016G-17Jul2018-v1/MINIAOD	7.721 fb^{-1}
280919-284044	/DoubleMuon/Run2016H-17Jul2018-v1/MINIAOD /DoubleEG/Run2016H-17Jul2018-v1/MINIAOD /MuonEG/Run2016H-17Jul2018-v1/MINIAOD /SingleElectron/Run2016H-17Jul2018-v1/MINIAOD /SingleMuon/Run2016H-17Jul2018-v1/MINIAOD /DoubleMuon/Run2016H-17Jul2018-v1/MINIAOD /DoubleEG/Run2016H-17Jul2018-v1/MINIAOD /MuonEG/Run2016H-17Jul2018-v1/MINIAOD /SingleElectron/Run2016H-17Jul2018-v1/MINIAOD /SingleMuon/Run2016H-17Jul2018-v1/MINIAOD	8.857 fb^{-1}

Table 1: Datasets used in the 2016 analysis.

HLT path	prescale	primary dataset
HLT_Ele17_Ele12_CaloIdL_TrackIdL_IsoVL_DZ	1	DoubleEG
HLT_Ele23_Ele12_CaloIdL_TrackIdL_IsoVL_DZ	1	DoubleEG
HLT_DoubleEle33_CaloIdL_GsfTrkIdVL	1	DoubleEG
HLT_Ele16_Ele12_Ele8_CaloIdL_TrackIdL	1	DoubleEG
HLT_Mu17_TrkIsoVVL_Mu8_TrkIsoVVL	1	DoubleMuon
HLT_Mu17_TrkIsoVVL_TkMu8_TrkIsoVVL	1	DoubleMuon
HLT_TripleMu_12_10_5	1	DoubleMuon
HLT_Mu8_TrkIsoVVL_Ele17_CaloIdL_TrackIdL_IsoVL	1	MuonEG
HLT_Mu8_TrkIsoVVL_Ele23_CaloIdL_TrackIdL_IsoVL	1	MuonEG
HLT_Mu17_TrkIsoVVL_Ele12_CaloIdL_TrackIdL_IsoVL	1	MuonEG
HLT_Mu23_TrkIsoVVL_Ele12_CaloIdL_TrackIdL_IsoVL	1	MuonEG
HLT_Mu23_TrkIsoVVL_Ele8_CaloIdL_TrackIdL_IsoVL	1	MuonEG
HLT_Mu8_DiEle12_CaloIdL_TrackIdL	1	MuonEG
HLT_DiMu9_Ele9_CaloIdL_TrackIdL	1	MuonEG
HLT_Ele25_eta2p1_WPTight	1	SingleElectron
HLT_Ele27_WPTight	1	SingleElectron
HLT_Ele27_eta2p1_WPLoose_Gsf	1	SingleElectron
HLT_IsoMu20 OR HLT_IsoTkMu20	1	SingleMuon
HLT_IsoMu22 OR HLT_IsoTkMu22	1	SingleMuon

Table 2: Trigger paths used in 2016 collision data.

Run-range	Dataset	Integrated luminosity
297046-299329	/DoubleMuon/Run2017B-17Nov2017-v1/MINIAOD /DoubleEG/Run2017B-17Nov2017-v1/MINIAOD /MuonEG/Run2017B-17Nov2017-v1/MINIAOD /SingleElectron/Run2017B-17Nov2017-v1/MINIAOD /SingleMuon/Run2017B-17Nov2017-v1/MINIAOD	4.792 fb ⁻¹
299368-300676	/DoubleMuon/Run2017C-17Nov2017-v1/MINIAOD /DoubleEG/Run2017C-17Nov2017-v1/MINIAOD /MuonEG/Run2017C-17Nov2017-v1/MINIAOD /SingleElectron/Run2017C-17Nov2017-v1/MINIAOD /SingleMuon/Run2017C-17Nov2017-v1/MINIAOD	9.755 fb ⁻¹
302030-303434	/DoubleMuon/Run2017D-17Nov2017-v1/MINIAOD /DoubleEG/Run2017D-17Nov2017-v1/MINIAOD /MuonEG/Run2017D-17Nov2017-v1/MINIAOD /SingleElectron/Run2017D-17Nov2017-v1/MINIAOD /SingleMuon/Run2017D-17Nov2017-v1/MINIAOD	4.319 fb ⁻¹
303824-304797	/DoubleMuon/Run2017E-17Nov2017-v1/MINIAOD /DoubleEG/Run2017E-17Nov2017-v1/MINIAOD /MuonEG/Run2017E-17Nov2017-v1/MINIAOD /SingleElectron/Run2017E-17Nov2017-v1/MINIAOD /SingleMuon/Run2017E-17Nov2017-v1/MINIAOD	9.424 fb ⁻¹
305040-306462	/DoubleMuon/Run2017F-17Nov2017-v1/MINIAOD /DoubleEG/Run2017F-17Nov2017-v1/MINIAOD /MuonEG/Run2017F-17Nov2017-v1/MINIAOD /SingleElectron/Run2017F-17Nov2017-v1/MINIAOD /SingleMuon/Run2017F-17Nov2017-v1/MINIAOD	13.50 fb ⁻¹
278820-280385	/DoubleMuon/Run2017G-PromptReco-v1/MINIAOD /DoubleEG/Run2017G-PromptReco-v1/MINIAOD /MuonEG/Run2017G-PromptReco-v1/MINIAOD /SingleElectron/Run2017G-PromptReco-v1/MINIAOD /SingleMuon/Run2017G-PromptReco-v1/MINIAOD	7.721 fb ⁻¹
281207-284068	/DoubleMuon/Run2017H-PromptReco-v1/MINIAOD /DoubleEG/Run2017H-PromptReco-v1/MINIAOD /MuonEG/Run2017H-PromptReco-v1/MINIAOD /SingleElectron/Run2017H-PromptReco-v1/MINIAOD /SingleMuon/Run2017H-PromptReco-v1/MINIAOD /DoubleMuon/Run2017H-PromptReco-v2/MINIAOD /DoubleEG/Run2017H-PromptReco-v2/MINIAOD /MuonEG/Run2017H-PromptReco-v2/MINIAOD /SingleMuon/Run2017H-PromptReco-v2/MINIAOD /DoubleMuon/Run2017H-PromptReco-v3/MINIAOD /DoubleEG/Run2017H-PromptReco-v3/MINIAOD /MuonEG/Run2017H-PromptReco-v3/MINIAOD /SingleElectron/Run2017H-PromptReco-v3/MINIAOD /SingleMuon/Run2017H-PromptReco-v3/MINIAOD	8.857 fb ⁻¹

Table 3: Datasets used in the 2017 analysis.

HLT path	prescale	primary dataset
HLT_Ele23_Ele12_CaloIdL_TrackIdL_IsoVL_*	1	DoubleEG
HLT_DoubleEle33_CaloIdL_GsfTrkIdVL	1	DoubleEG
HLT_Ele16_Ele12_Ele8_CaloIdL_TrackIdL	1	DoubleEG
HLT_Mu17_TrkIsoVVL_Mu8_TrkIsoVVL_DZ_Mass3p8	1	DoubleMuon
HLT_Mu17_TrkIsoVVL_Mu8_TrkIsoVVL_DZ_Mass8	1	DoubleMuon
HLT_TripleMu_12_10_5	1	DoubleMuon
HLT_TripleMu_10_5_5_D2	1	DoubleMuon
HLT_Mu23_TrkIsoVVL_Ele12_CaloIdL_TrackIdL_IsoVL	1	MuonEG
HLT_Mu8_TrkIsoVVL_Ele23_CaloIdL_TrackIdL_IsoVL_DZ	1	MuonEG
HLT_Mu12_TrkIsoVVL_Ele23_CaloIdL_TrackIdL_IsoVL_DZ	1	MuonEG
HLT_Mu23_TrkIsoVVL_Ele12_CaloIdL_TrackIdL_IsoVL_DZ	1	MuonEG
HLT_DiMu9_Ele9_CaloIdL_TrackIdL_DZ	1	MuonEG
HLT_Mu8_DiEle12_CaloIdL_TrackIdL	1	MuonEG
HLT_Mu8_DiEle12_CaloIdL_TrackIdL_DZ	1	MuonEG
HLT_Ele35_WPTight_Gsf_v*	1	SingleElectron
HLT_Ele38_WPTight_Gsf_v*	1	SingleElectron
HLT_Ele40_WPTight_Gsf_v*	1	SingleElectron
HLT_IsoMu27	1	SingleMuon

Table 4: Trigger paths used in 2017 collision data.

Run-range	Dataset	Integrated luminosity
315252-316995	/DoubleMuon/Run2018A-17Sep2018-v2/MINIAOD /MuonEG/Run2018A-17Sep2018-v1/MINIAOD /EGamma/Run2018A-17Sep2018-v2/MINIAOD /SingleMuon/Run2018A-17Sep2018-v2/MINIAOD	X.XXX fb ⁻¹
317080-319310	/DoubleMuon/Run2018B-17Sep2018-v1/MINIAOD /MuonEG/Run2018B-17Sep2018-v1/MINIAOD /EGamma/Run2018B-17Sep2018-v1/MINIAOD /SingleMuon/Run2018B-17Sep2018-v1/MINIAOD	X.XXX fb ⁻¹
319337-320065	/DoubleMuon/Run2018C-17Sep2018-v1/MINIAOD /MuonEG/Run2018C-17Sep2018-v1/MINIAOD /EGamma/Run2018C-17Sep2018-v1/MINIAOD /SingleMuon/Run2018C-17Sep2018-v1/MINIAOD	X.XXX fb ⁻¹
320673-325175	/DoubleMuon/Run2018D-PromptReco-v2/MINIAOD /MuonEG/Run2018D-PromptReco-v2/MINIAOD /EGamma/Run2018D-PromptReco-v2/MINIAOD /SingleMuon/Run2018D-PromptReco-v2/MINIAOD	X.XXX fb ⁻¹

Table 5: Datasets used in the 2018 analysis.

HLT path	prescale	primary dataset
HLT_Ele23_Ele12_CaloIdL_TrackIdL_IsoVL_v*	1	DoubleEG
HLT_DoubleEle25_CaloIdL_MW_v*	1	DoubleEG
HLT_Mu17_TrkIsoVVL_Mu8_TrkIsoVVL_DZ_Mass3p8_v*	1	DoubleMuon
HLT_Mu23_TrkIsoVVL_Ele12_CaloIdL_TrackIdL_IsoVL_v*	1	MuonEG
HLT_Mu8_TrkIsoVVL_Ele23_CaloIdL_TrackIdL_IsoVL_DZ_v*	1	MuonEG
HLT_Mu12_TrkIsoVVL_Ele23_CaloIdL_TrackIdL_IsoVL_DZ_v*	1	MuonEG
HLT_DiMu9_Ele9_CaloIdL_TrackIdL_DZ_v*	1	MuonEG
HLT_Ele32_WPTight_Gsf_v*	1	SingleElectron
HLT_IsoMu24_v*	1	SingleMuon

Table 6: Trigger paths used in 2018 collision data.

2.1.2 Trigger Efficiency

The efficiency in data of the combination of triggers used in the analysis with respect to the offline reconstruction and selection is measured by considering 4ℓ events triggered by single lepton triggers. One of the four reconstructed leptons (the “tag”) is geometrically matched to a trigger object passing the final filter of one of the single muon or single electron triggers. The other three leptons are used as “probes”. In each 4ℓ event there are up to 4 possible tag-probe combinations, and all possible combinations are counted in the denominator of the efficiency. For each of the three probe leptons all matching trigger filter objects are collected. Then the matched trigger filter objects of the three probe leptons are combined in attempt to reconstruct any of the triggers used in the analysis. If any of the analysis triggers can be formed using the probe leptons, the set of probes is also counted in the numerator of the efficiency.

This method does not have a perfect closure in MC events due to the fact that the presence of a fourth lepton increases the trigger efficiency, and this effect is not accounted for. Also, in the $2e2\mu$ final state, the three probe leptons cannot be combined to form all possible triggers which can collect events with two electrons and two muons (e.g. if the tag lepton is an electron, the three remaining leptons cannot pass a double electron trigger). Therefore the method is also applied on MC and the difference between data and MC is used to determine the reliability of the simulation. The efficiency plotted as a function of the minimum p_T of the three probe leptons in data and MC using this method can be seen in Fig. 1 that shows the trigger efficiency in 2018 data for different final states. The MC efficiency describes well the data within the statistical uncertainties.

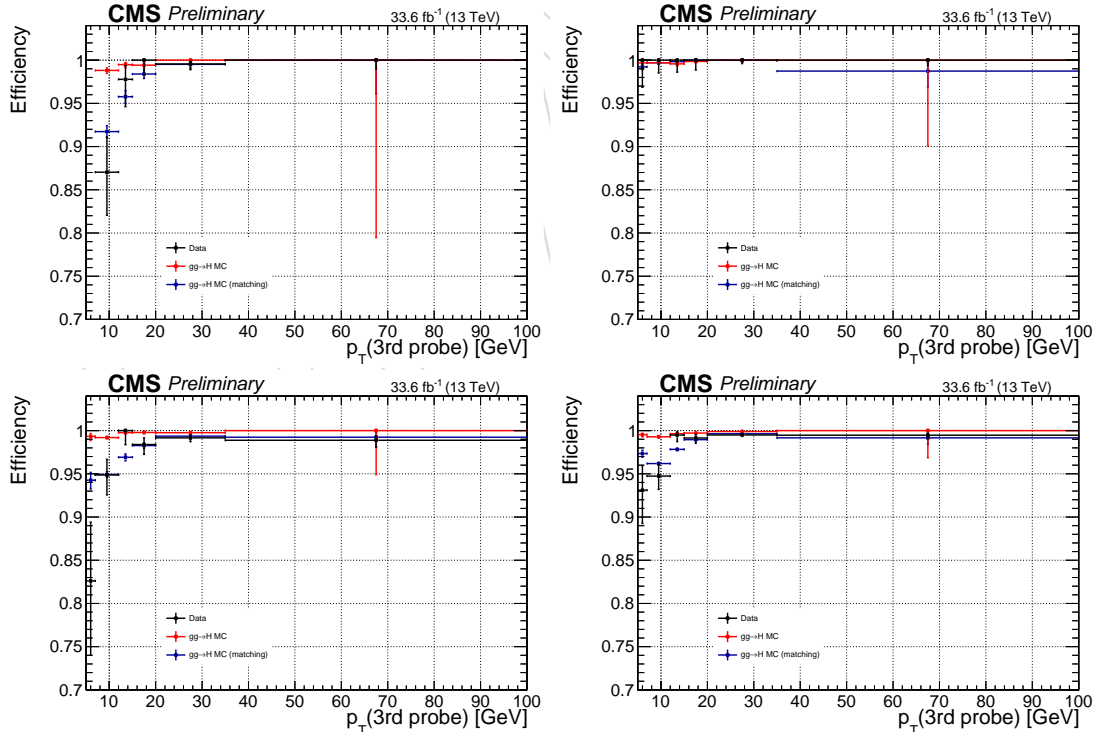


Figure 1: Trigger efficiency measured in 2016 data using 4ℓ events collected by single lepton triggers for the $4e$ (top left), 4μ (top right), $2e2\mu$ (bottom left) and 4ℓ (bottom right) final states.

A summary of the trigger efficiencies in MC truth, and in MC and data using the tag and probe method are summarized in table 7. The trigger efficiency in simulation is found to be $> 99\%$ in

112 each final state.

Final State	$gg \rightarrow H$ MC	$gg \rightarrow H$ MC (matching)	Data (matching)
$4e$	$0.991^{+.002}_{-.002}$	$0.948^{+.004}_{-.004}$	$0.982^{+.005}_{-.007}$
4μ	$0.997^{+.001}_{-.001}$	$0.997^{+.001}_{-.001}$	$1.000^{+.000}_{-.001}$
$2e2\mu$	$0.995^{+.001}_{-.001}$	$0.964^{+.002}_{-.002}$	$0.983^{+.003}_{-.004}$

Table 7: Trigger efficiencies measured using 4ℓ events in 2018 data.

113 2.2 Simulation

114 2.2.1 Signal Samples

115 Descriptions of the SM Higgs boson production are obtained using the POWHEG V2 [21–23]
 116 generator for the five main production modes: gluon fusion ($gg \rightarrow H$) including quark mass
 117 effects [24], vector boson fusion (VBF) [25], and associated production (WH, ZH and $t\bar{t} H$ [26]).
 118 In the case of WH and ZH the MiNLO HVJ extension of POWHEG is used [27]. The description
 119 of the decay of the Higgs boson to four leptons is obtained using the JHUGEN generator [28]. In
 120 the case of WH, ZH and $t\bar{t} H$, the Higgs boson is allowed to decay to $H \rightarrow ZZ \rightarrow 2\ell^2X$ such that
 121 4-lepton events where two leptons originate from the decay of associated Z, W bosons or top
 122 quarks are also taken into account in the simulation. Showering of parton-level events is done
 123 using PYTHIA8.209, and in all cases matching is performed by allowing QCD emissions at all
 124 energies in the shower and vetoing them afterwards according to the POWHEG internal scale.
 125 All samples are generated with the NNPDF 3.1 NLO parton distribution functions (PDFs) [29].
 126 The list of signal samples and their cross sections are shown in Table 8.

127 2.2.2 Background Samples

128 Production of ZZ via quark-antiquark annihilation is generated at next-to-leading order (NLO)
 129 using POWHEG V2 [30] and PYTHIA8, with the same settings as for the Higgs signal. As this
 130 simulation covers a large range of ZZ invariant masses, dynamical QCD factorization and
 131 renormalization scales have been chosen, equal to m_{ZZ} .

132 The $gg \rightarrow ZZ$ process is simulated at leading order (LO) with MCFM [31, 32]. In order to match
 133 the $gg \rightarrow H \rightarrow ZZ$ transverse momentum spectra predicted by POWHEG at NLO, the showering
 134 for MCFM samples is performed with different PYTHIA8 settings, allowing only emissions up
 135 to the parton-level scale (“wimpy” shower).

136 Although not directly used to model data observations, additional MC samples of WZ, Drell-
 137 Yan+jets, $t\bar{t}$, and tribosons are generated using MADGRAPH5_AMCATNLO [33] either inclu-
 138 sively or merging several jet multiplicities, as detailed in the table. Table 9 summarizes the MC
 139 simulation datasets used for this analysis.

Process	Dataset Name	$\sigma \times BR(\times \epsilon_{\text{filter}})$
$gg \rightarrow H \rightarrow ZZ \rightarrow 4\ell$	/GluGluHToZZTo4L_M125_13TeV_powheg2_JHUGenV709_pythia8/[1]	12.18 fb
$qq \rightarrow Hqq \rightarrow ZZqq \rightarrow 4\ell qq$	/VBF_HToZZTo4L_M125_13TeV_powheg2_JHUGenV709_pythia8/[1]	1.044 fb
$q\bar{q} \rightarrow W^+H \rightarrow W^+ZZ \rightarrow 4\ell + X$	/WplusH_HToZZTo4L_M125_13TeV_powheg2-minlo-HWJ_JHUGenV709_pythia8/[1]	0.232 fb
$q\bar{q} \rightarrow W^-H \rightarrow W^-ZZ \rightarrow 4\ell + X$	/WminusH_HToZZTo4L_M125_13TeV_powheg2-minlo-HWJ_JHUGenV709_pythia8/[1]	0.147 fb
$q\bar{q} \rightarrow ZH \rightarrow ZZZ \rightarrow 4\ell + X$	/ZH_HToZZ_4LFilter_M125_13TeV_powheg2-minlo-HZJ_JHUGenV709_pythia8/[1]	0.668 fb
$gg \rightarrow ttH \rightarrow ttZZ \rightarrow 4\ell + X$	/ttH_HToZZ_4LFilter_M125_13TeV_powheg_JHUGenV709_pythia8/[1]	0.393 fb
$gg \rightarrow bbH \rightarrow bbZZ \rightarrow 4\ell + X$	/bbH_HToZZTo4L_M125_13TeV_JHUGenV7011_pythia8/[1]	0.135 fb
$q\bar{q}/qg \rightarrow tHq \rightarrow tqZZ \rightarrow 4\ell + X$	/tqH_HToZZTo4L_M125_13TeV_JHUGenV7011_pythia8/[1]	0.0213 fb

[1] RunIIAutumn18MiniAOD-102X_upgrade2018_realistic_v15

Table 8: Signal Monte Carlo samples and cross sections.

Process	Dataset Name	$\sigma \cdot BR$
$qq \rightarrow ZZ \rightarrow 4\ell$	/ZZTo4L_13TeV_powheg_pythia8/[1]	1.256 pb
$qq \rightarrow ZZ \rightarrow 4\ell$	/ZZTo4L_13TeV-amcatnloFXFX-pythia8/[1]	1.212 pb
$gg \rightarrow ZZ \rightarrow 4e$	/GluGluToContinToZZTo4e_13TeV_MCFM701/[1]	0.00159 pb
$gg \rightarrow ZZ \rightarrow 4\mu$	/GluGluToContinToZZTo4mu_13TeV_MCFM701/[1]	0.00159 pb
$gg \rightarrow ZZ \rightarrow 4\tau$	/GluGluToContinToZZTo4tau_13TeV_MCFM701/[1]	0.00159 pb
$gg \rightarrow ZZ \rightarrow 2e2\mu$	/GluGluToContinToZZTo2e2mu_13TeV_MCFM701/[1]	0.00319 pb
$gg \rightarrow ZZ \rightarrow 2e2\tau$	/GluGluToContinToZZTo2e2tau_13TeV_MCFM701/[1]	0.00319 pb
$gg \rightarrow ZZ \rightarrow 2\mu2\tau$	/GluGluToContinToZZTo2mu2tau_13TeV_MCFM701/[1]	0.00319 pb
$Z \rightarrow \ell\ell + \text{jets}$	/DYJetsToLL_M-50.TuneCUETP8M1_13TeV-amcatnloFXFX-pythia8/[1]	6104 pb
$Z \rightarrow \ell\ell + \text{jets}$	/DYJetsToLL_M-10to50.TuneCUETP8M1_13TeV-amcatnloFXFX-pythia8/[1]	18610 pb
$WZ \rightarrow 3\ell\nu$	/WZTo3LNu_TuneCUETP8M1_13TeV-powheg-pythia8/[1]	4.430 pb
$t\bar{t}$	/TTJets_TuneCUETP8M1_13TeV-amcatnloFXFX-pythia8/[1]	815.96 pb
$t\bar{t} \rightarrow 2\ell 2\nu 2b$	/TTTo2L2Nu_13TeV-powheg/[1]	87.31 pb
ZZZ	/ZZZ_TuneCUETP8M1_13TeV-amcatnlo-pythia8/[1]	0.01398 pb
WZZ	/WZZ_TuneCUETP8M1_13TeV-amcatnlo-pythia8/[1]	0.05565 pb
WWZ	/WWZ_TuneCUETP8M1_13TeV-amcatnlo-pythia8/[1]	0.1651 pb
$t\bar{t}+ZZ$	/TTZZ_TuneCUETP8M2T4_13TeV-madgraph-pythia8/[1]	0.001572 pb
$t\bar{t}+WW$	/TTWW_TuneCUETP8M2T4_13TeV-madgraph-pythia8/[1]	0.007883 pb
$t\bar{t}+Z$	/ttZJets_13TeV_madgraphMLM/[1]	0.259 pb

where [1] = RunIIISummer16MiniAODv3-PUMoriond17_94X_mcRun2_asymptotic_v* for 2016,

[1] = RunIIFall17MiniAODv2-PU2017_12Apr2018_94X_mc2017_realistic_v* for 2017,

[1] = RunIIIAutumn18MiniAOD-102X_upgrade2018_realistic_v1* for 2018.

Table 9: Background Monte Carlo samples and cross sections.

140 2.2.3 Pileup Reweighting

- 141 For each year, corresponding simulation samples are reweighted to match the pileup distribution
 142 in data, as shown on the Fig. 2. The minimum bias cross-section used for each year is 69.2
 143 mb.

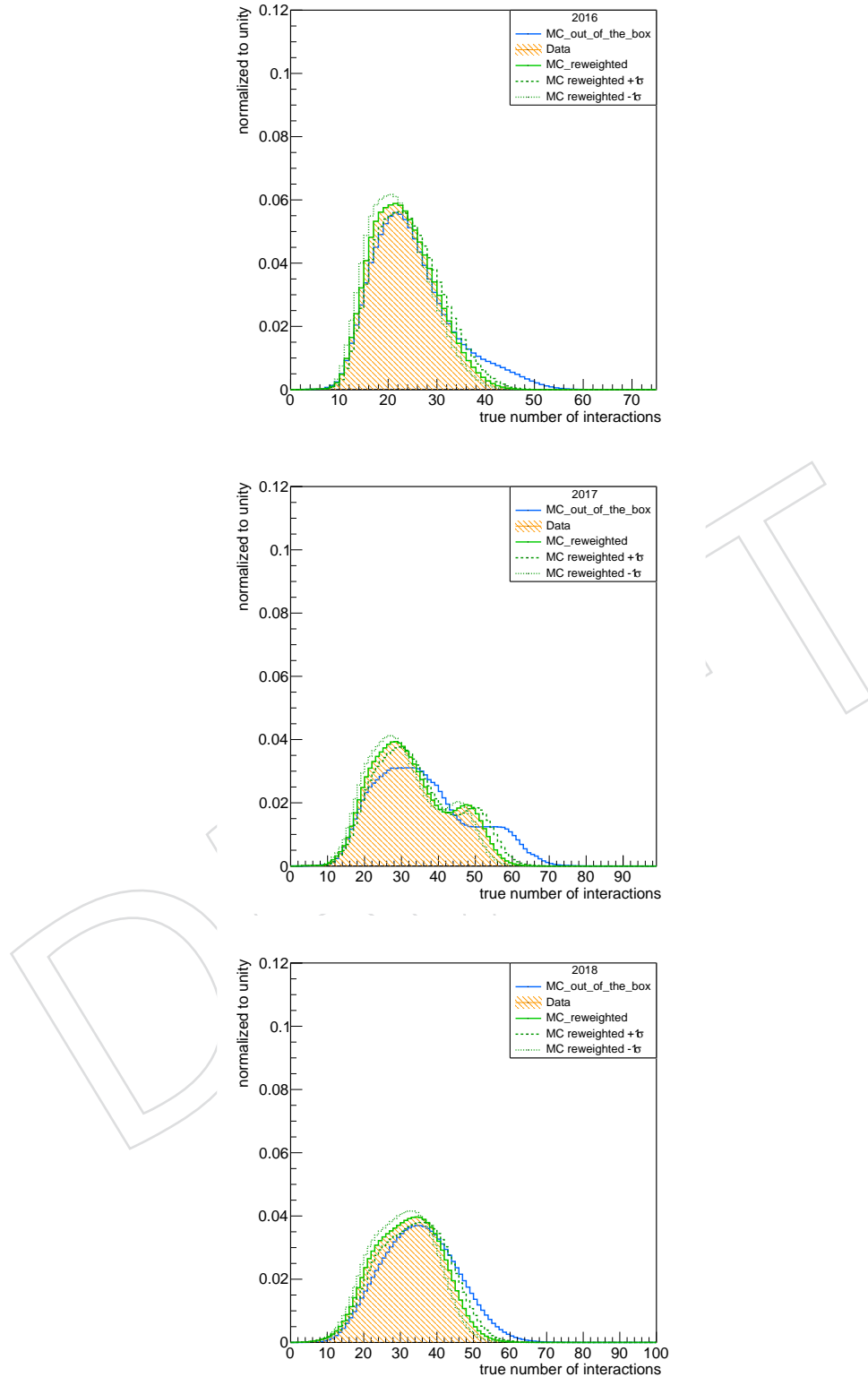


Figure 2: Distribution of pileup in 2016 (top), 2017 (middle) and 2018 (bottom) MC and Data shown before and after the application of PU weights. Up and down variations of 5% in the minimum bias cross section when calculating the weights are also shown.

144 **3 Objects**

145 The reconstruction of the SM Higgs boson in the decay chain $H \rightarrow ZZ \rightarrow 4\ell$ requires very
146 efficient lepton reconstruction and identification in order to be sensitive to a low mass Higgs,
147 for which at least one of the leptons has a p_T within the range 5 - 15 GeV. In this kinematic
148 region the need is for an optimal efficiency, while retaining the rate of misidentified leptons
149 low enough. On the same time, to allow a precise measurement of the Higgs boson mass and
150 together properties, which depend on the lepton kinematics, the analysis needs a precise mo-
151 mentum measurement. For both reasons, the analysis will make use of high statistics sources
152 of prompt leptons to measure efficiency, mis-identification rate, and energy scale/resolution.
153 In this chapter we describe the selection of leptons and jets and the calibrations done on data
154 control samples relevant for this analysis.

155 **3.1 Electrons**

156 **3.1.1 Electron Reconstruction**

157 More details on electron reconstruction can be found in Ref. [34].

158 Electron candidates are preselected using loose cuts on track-cluster matching observables, so
159 as to preserve the highest possible efficiency while rejecting part of the QCD background. To be
160 considered for the analysis, electrons are required to have a transverse momentum $p_T^e > 7$ GeV,
161 a reconstructed $|\eta^e| < 2.5$, and to satisfy a loose primary vertex constraint defined as $d_{xy} < 0.5$
162 cm and $d_z < 1$ cm. Such electrons are called **loose electrons**.

163 The data-MC discrepancy is corrected using scale factors as is done for the electron selection
164 with data efficiencies measured using the same tag-and-probe technique outlined later (see
165 Section 3.1.5). These studies for reconstructions are carried out by the EGM POG and the results
166 are only summarised here.

167 The electron reconstruction scale factors are shown Fig. 3 and are applied as a function of the
168 super cluster η and electron p_T .

169 **3.1.2 Electron Identification and Isolation**

170 One of the main improvements brought in the analysis is the usage of a new multivariate dis-
171 criminant for electron selection in all data taking periods.

172 Reconstructed electrons are now identified and isolated by means of an eXtreme Gradient
173 Boosting (XGBoost) optimized distributed gradient boosting library designed to be highly ef-
174 ficient, flexible and portable. It implements machine learning algorithms under the Gradient
175 Boosting framework and exploits observables from the electromagnetic cluster, the matching
176 between the cluster and the electron track, observables based exclusively on tracking measure-
177 ments as well as particle flow isolation sums. The full list of used features can be found in the
178 Table 10.

179 The model is trained on 2016, 2017, and 2018 Drell-Yan with jets MC sample for both signal and
180 background. The separate training for three periods guarantees optimal performance during
181 the whole Run 2 data taking period. The simulated samples used to train the model are listed
182 bellow.

183 • 2016

184 /DYJetsToLL_M-50_TuneCUETP8M1_13TeV-amcatnloFXFX-pythia8/RunIIISummer16MiniaO

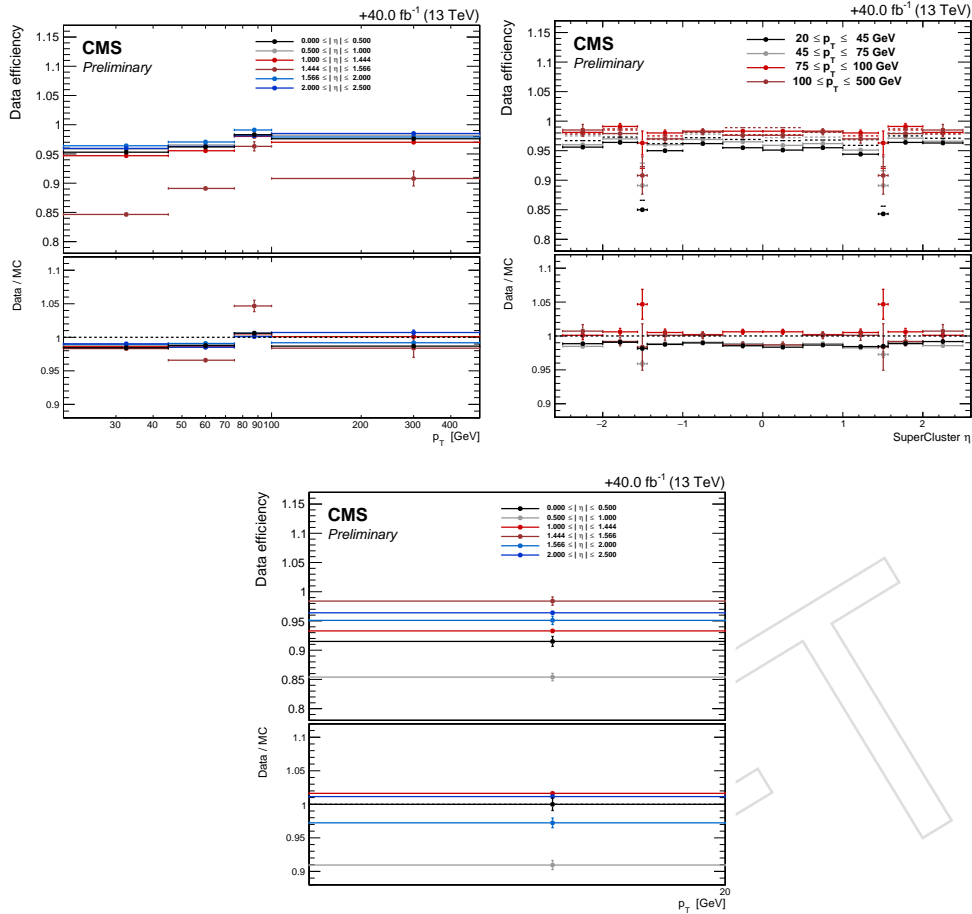


Figure 3: Electron reconstruction efficiencies efficiency in data versus p_T (left) and η (right) for electrons with $p_T > 20$ GeV (top) and $p_T < 20$ GeV (bottom) with corresponding data/MC scale factors as provided by the EGM POG. Errors are statistical only.

• 2017

/DYJetsToLL_M-50_TuneCP5_13TeV-madgraphMLM-pythia8/RunIIFall17MiniAOD-RECO

• 2018

/DYJetsToLL_M-50_TuneCP5_13TeV-madgraphMLM-pythia8/RunIIAutumn18MiniAOD-102X

Several studies have been conducted on 2016 Drell-Yan with jets MC sample. The XGBoost framework was first used in 2017 and the model was trained on 2017 Drell-Yan with jets MC sample. This model is known as 2017 ID+ISO V2. The same framework was then used to train the model on 2016 MC (2016 ID+ISO) and finally on 2018 MC (2018 ID+ISO). In Fig. 4 one can see the ROC curves obtained using 2016 Drell-Yan with jets MC sample. As expected, the model trained on 2016 MC using electron identification and isolation features outperforms the model trained on 2016 MC using only identification features and the model obtained after applying 2017 ID+ISO V2 training on 2016 Drell-Yan with jets MC sample.

In Fig. 5 one can see the ROC curve for the model trained on 2016 MC using electron identification and isolation features and ROC curve when applying sequential approach meaning applying isolation cut after cutting on the distribution obtained by training using only identification features. As expected, the model obtained using electron identification and isolation

201 features outperforms the sequential approach model.

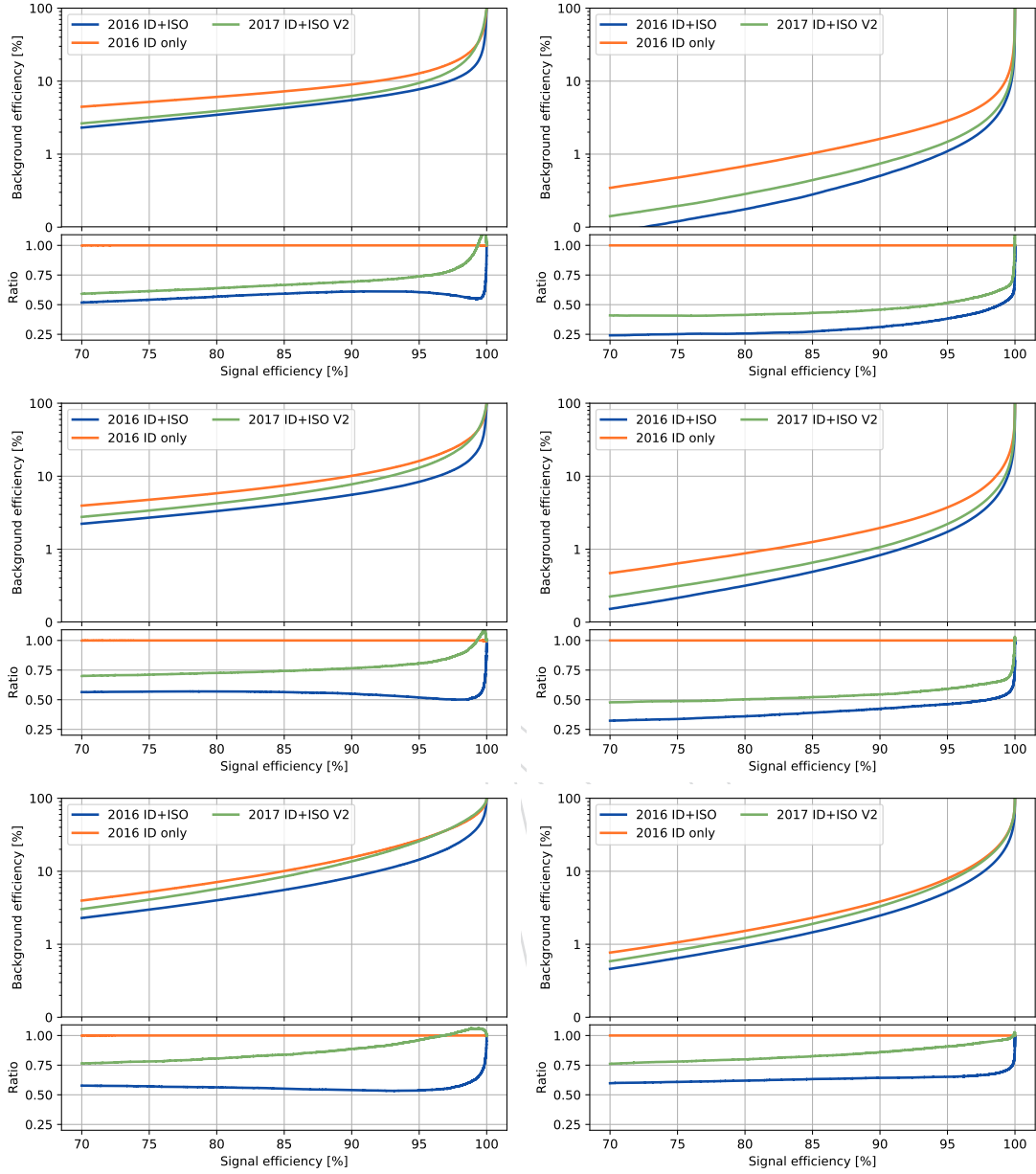


Figure 4: The receiver operating characteristic curves, representing the background efficiency vs signal efficiency, of the MVA trained on 2016 Drell-Yan with jets MC sample. Performance are shown for electrons with $5 < p_T < 10$ GeV (left), $p_T > 10$ GeV (right), and $|\eta| < 0.8$ (top), $0.8 < |\eta| < 1.479$ (middle), and $|\eta| > 1.479$ (bottom).

202 The Fig. 6 shows output of the multiclassifier discriminant i.e. MVA score for prompt electrons
 203 from Drell-Yan events and misidentified electrons originating from jets in Drell-Yan events. The
 204 performance of model trained on 2018 MC using electron identification and isolation features
 205 outperforms the model obtained after applying 2017 ID+ISO V2 training on 2018 Drell-Yan
 206 with jets MC sample as shown in Fig. 7.

207 The impact of the transition from the TMVA (V1) to the XGBoost(V2) training framework is
 208 shown in Fig. 8, showing a noticeable improvement.

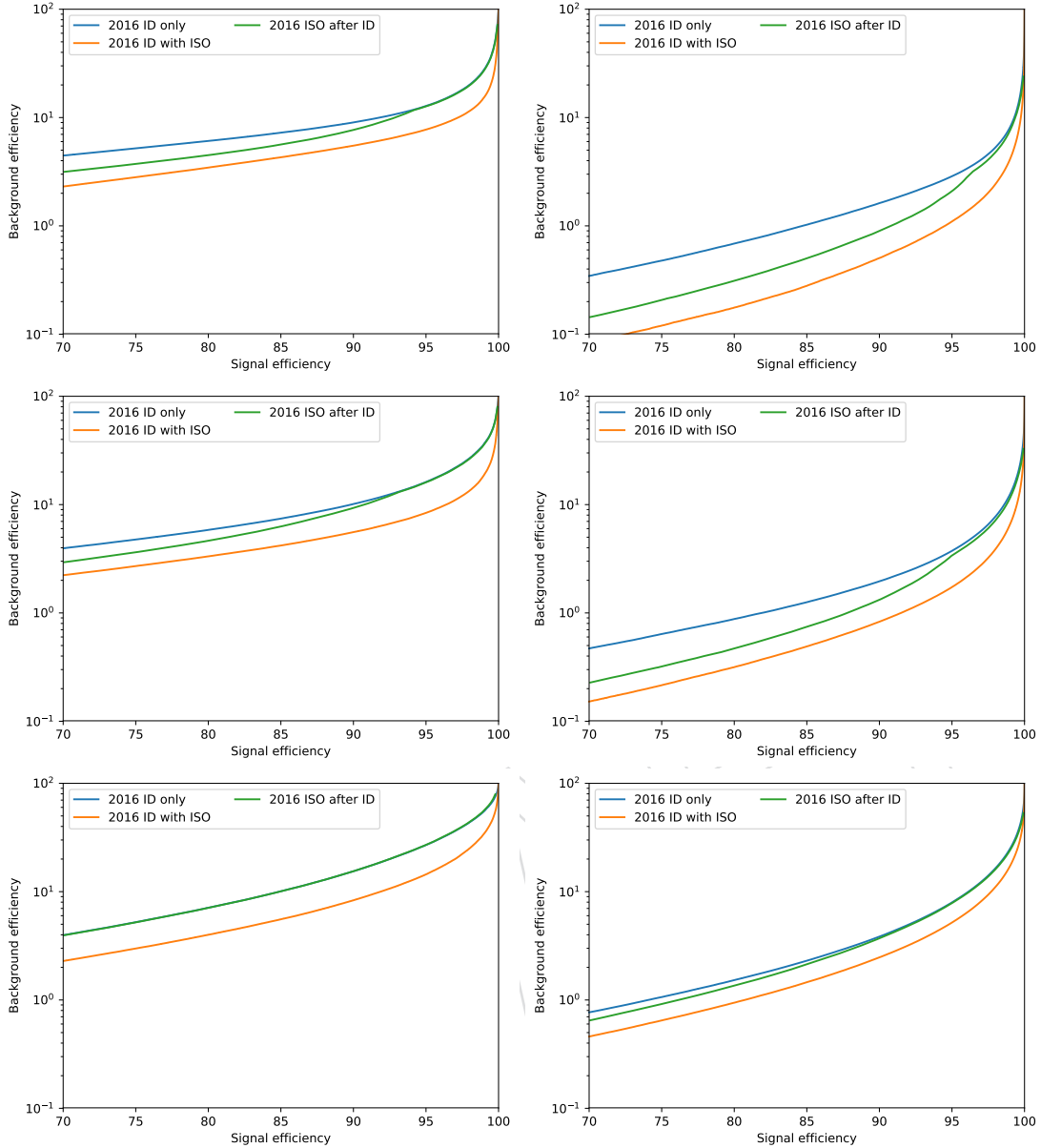


Figure 5: The receiver operating characteristic curves, representing the background efficiency vs signal efficiency, of the MVA trained on 2016 Drell-Yan with jets MC sample. Performance are shown for electrons with $5 < p_T < 10$ GeV (left), $p_T > 10$ GeV (right), and $|\eta| < 0.8$ (top), $0.8 < |\eta| < 1.479$ (middle), and $|\eta| > 1.479$ (bottom).

Tables 11, 12 and 13 list the cuts values applied to the MVA output for 2016, 2017, 2018 training, respectively. For 2018, the corresponding signal and background efficiencies are given as examples. They are very similar for 2016 and 2017. For the analysis, loose electrons have to pass this MVA identification and isolation working point.

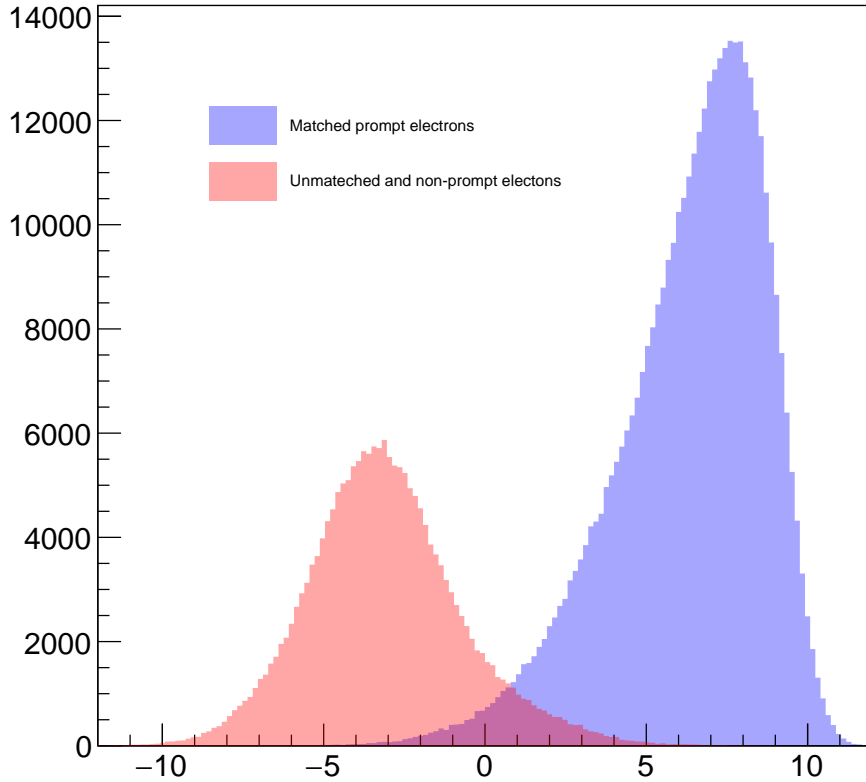


Figure 6: The Output of the multiclassifier discriminant for prompt electrons matched to truth electrons from Z decay (blue) and for misidentified electrons (red). Events are all taken from Drell-Yan with jets MC sample.

Observable type	Observable name
Cluster shape	RMS of the energy-crystal number spectrum along η and ϕ ; $\sigma_{i\eta i\eta}, \sigma_{i\phi i\phi}$
	Super cluster width along η and ϕ
	Ratio of the hadronic energy behind the electron supercluster to the supercluster energy, H/E
	Circularity $(E_{5\times 5} - E_{5\times 1})/E_{5\times 5}$
Track-cluster matching	Sum of the seed and adjacent crystal over the super cluster energy R_9
	For endcap traing bins: energy fraction in pre-shower $E_{\text{PS}}/E_{\text{raw}}$
	Energy-momentum agreement $E_{\text{tot}}/p_{in}, E_{\text{ele}}/p_{out}, 1/E_{\text{tot}} - 1/p_{in}$
tracking	Position matching $\Delta\eta_{in}, \Delta\varphi_{in}, \Delta\eta_{seed}$
	Fractional momentum loss $f_{\text{brem}} = 1 - p_{out}/p_{in}$
	Number of hits of the KF and GSF track N_{KF}, N_{GSF}
	Reduced χ^2 of the KF and GSF track $\chi^2_{KF}, \chi^2_{GSF}$
isolation	Number of expected but missing inner hits
	Probability transform of conversion vertex fit χ^2
	Particle Flow photon isolation sum
For PU-resilience	Particle Flow charged hadrons isolation sum
	Particle Flow neutral hadrons isolation sum
	Mean energy density in the event: ρ

Table 10: Overview of input features to the identification classifier.

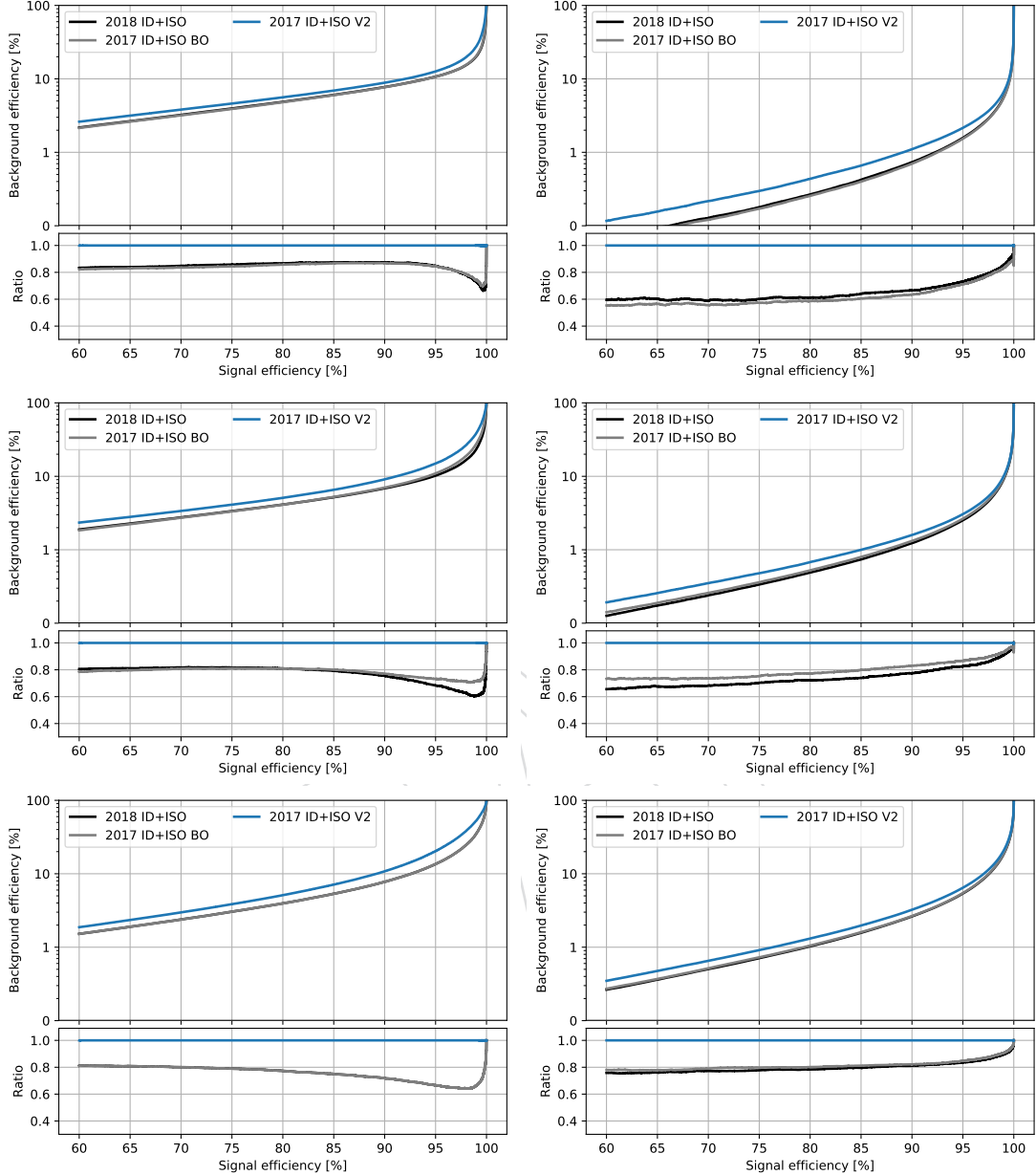


Figure 7: The receiver operating characteristic curves, representing the background efficiency vs signal efficiency, of the MVA trained on the 2017 Drell-Yan with jets MC sample and applied on the 2018 Drell-Yan with jets MC sample. The training combines identification and isolation features. Performance are shown for electrons with $5 < p_T < 10 \text{ GeV}$ (left), $p_T > 10 \text{ GeV}$ (right), and $||\eta|| < 0.8$ (top), $0.8 < |\eta| < 1.479$ (middle), and $|\eta| > 1.479$ (bottom). V1 and V2 versions of training are compared, exploiting TMVA and xgboost training libraries respectively.

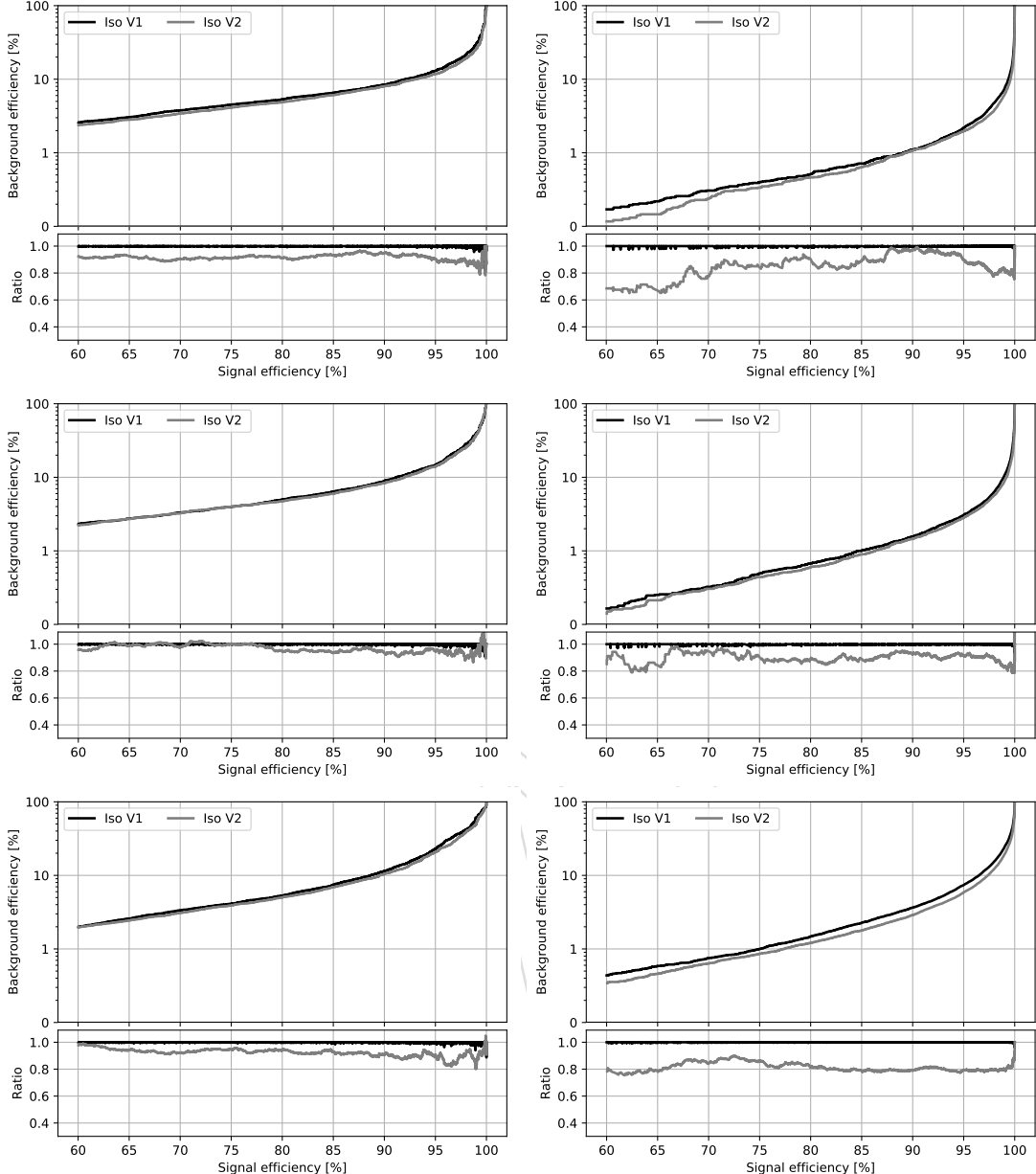


Figure 8: Performance comparison, background efficiency vs signal efficiency, of the MVA trained using TMVA framework (V1) and XGBoost framework (V2). The performance are shown for electrons with $5 < p_T < 10$ GeV (left), $p_T > 10$ GeV (right), and $|\eta| < 0.8$ (top), $0.8 < |\eta| < 1.479$ (middle), and $|\eta| > 1.479$ (bottom).

2016 Datasets			
minimum BDT score	$ \eta < 0.8$	$0.8 < \eta < 1.479$	$ \eta > 1.479$
$5 < p_T < 10$ GeV	0.9503	0.9461	0.9387
$p_T > 10$ GeV	0.3782	0.3587	-0.5745

Table 11: Minimum BDT score required for passing the electron identification, for 2016 samples.

2017 Datasets				
minimum BDT score	$ \eta < 0.8$	$0.8 < \eta < 1.479$	$ \eta > 1.479$	
$5 < p_T < 10 \text{ GeV}$	0.8521	0.8268	0.8694	
$p_T > 10 \text{ GeV}$	0.9825	0.9692	0.7935	

Table 12: Minimum BDT score required for passing the electron identification, for 2017 samples.

$ \eta < 0.8$		
	Cut on BDT score	Signal eff. Background eff.
$5 < p_T < 10 \text{ GeV}$	0.8956	81.04% 4.4%
$p_T > 10 \text{ GeV}$	0.0424	97.1% 2.9%
$0.8 < \eta < 1.479$		
	Cut on BDT score	Signal eff. Background eff.
$5 < p_T < 10 \text{ GeV}$	0.9111	79.3% 4.6%
$p_T > 10 \text{ GeV}$	0.0047	96.3% 3.6%
$ \eta > 1.479$		
	Cut on BDT score	Signal eff. Background eff.
$5 < p_T < 10 \text{ GeV}$	0.9401	72.97% 3.6%
$p_T > 10 \text{ GeV}$	-0.6042	95.7% 6.7%

Table 13: Minimum MVA score required for passing the electron identification, together with the corresponding signal and background efficiencies, for 2018 samples.

213 **3.1.3 Electron Impact Parameter Selection**

214 In order to ensure that the leptons are consistent with a common primary vertex we require
215 that they have an associated track with a small impact parameter with respect to the event
216 primary vertex. We use the significance of the impact parameter to the event vertex, $SIP_{3D} =$
217 $\frac{IP}{\sigma_{IP}}$, where IP is the lepton impact parameter in three dimensions at the point of closest approach
218 with respect to the primary interaction vertex, and σ_{IP} the associated uncertainty. Hereafter, a
219 "primary lepton" is a lepton satisfying $|SIP_{3D}| < 4$.

220 **3.1.4 Electron Energy Calibrations**

221 Electrons in data are corrected for features in ECAL energy scale in bins of p_T and $|\eta|$. Correc-
222 tions are calculated on a $Z \rightarrow ee$ sample to align the dielectron mass spectrum in the data to
223 that in the MC, and to minimize its width.

224 The $Z \rightarrow ee$ mass resolution in Monte Carlo is made to match data by applying a pseudoran-
225 dom Gaussian smearing to electron energies, with Gaussian parameters varying in bins of p_T
226 and $|\eta|$. This has the effect of convoluting the electron energy spectrum with a Gaussian.

227 The electron energy scale is measured in data by fitting a Crystall-ball function to the di-
228 electron mass spectrum around the Z peak in the $Z \rightarrow ee$ control region. The energy scale
229 for the 2016, 2017 and 2018 dataset are shown in Fig. 9, 10, 11 (a), respectively, and decently
230 agrees with the MC with the preliminary corrections released so far by EGAMMA POG.

DRAFT

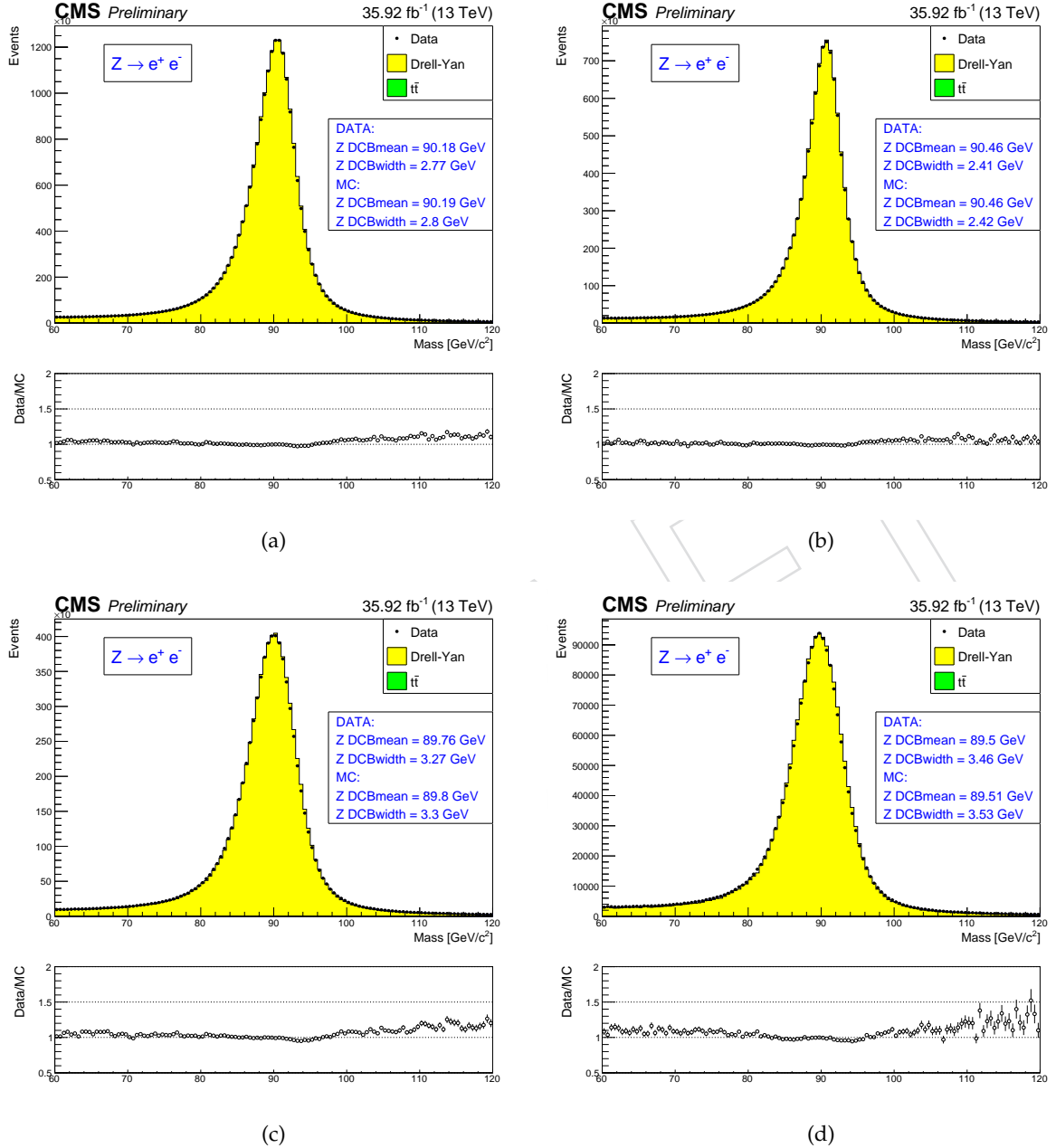


Figure 9: (a): electron energy scale measured in the $Z \rightarrow ee$ control region for all electrons, for both electrons in the barrel (b), for one electron in the barrel, one in the endcaps (c) and for both electrons in the endcaps (d), for 2016 data. The results of the Crystall-ball fit are reported in the figures.

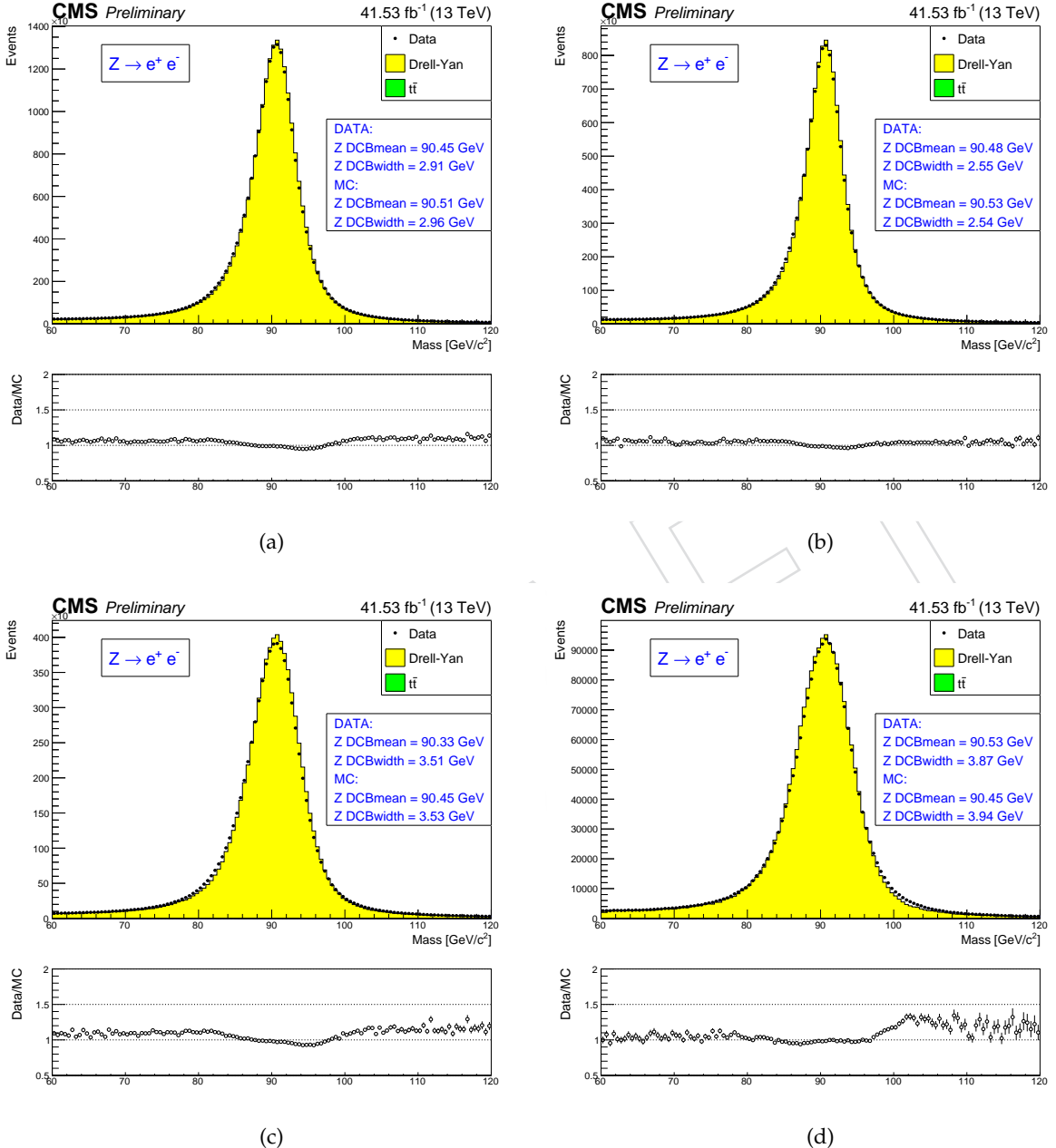


Figure 10: (a): electron energy scale measured in the $Z \rightarrow ee$ control region for all electrons, for both electrons in the barrel (b), for one electron in the barrel, one in the endcaps (c) and for both electrons in the endcaps (d), for 2017 data. The results of the Crystall-ball fit are reported in the figures.

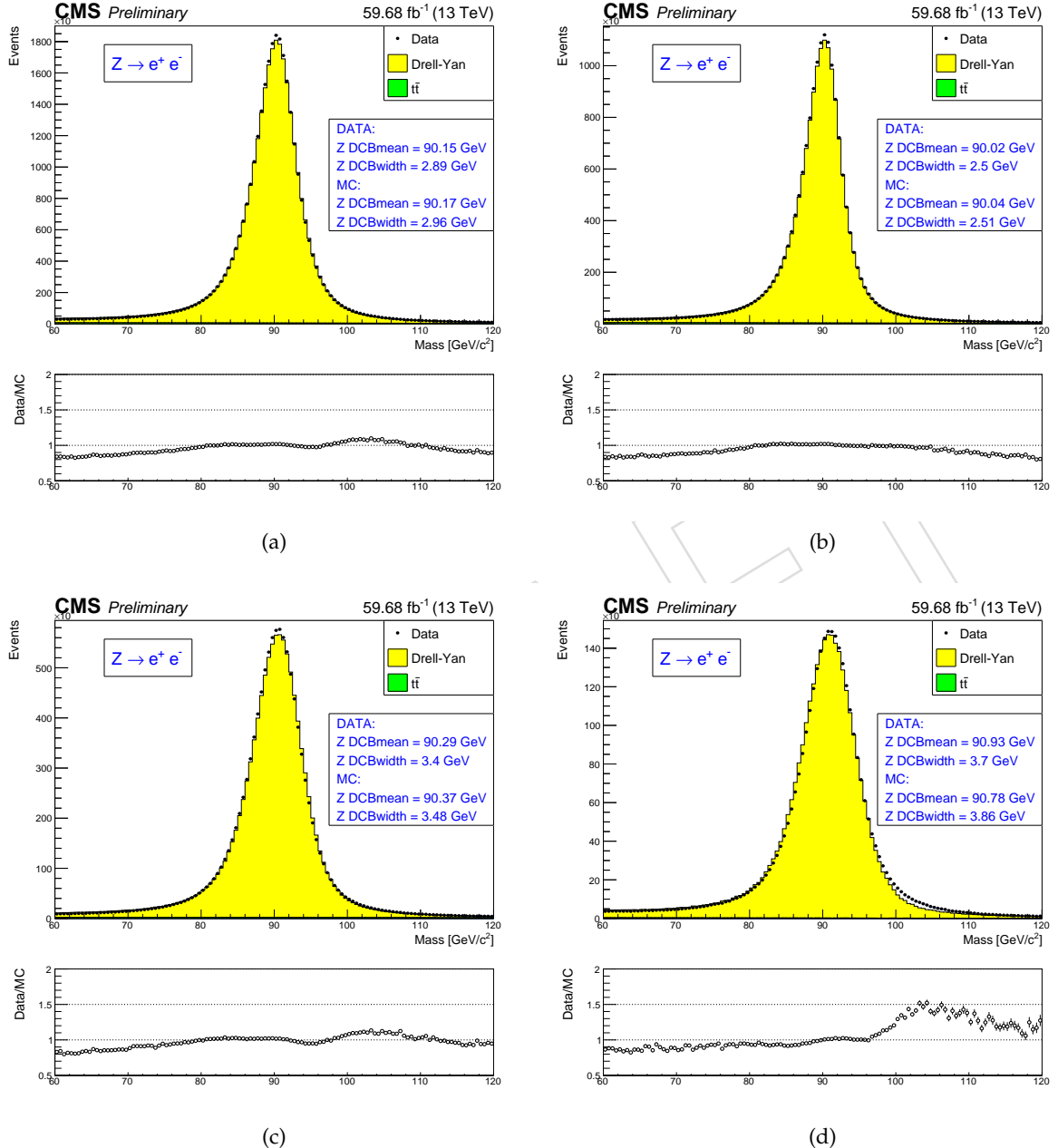


Figure 11: (a): electron energy scale measured in the $Z \rightarrow ee$ control region for all electrons, for both electrons in the barrel (b), for one electron in the barrel, one in the endcaps (c) and for both electrons in the endcaps (d), for 2018 data. The results of the Crystall-ball fit are reported in the figures.

231 **3.1.5 Electron Efficiency Measurements**

232 The Tag-and-Probe study was performed on the EGM dataset using the golden JSON of 58.83
233 fb^{-1} . More details on the Tag-and-Probe method can be found in Ref. [35].

234 Tag electrons need to satisfy the following quality requirements:

- 235 • trigger matched to single electron trigger (e.g HLT_Ele32_WPTight_Gsf_L1DoubleEG_v*
236 for 2018 for instance)
- 237 • $p_T > 30 \text{ GeV}$ (tag), super cluster (SC) $\eta < 2.17$
- 238 • the tag and the probe need to have opposite charge.

239 For the bin between 7 and 20 GeV, additional criteria are required:

- 240 • the tag has to pass a cut on the MVA ID > 0.92 , $\sqrt{(2 * \text{PFMET} * p_T(\text{tag}) * (1 -$
241 $\cos(\phi_{\text{MET}} - \phi_{\text{tag}})))} < 45 \text{ GeV}$.
- 242 • tag p_T increased to 50 GeV
- 243 • the charge is determined with the so-called selection method, using all three esti-
244 mates of the electron charge to agree.

245 These additional requirements help cleaning the background and makes the fits more reliable
246 (and thus, the measurement more precise).

247 Probe electrons only need to be reconstructed as GsfElectron while the FSR recovery algorithm
248 is not applied in efficiency measurement.

249 The nominal MC efficiencies are evaluated from the LO MadGraph Drell-Yan, while the NLO
250 systematics use the MadGraph_AMCatNLO sample (or POWHEG in 2018).

251 For the efficiency measurements a template fit is used. The m_{ee} signal shape of the passing and
252 failing probes is taken from MC and convoluted with a Gaussian. The data is then fitted with
253 the convoluted MC template and a CMSShape (an Error-function with a one-sided exponential
254 tail). This change follows from the usage of the T&P tool developed by the EGM POG. For the
255 low p_T bins, a gaussian is added to the signal model for the failing probes.

256 The electron selection efficiency is measured as a function of the probe electron p_T and its SC
257 η , and separately for electrons falling in the ECAL gaps. Figure 12, 14, 16 and 13,15, 17 show
258 the p_T and η turn-on curves measured in data, for 2016, 2017 and 2018.

259 The EGM recommendations on the evaluation of Tag-and-Probe uncertainties for efficiency
260 measurements are followed. Specifically, we consider

- 261 • Variation of the signal shape from a MC shape to an analytic shape (Crystal Ball)
262 fitted to the MC
- 263 • Variation of the background shape from a CMS-shape to a simple exponential in fits
264 to data
- 265 • Using an NLO MC sample for the signal templates

266 The total uncertainty for the measurement of the scale factors is the quadratic sum of the sta-
267 tistical uncertainties returned from the fit and the aforementioned systematic uncertainties.

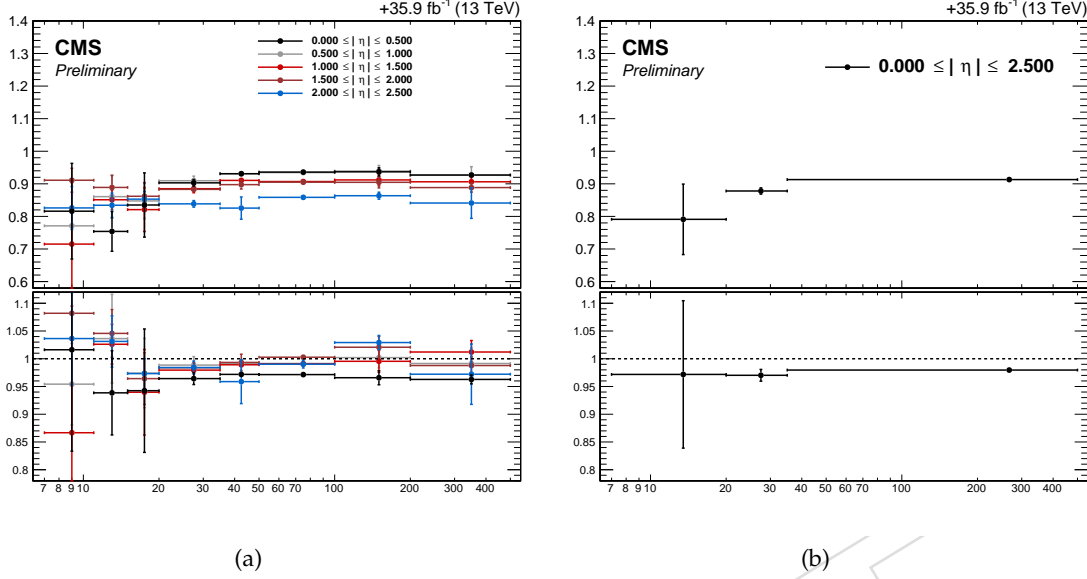


Figure 12: Electron selection efficiencies vs p_T measured using the Tag-and-Probe technique described in the text, non-gap electrons (left) and gap electrons (right), together with the corresponding data/MC ratio (bottom), for 2016 samples.

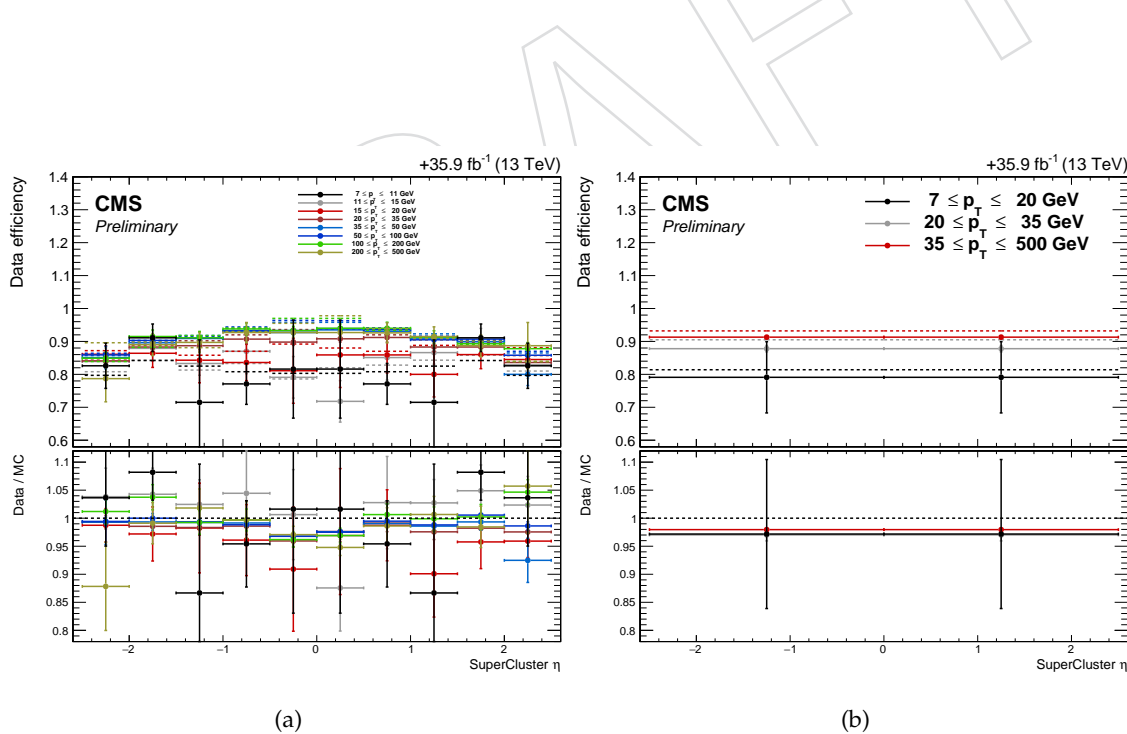


Figure 13: Electron selection efficiencies vs η measured using the Tag-and-Probe technique described in the text, non-gap electrons (left) and gap electrons (right), together with the corresponding data/MC ratio at the bottom of each plot, for 2016 samples. Dashed lines is MC, solid lines is DATA.

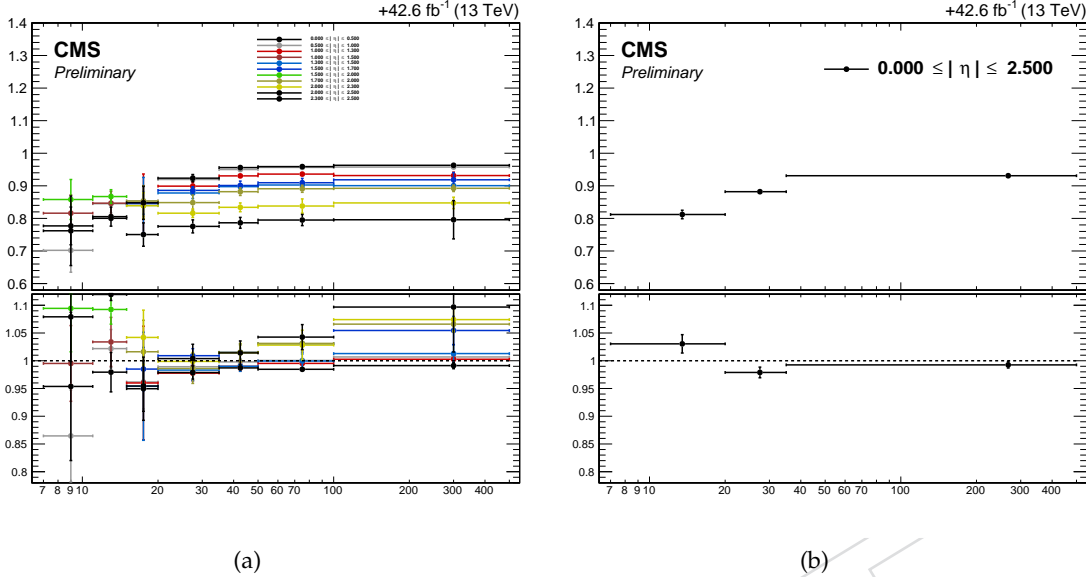


Figure 14: Electron selection efficiencies vs p_T measured using the Tag-and-Probe technique described in the text, non-gap electrons (left) and gap electrons (right), together with the corresponding data/MC ratio (bottom), for 2017 samples.

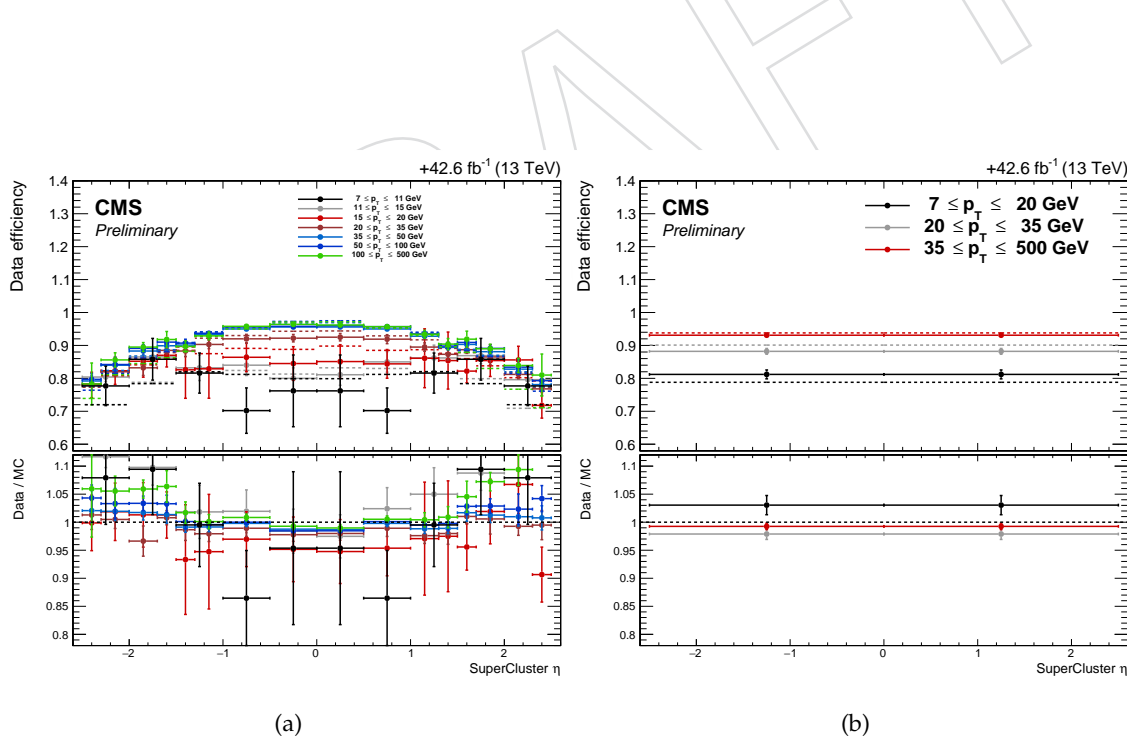


Figure 15: Electron selection efficiencies vs η measured using the Tag-and-Probe technique described in the text, non-gap electrons (left) and gap electrons (right), together with the corresponding data/MC ratio at the bottom of each plot, for 2017 samples. Dashed lines is MC, solid lines is DATA.

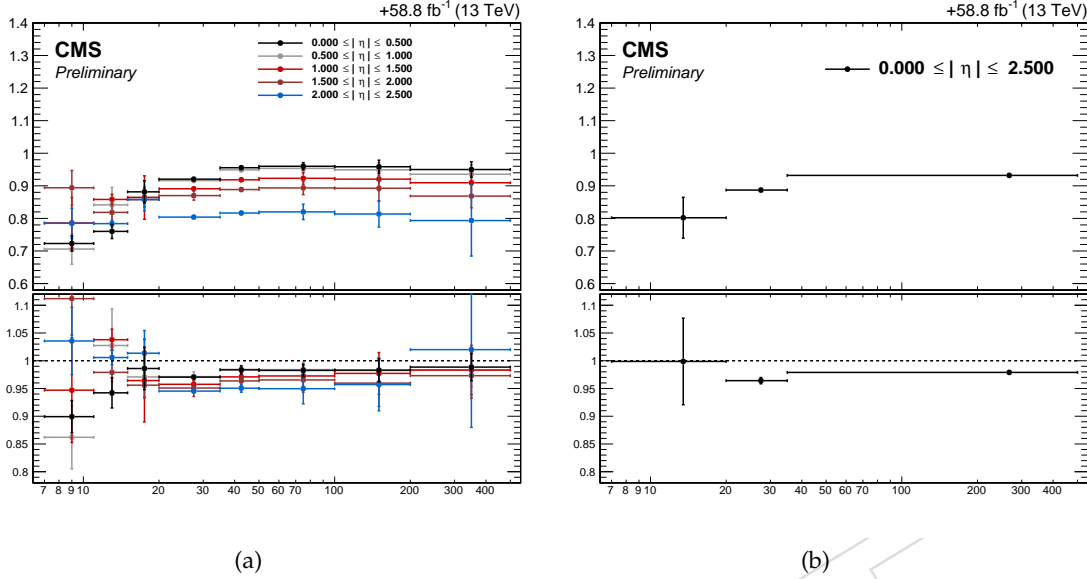


Figure 16: Electron selection efficiencies vs p_T measured using the Tag-and-Probe technique described in the text, non-gap electrons (left) and gap electrons (right), together with the corresponding data/MC ratio (bottom), for 2018 samples.

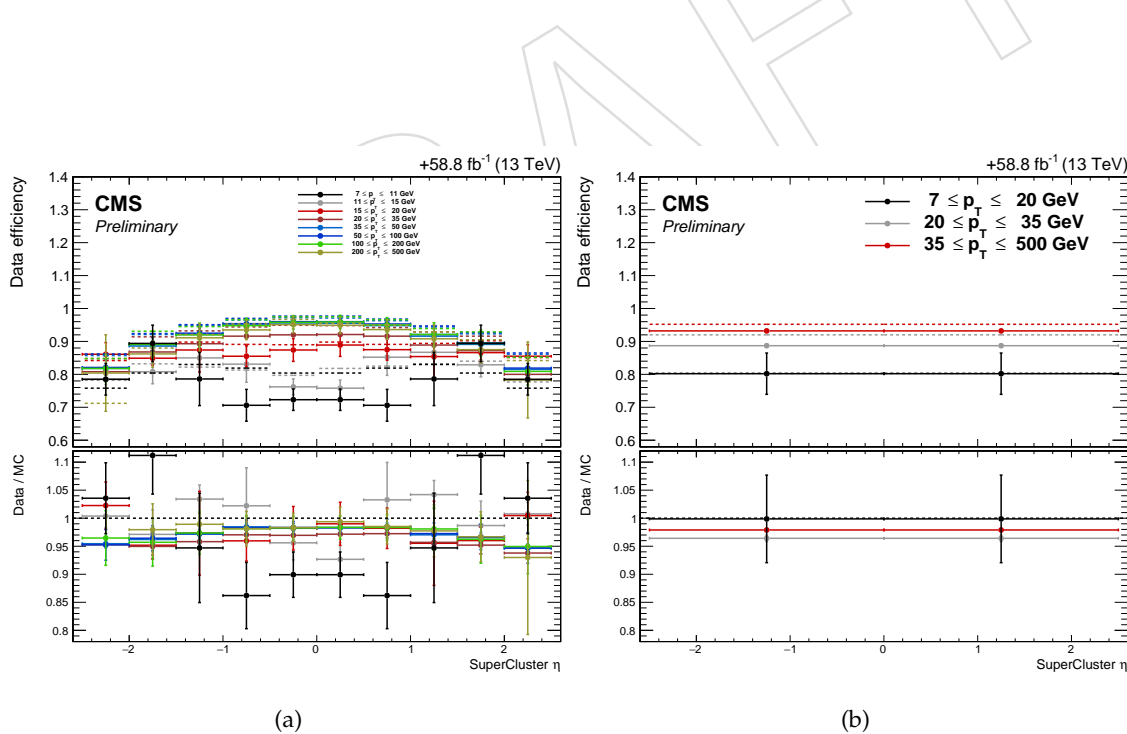


Figure 17: Electron selection efficiencies vs η measured using the Tag-and-Probe technique described in the text, non-gap electrons (left) and gap electrons (right), together with the corresponding data/MC ratio at the bottom of each plot, for 2018 samples. Dashed lines is MC, solid lines is DATA.

268 **3.2 Muons**269 **3.2.1 Muon Reconstruction**

270 More details on muon reconstruction can be found in Ref. [35]. We define **loose muons** as the
 271 muons that satisfy $p_T > 5$, $|\eta| < 2.4$, $d_{xy} < 0.5$ cm, $d_z < 1$ cm, where d_{xy} and d_z are defined
 272 w.r.t. the PV and using the ‘muonBestTrack’. Muons have to be reconstructed by either the
 273 Global Muon or Tracker Muon algorithm. Standalone Muon tracks that are only reconstructed
 274 in the muon system are rejected. Muons with muonBestTrackType==2 (standalone) are dis-
 275 carded even if they are marked as global or tracker muons.

276 Loose muons with p_T below 200 GeV are considered identified muons if they also pass the PF
 277 muon ID (note that the naming convention used for these IDs differs from the muon POG
 278 naming scheme, in which the “tight ID” used here is called the “loose ID”). Loose muons with
 279 p_T above 200 GeV are considered identified muons if they pass the PF ID or the Tracker High-
 280 p_T ID, the definition of which is shown in Table 14. This relaxed definition is used to increase
 281 signal efficiency for the high-mass search. When a very heavy resonance decays to two Z
 282 bosons, both bosons will be very boosted. In the lab frame, the leptons coming from the decay
 283 of a highly boosted Z will be nearly collinear, and the PF ID loses efficiency for muons separated
 284 by approximately $\Delta R < 0.4$, which roughly corresponds to muons originating from Z bosons
 285 with $p_T > 500$ GeV.

Table 14: The requirements for a muon to pass the Tracker High- p_T ID. Note that these are equivalent to the Muon POG High- p_T ID with the global track requirements removed.

Plain-text description	Technical description
Muon station matching	Muon is matched to segments in at least two muon stations NB: this implies the muon is an arbitrated tracker muon.
Good p_T measurement	$\frac{p_T}{\sigma_{p_T}} < 0.3$
Vertex compatibility ($x - y$)	$d_{xy} < 2$ mm
Vertex compatibility (z)	$d_z < 5$ mm
Pixel hits	At least one pixel hit
Tracker hits	Hits in at least six tracker layers

286 An additional “ghost-cleaning” step is performed to deal with situations when a single muon
 287 can be incorrectly reconstructed as two or more muons:

- 288 • Tracker Muons that are not Global Muons are required to be arbitrated.
- 289 • If two muons are sharing 50% or more of their segments then the muon with lower
 290 quality is removed.

291 **3.2.2 Muon Isolation**

Particle-Flow based isolation is used for the muons. The so-called $\Delta\beta$ correction is applied in order to subtract the pileup contribution for the muons, whereby $\Delta\beta = \frac{1}{2} \sum_{\text{PU}}^{\text{charged had.}} p_T$ gives an estimate of the energy deposit of neutral particles (hadrons and photons) from pile-up vertices. The relative isolation for muons is then defined as:

$$\text{RelPFiso} = \frac{\sum_{\text{lepton}}^{\text{charged had.}} p_T + \max(\sum_{\text{neutral had.}}^{} E_T + \sum_{\text{photon}}^{} E_T - \Delta\beta, 0)}{p_T} \quad (1)$$

292 The isolation working point for muons was optimized in Ref. [35] and the working point was
293 chosen to be the same as electrons, namely $\text{RelPFiso}(\Delta R = 0.3) < 0.35$.

294 **3.2.3 Muon Impact Parameter Selection**

295 In addition to a cut to the Muon BDT, we apply an additional cut to the muon significance of
296 impact parameter as for the electrons, as described in Sec. 3.1.3:

- 297 • $|\text{SIP}_{3D} = \frac{\text{IP}}{\sigma_{\text{IP}}} | < 4$

298 **3.2.4 Muon Energy Calibrations**

299 Similar to electrons the muon momentum scale is measured in data by fitting a Crystall-ball
300 function to the di-muon mass spectrum around the Z peak in the $Z \rightarrow \mu\mu$ control region.
301 Fig. 18, 19 and 20 shows a very good agreement between data and simulation, for 2016, 2017
302 and 2018 eras, respectively.

DRAFT

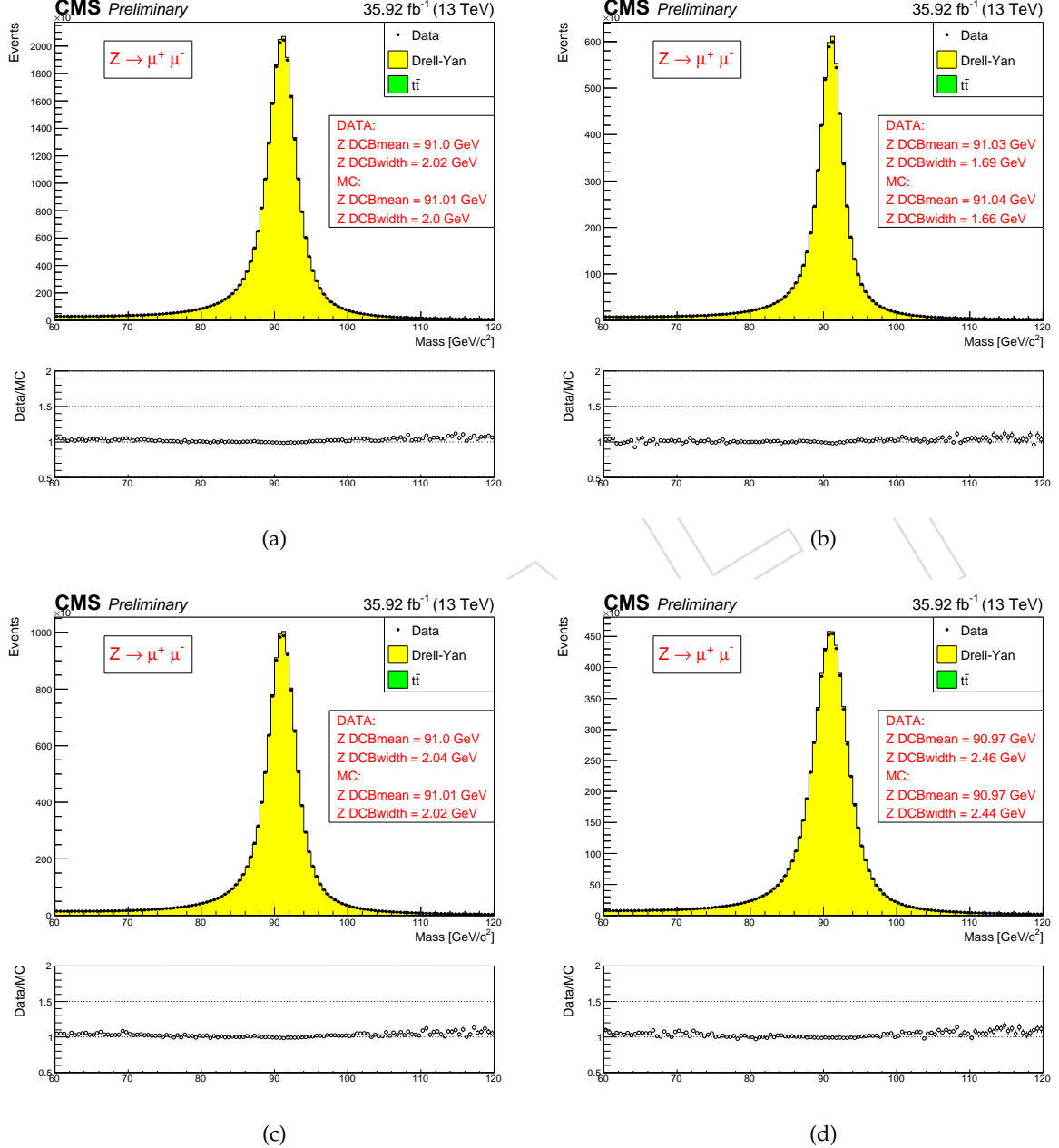


Figure 18: (a): muon energy scale measured in the $Z \rightarrow \mu\mu$ control region for all muons, for both muons in the barrel (b), for one muon in the barrel, one in the endcaps (c) and for both muons in the endcaps (d), for 2016. The results of the Crystall-ball fit are reported in the figures.

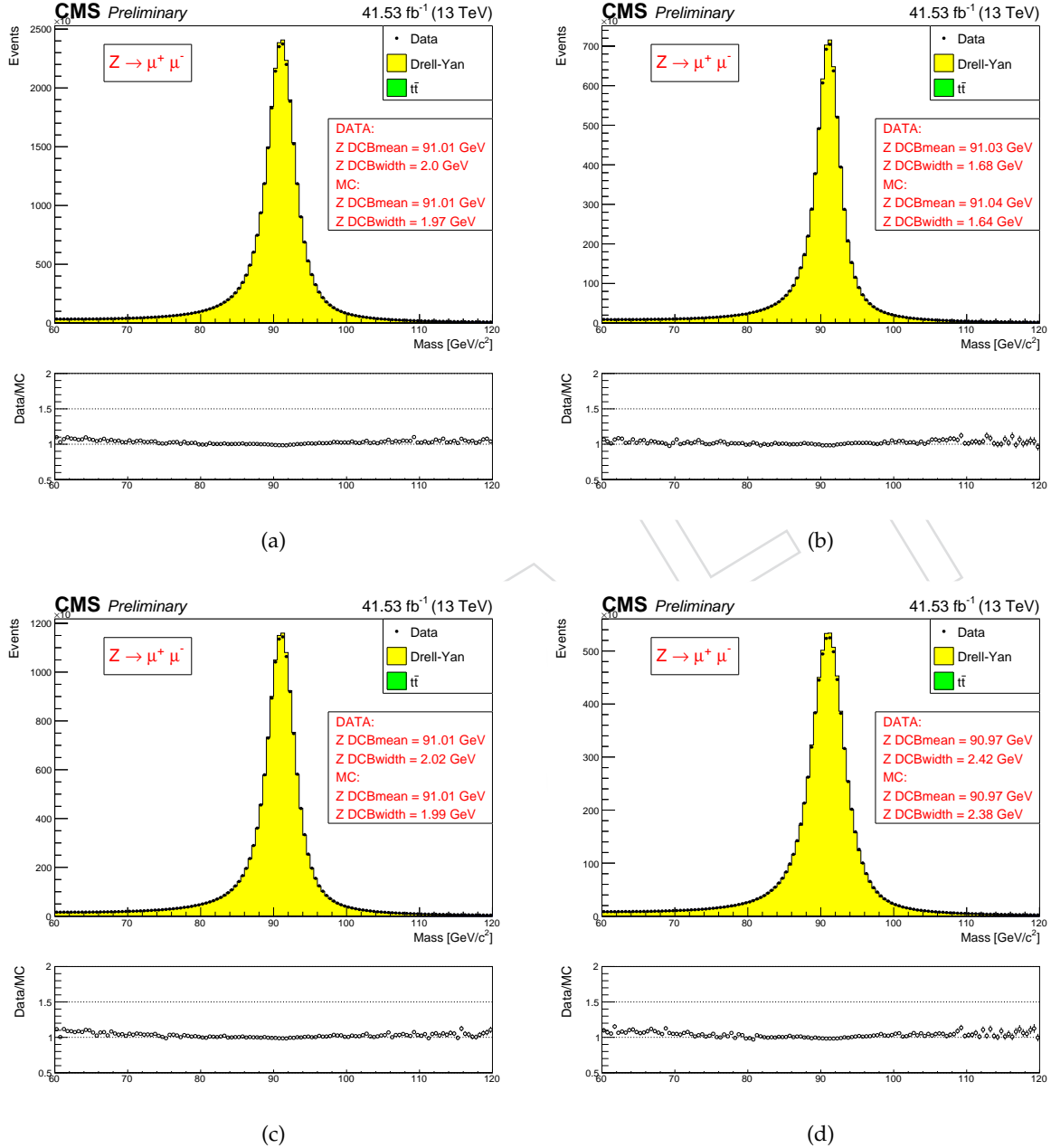


Figure 19: (a): muon energy scale measured in the $Z \rightarrow \mu\mu$ control region for all muons, for both muons in the barrel (b), for one muon in the barrel, one in the endcaps (c) and for both muons in the endcaps (d), for 2017. The results of the Crystall-ball fit are reported in the figures.

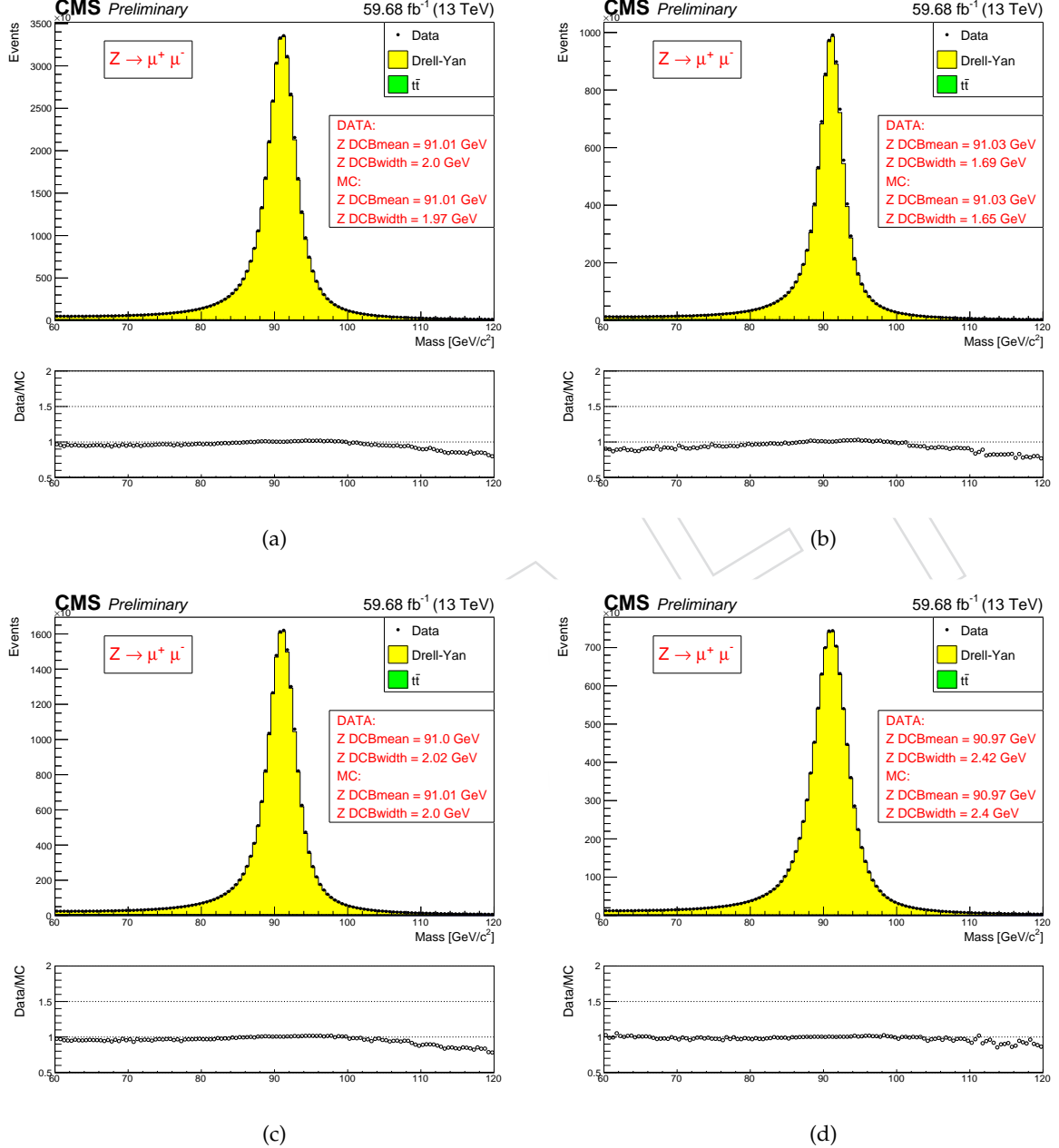


Figure 20: (a): muon energy scale measured in the $Z \rightarrow \mu\mu$ control region for all muons, for both muons in the barrel (b), for one muon in the barrel, one in the endcaps (c) and for both muons in the endcaps (d), for 2018. The results of the Crystall-ball fit are reported in the figures.

303 3.2.5 Muon Efficiency Measurements

304 Muon efficiencies are measured with the Tag and Probe (T&P) method performed on $Z \rightarrow \mu\mu$
 305 and $J/\psi \rightarrow \mu\mu$ events in bins of p_T and η . More details on the methodology can be found in
 306 Ref. [36]. Measurements are extracted using 2018 RunA,B,C,D data while the measurements
 307 corresponding to 2016 and 2017 datasets have already been reported in Ref. [37] and Ref. [38]
 308 respectively. The Z sample is used to measure the muon reconstruction and identification ef-
 309 ficiency at high p_T , and the efficiency of the isolation and impact parameter requirements at
 310 all p_T . The J/ψ sample is used to measure the reconstruction efficiency at low p_T , as it ben-
 311 efits from a better purity in that kinematic regime. In this case, events are collected using
 312 `HLT_Mu7p5_Track2_Jpsi_v*` when probing the reconstruction and identification efficiency
 313 in the muon system, and using the `HLT_Mu7p5_L2Mu2_Jpsi_v*` when probing the tracking
 314 efficiency.

315 **Reconstruction and identification** Results for the muon reconstruction and identification
 316 efficiency for $p_T > 20$ GeV have been derived by the Muon POG. The probe in this measure-
 317 ment are tracks reconstructed in the inner tracker, and the passing probes are those that are
 318 also reconstructed as a global or tracker muon and passing the Muon POG Loose muon identi-
 319 fication. Results for low p_T muons were derived using J/ψ events, with the same definitions of
 320 probe and passing probes. The systematic uncertainties are estimated by varying the analytical
 321 signal and background shape models used to fit the dimuon invariant mass. Details on the
 322 procedure can be found in Ref. [35]. The efficiency and scale factors used for low p_T muons are
 323 the ones derived using single muon prompt-reco dataset.

324 The efficiency in data and simulation is shown in Fig. 21.

325 **Impact parameter requirements** The measurement is performed using Z events. Events
 326 are selected with `HLT_IsoMu27_v*` or `HLT_Mu50_v*` triggers. For this measurement, the
 327 probe is a muon passing the POG Loose identification criteria, and it is considered a passing
 328 probe if satisfies the SIP3D, dxy , dz cuts of this analysis. The results are shown in Fig. 22.

329 **Isolation requirements** The isolation efficiency is measured using events from the Z decay
 330 for any p_T . The events are selected with either of `HLT_IsoMu27_v*` or `HLT_Mu50_v*` triggers.
 331 The isolation of the muons are calculated after recovery of the FSR photons and subtracting
 332 their contribution to the isolation cone of the muons. More detailed description of the method
 333 can be found in Ref. [39].

334 The results are shown in Fig. 23.

335 **Tracking** The efficiency to reconstruct a muon track in the inner detector is measured us-
 336 ing as probes tracks reconstructed in the muon system alone. The method for measuring the
 337 tracking efficiency is the same as in Ref. [40], and the results on 2018 data are briefly discussed
 338 here. The efficiency and data to mc scale factors are measured from Z events as a function of
 339 η for $p_T > 10$ GeV and $p_T < 10$ GeV. The values of data to mc scale factors used are from the
 340 ReReco version of the full dataset collected in 2018.

341 **Overall results** The product of all the data to simulation scale factors for muon tracking,
 342 reconstruction, identification, impact parameter and isolation requirements is shown in Fig. 24.

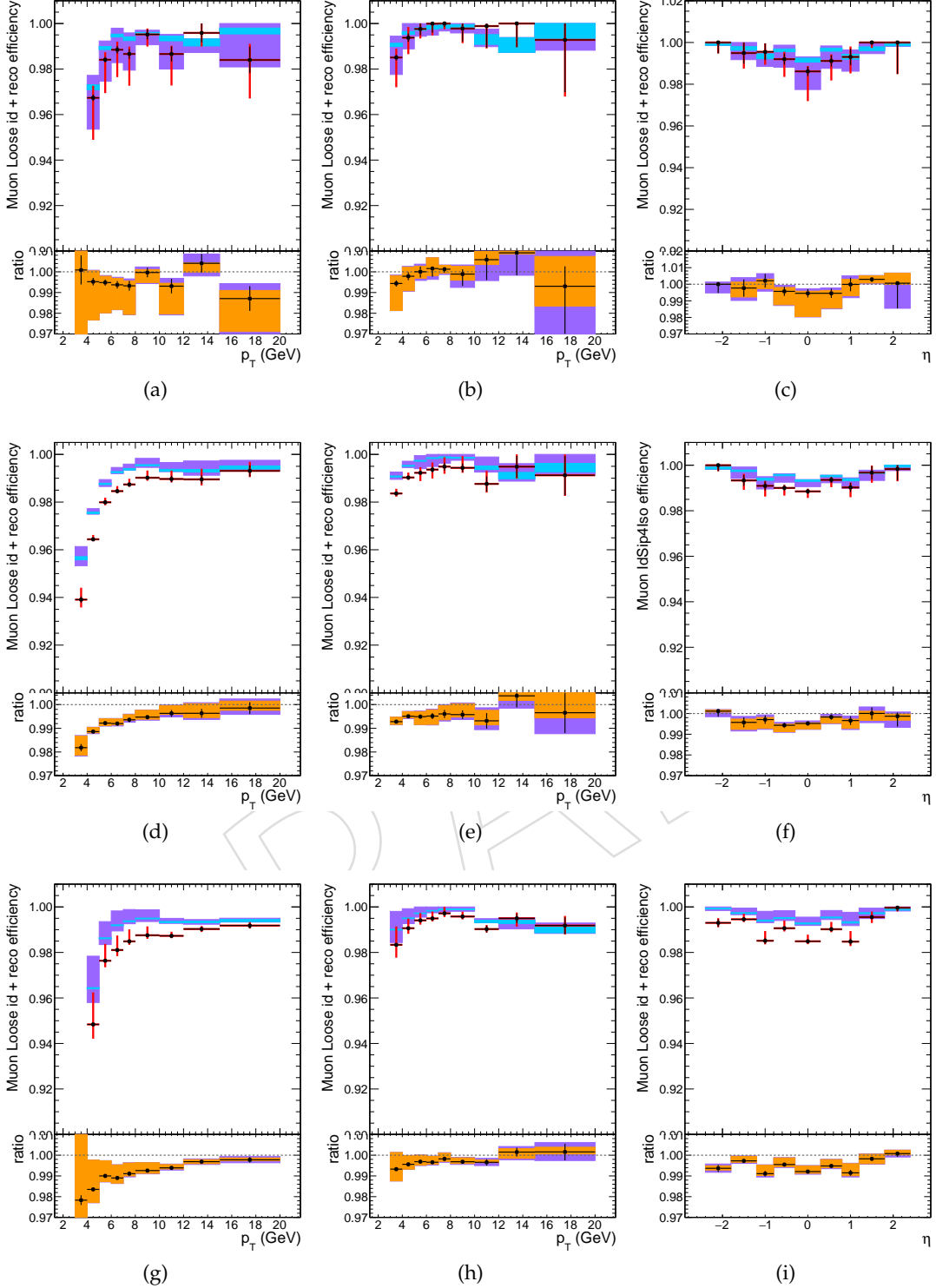


Figure 21: Muon reconstruction and identification efficiency at low p_T , measured with the tag&probe method on J/ψ events, as function of p_T in the barrel (left) and endcaps (center), and as function of η for $p_T > 7\text{ GeV}$ (right), for 2016 (top), 2017 (middle) and 2018 (bottom). In the upper panel, the larger error bars include also the systematical uncertainties, while the smaller ones are purely statistical. In the lower panel showing the ratio of the two efficiencies, the black error bars are for the statistical uncertainty, the orange rectangles for the systematical uncertainty and the violet rectangles include both uncertainties.

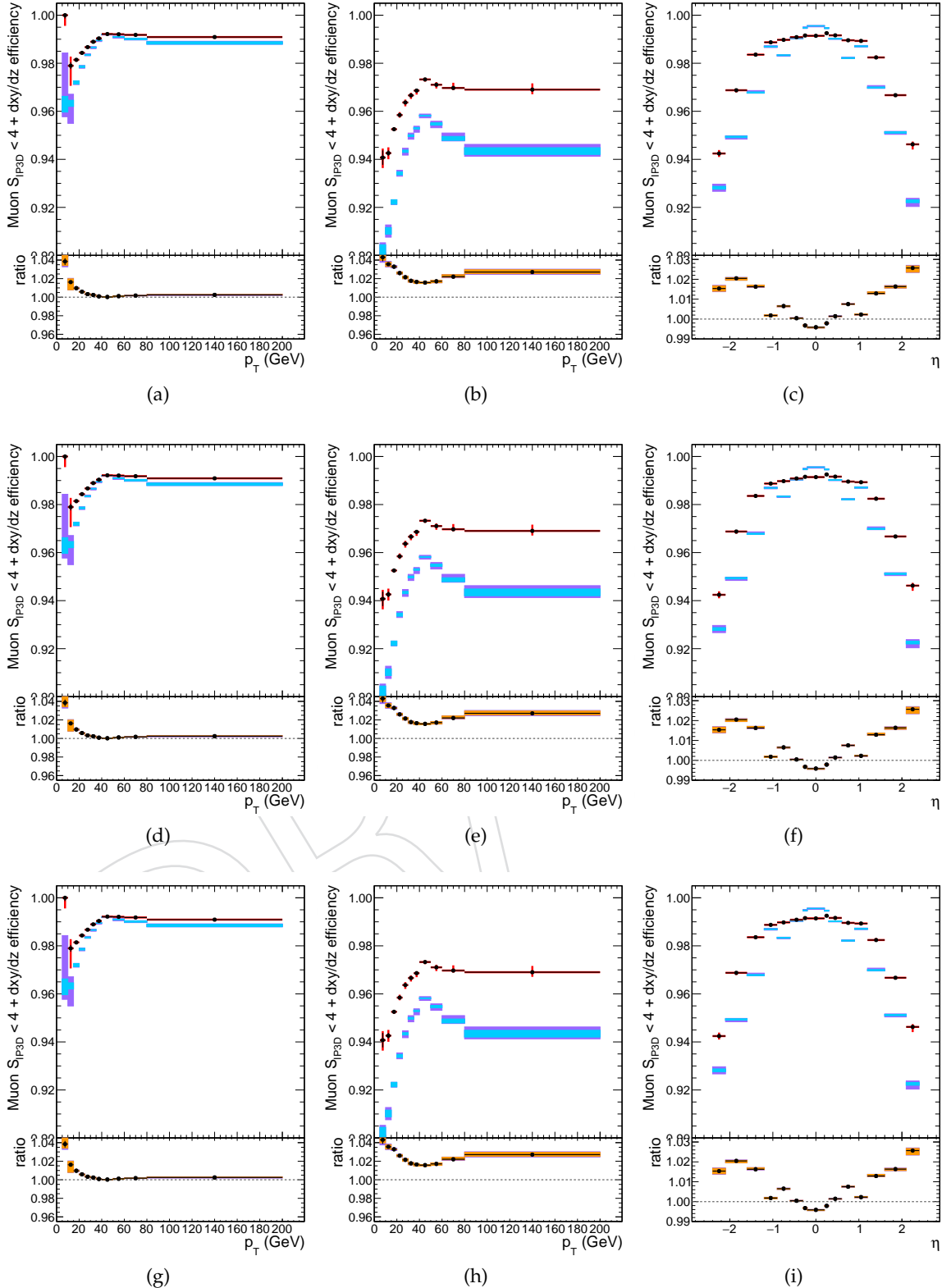


Figure 22: Efficiency of the muon impact parameter requirements, measured with the tag&probe method on Z events, as function of p_T in the barrel (left) and endcaps (center), and as function of η for $p_T > 20$ GeV (right), for 2016 (top), 2017 (middle) and 2018 (bottom). In the upper panel, the larger error bars include also the systematical uncertainties, while the smaller ones are purely statistical. In the lower panel showing the ratio of the two efficiencies, the black error bars are for the statistical uncertainty, the orange rectangles for the systematical uncertainty and the violet rectangles include both uncertainties.

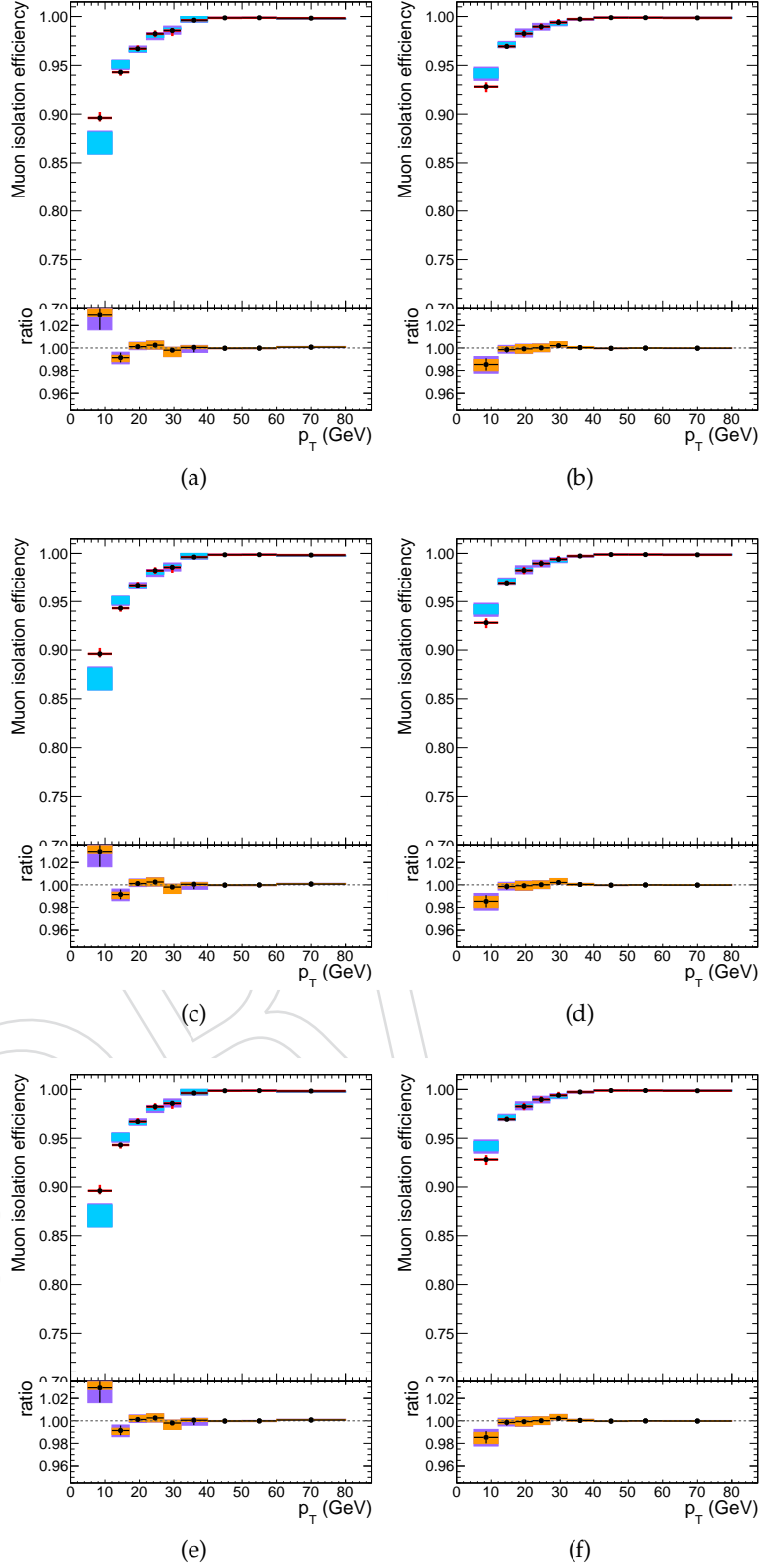


Figure 23: Efficiency of the muon isolation requirement, measured with the tag&probe method on Z events, as function of p_T in the barrel (left) and endcaps (right), for 2016 (top), 2017 (middle) and 2018 (bottom). In the upper panel, the larger error bars include also the systematical uncertainties, while the smaller ones are purely statistical. In the lower panel showing the ratio of the two efficiencies, the black error bars are for the statistical uncertainty, the orange rectangles for the systematical uncertainty and the violet rectangles include both uncertainties.

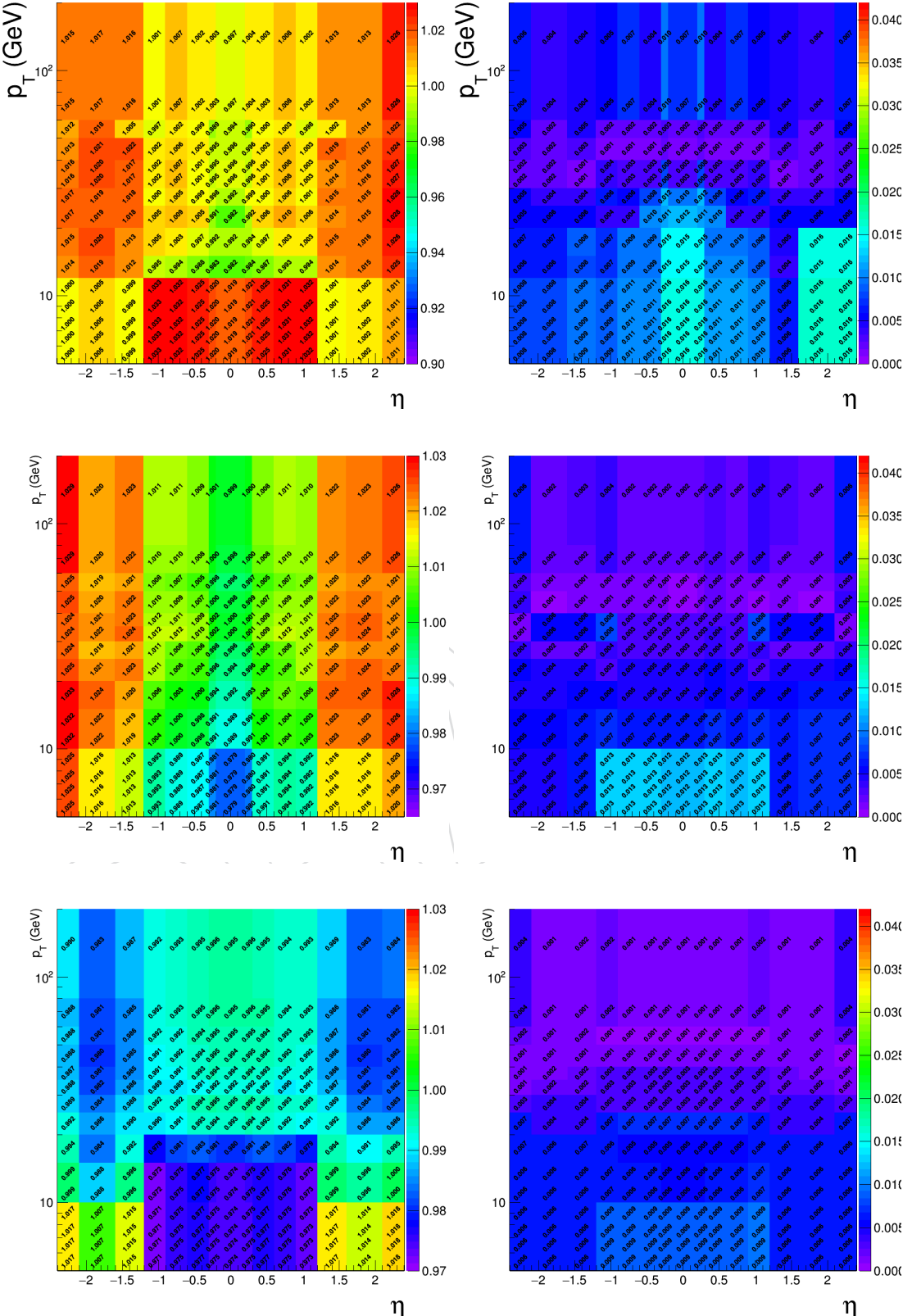


Figure 24: Left: Overall data to simulation scale factors for muons, as function of p_T and η . Right: Uncertainties on data to simulation scale factors for muons, as function of p_T and η . Results are shown for 2016 (top), 2017 (middle) and 2018 (bottom).

344 **3.3 Photons for FSR recovery**

345 The FSR recovery algorithm was considerably simplified with respect to what was done in Run
 346 I, while maintaining similar performance. The selection of FSR photons is now only done per-
 347 lepton and no longer depends on any Z mass criterion, thus much simplifying the subsequent
 348 ZZ candidate building and selection. As regards the association of photons with leptons, the
 349 rectangular cuts on $\Delta R(\gamma, l)$ and $E_{T,\gamma}$ have been replaced by a cut on $\Delta R(\gamma, l)/E_{T,\gamma}^2$.

350 Starting from the collection of ‘PF photons’ provided by the particle-flow algorithm, the selec-
 351 tion of photons and their association to a lepton proceeds as follows:

- 352 1. The preselection of PF photons is done by requiring $p_{T,\gamma} > 2$ GeV, $|\eta^\gamma| < 2.4$, and a
 353 relative Particle-flow isolation smaller than 1.8. The latter variable is computed using
 354 a cone of radius $R = 0.3$, a threshold of 0.2 GeV on charged hadrons with a veto cone
 355 of 0.0001, and 0.5 GeV on neutral hadrons and photons with a veto cone of 0.01, also
 356 including the contribution from pileup vertices (with the same radius and threshold as
 357 per charged isolation) .
- 358 2. Supercluster veto: we remove all PF photons that match with any electron passing both
 359 the loose ID and SIP cuts. The matching is performed by directly associating the two PF
 360 candidates.
- 361 3. Photons are associated to the closest lepton in the event among all those pass both the
 362 loose ID and SIP cuts.
- 363 4. We discard photons that do not satisfy the cuts $\Delta R(\gamma, l)/E_{T,\gamma}^2 < 0.012$, and $\Delta R(\gamma, l) < 0.5$.
- 364 5. If more than one photon is associated to the same lepton, the lowest- $\Delta R(\gamma, l)/E_{T,\gamma}^2$ is
 365 selected.
- 366 6. For each FSR photon that was selected, we exclude that photon from the isolation sum
 367 of all the leptons in the event that pass both the loose ID and SIP cuts. This concerns
 368 the photons that are in the isolation cone and outside the isolation veto of said leptons
 369 ($\Delta R < 0.4$ AND $\Delta R > 0.01$ for muons and $\Delta R < 0.4$ AND ($\eta^{\text{SC}} < 1.479$ OR $\Delta R > 0.08$)
 370 for electrons).

371 More details on the optimization of the FSR photon selection can be found in Ref. [35, 39].

372 **3.4 Jets**

373 Vector Boson Fusion (VBF) and other production mechanisms of Higgs Boson normally differ
 374 as regards the jet kinematics. In this analysis, jets are thus used for the event categorization,
 375 which will be introduced in Section ??.

376 **3.4.1 Jet Identification**

377 Jets are reconstructed by using the anti- k_T clustering algorithm out of particle flow candidates,
 378 with a distance parameter $R = 0.4$, after rejecting the charged hadrons that are associated to a
 379 pileup primary vertex.

380 To reduce instrumental background, the tight working point jet ID suggested by the JetMET
 381 Physics Object Group is applied [41]. In addition, jets from Pile-Up are rejected using the
 382 PileUp jet ID criteria suggested by the JetMET POG [42]. It is to be noted that the PU JetID
 383 was only derived for 2016 conditions but is also applied to 2017 and 2018 samples.

384 In this analysis, the jets are required to be within $|\eta| < 4.7$ area and have a transverse momen-
 385 tum above 30 GeV. In addition, the jets are cleaned from any of the tight leptons (passing the
 386 SIP and isolation cut computed after FSR correction) and FSR photons by a separation criterion:
 387 $\Delta R(\text{jet}, \text{lepton}/\text{photon}) > 0.4$.

388 3.4.2 Jet Energy Corrections

389 The calorimeter response to particles is not linear and it is not straightforward to translate
 390 the measured jet energy to the true particle or parton energy, therefore we need Jet Energy
 391 Corrections. In this analysis, standard jet energy corrections are applied to the reconstructed
 392 jets, which consist of L1 Pileup, L2 Relative Jet Correction, L3 Absolute Jet Correction for both
 393 Monte Carlo samples and data, and also residual calibration for data [43].

394 The table 15 summarizes the various JEC and JER tags used in this analysis.

	JEC tag	JER tag
2016	Summer16_07Aug2017All_V11	Summer16_25nsV1_MC
2017	Fall17_17Nov2017_V32_94X	Fall17_V3_94X_MC
2018	Autumn18_RunABCD_V19	Autumn18_V7_MC

Table 15: Summary of all JEC and JER tags.

395 3.4.3 Additional criteria on jets

396 The three data taking periods analyzed in this note suffered from issues during the data taking
 397 which impact the quality of the jet reconstruction. Some of these issues would need a complete
 398 re-reconstruction of the data to be fully fixed (the so-called “Ultra Legacy ReReco”), which is
 399 beyond the scope of the paper. In the mean time, following the guidance from the JetMET POG,
 400 we studied the possibility of adding some criteria on the jet to cope with these issues.

401 **3.4.3.1 L1 pre-firing** In 2016 and 2017, the gradual timing shift of ECAL was not properly
 402 propagated to L1 trigger primitives (TP) resulting in a significant fraction of high eta TP being
 403 mistakenly associated to the previous bunch crossing. Since Level 1 rules forbid two consecu-
 404 tive bunch crossings to fire, an unpleasant consequence of this (in addition to not finding the
 405 TP in the bx 0) is that events can self veto if a significant amount of ECAL energy is found in
 406 the region of $2 < |\eta| < 3$. This effect is not described by the simulations [44]. A weight is thus
 407 calculating for each event, not to prefire, and apply to the simulation in 2016 and 2017 samples.
 408 The official tool is used for this purpose [44].

409 The Fig 25 shows the impact of the L1 pre-firing weights on the signal MC. As expected, the
 410 effect on ggH samples is minor but is at the leve of 2-3% in the endcaps for VBF production
 411 mode.

412 **3.4.3.2 removal of noisy jets** Increased jet multiplicity was reported for 2017 data, cre-
 413 ating “horns” in the jet η distribution for $2.5 < \eta_{jet} < 3$ (FIXME: add ref). The issue was linked
 414 to an increase of the ECAL noise, PU and bunch-crossing dependant, thus getting worse as
 415 luminosity increases. The problem can only be fixed in the UL ReReco. For now, we checked
 416 the impact of rejecting jets with raw $p_T < 50$ GeV in $2.65 < \eta < 3.139$. As we see no significant
 417 impact in the data/MC agreement, we decided not to use these cuts.

418 **3.4.3.3 HEM 15/16 failures** Following a CMS-wide power interlock, the power-on of
 419 CAEN A3100HBP modules that provide low-voltage power to the on-detector HE front-end
 420 electronics led to irreversible damage of two sectors on the HE minus side, HEM15 and HEM16

421 (FIXME: add ref). No significant impact was seen and nothing particular is done to cope with
 422 this.

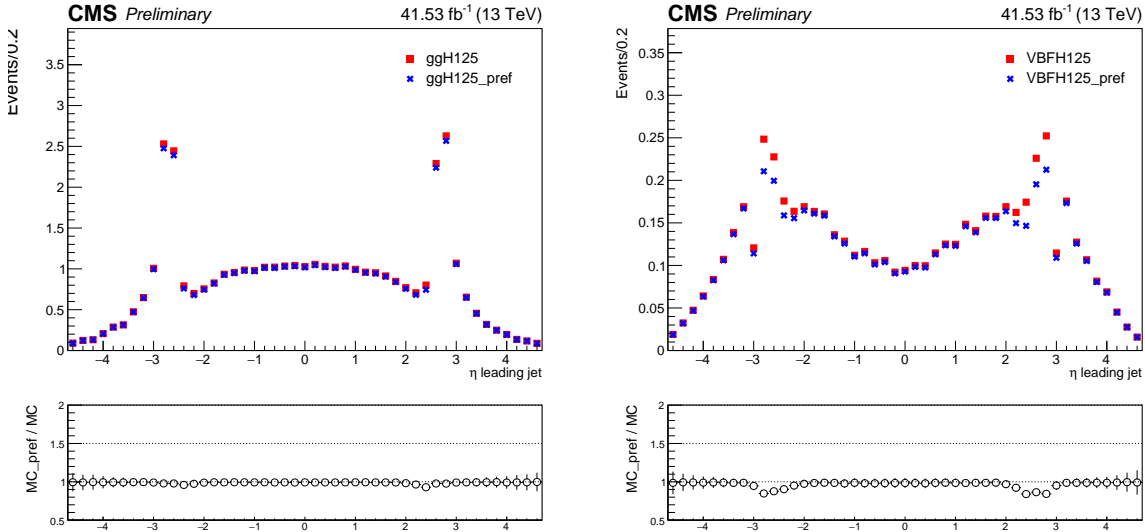


Figure 25: Comparison between 2017 MC samples with (blue) and without (red) L1 pre-firing weights for ggH (left) and VBFH signals. The ratio is shown at the bottom of each plot.

423 3.4.4 B-tagging

424 For categorization purpose, we need to distinguish whether a jet is b-jet or not. The *DeepCSV*
 425 algorithm is used as our b-tagging algorithm. It combines the same information as the previous
 426 tagger *CSVv2*, impact parameter significance, secondary vertex and jet kinematics but uses
 427 information of more tracks. Also, the b-tag output discriminator is computed with a Deep
 428 Neural Network. In this analysis, a jet is considered to be b-tagged if it passes the *medium*
 429 working point, i.e. if its $| \text{pfDeepCSVJetTags:prob} + \text{pfDeepCSVJetTags:prob}_{\text{bb}} |$ discriminator
 430 is greater than 0.4184 [45].

431 Data to simulation scale factors for b-tagging efficiency are provided for this working point
 432 for the full dataset as a function of jet p_T , η and flavour. They are applied to simulated jets by
 433 downgrading (upgrading) the b-tagging status of a fraction of the b-tagged (untagged) jets that
 434 have a scale factor smaller (larger) than one.

435 3.4.5 Missing Transverse Energy

436 MET is not used in this analysis to, for instance, categorize events.

437 3.4.6 Validation on data

438 Similarly to what was done with electrons and muons, we performed some validation studies
 439 to probe the agreement between data and simulated samples for jets. Events containing
 440 $Z \rightarrow e^+e^-$ or $Z \rightarrow \mu^+\mu^-$ were selected, following the same trigger and lepton selection crite-
 441 ria of the main analysis, but increasing the p_T threshold on leptons to 30 GeV and asking the
 442 invariant mass of the two leptons to be within the 70-110 GeV range.

443 Basic properties of additional jets in the event, with $p_T > 30$ GeV and $\eta < 4.7$, were then
 444 compared. Figure 26 shows the pseudo-rapidity and transverse momentum of the leading jet

in data and MC for the three data taking periods. Fig 27 shows the jet multiplicity. Uncertainties from the jet energy corrections are also displayed on the data/MC ratio plots.

The agreement between data and simulation is found to be good for the jet transverse momentum or pseudo-rapidity, given the large uncertainties in the forward region.

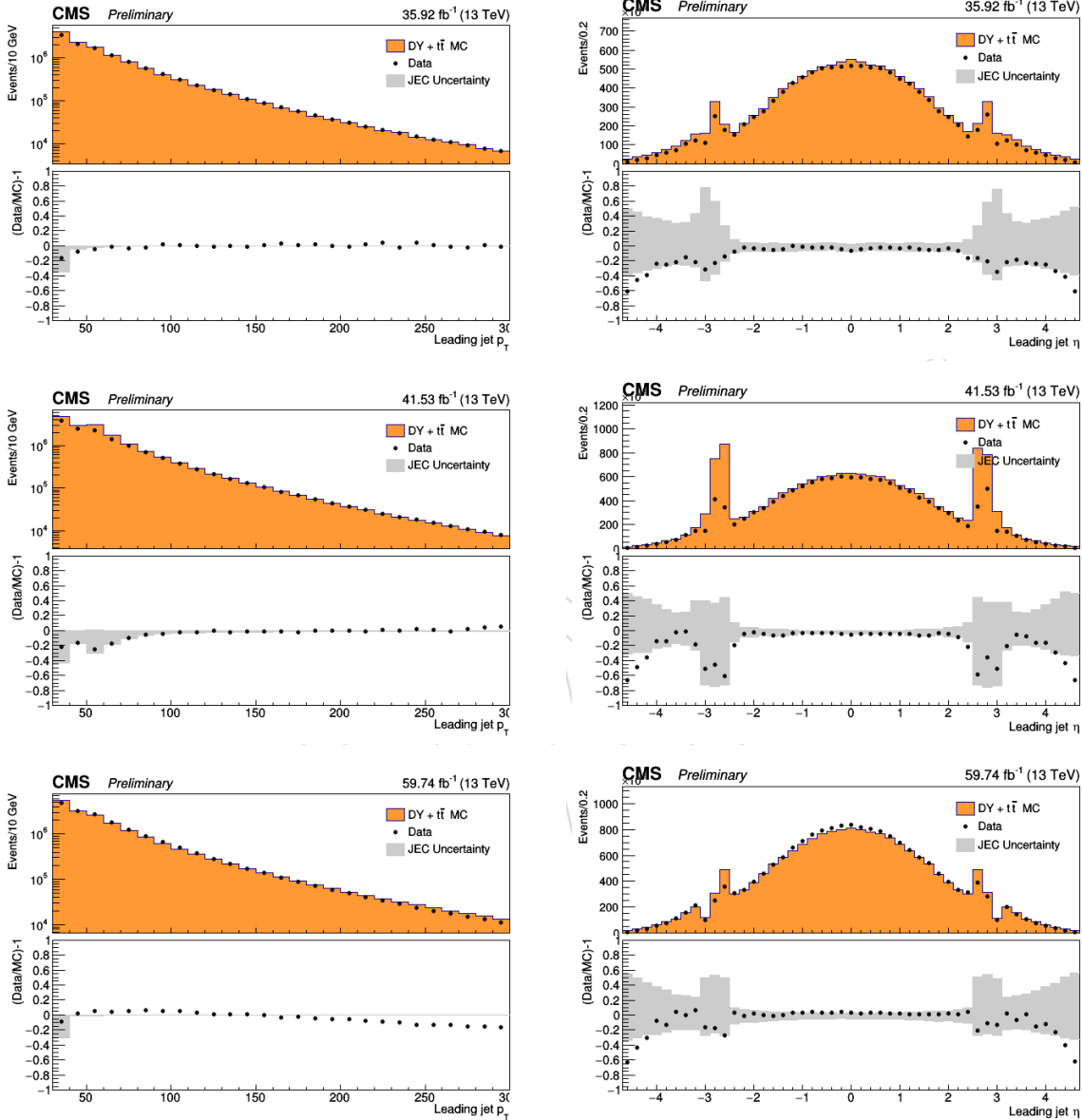


Figure 26: Comparison between data and MC for the leading jet p_T (left) and jet η (right) for 2016 (top), 2017 (middle) and 2018 (bottom). $Z \rightarrow \ell\ell + \text{jets}$ events are used. MC is normalized to data. Jet ID and Jet PUID are applied. MC samples include DY and $t\bar{t}$. Data/MC ratio plots are shown in the bottom of each plots, together with the uncertainties (shaded histograms) from Jet Energy Corrections.

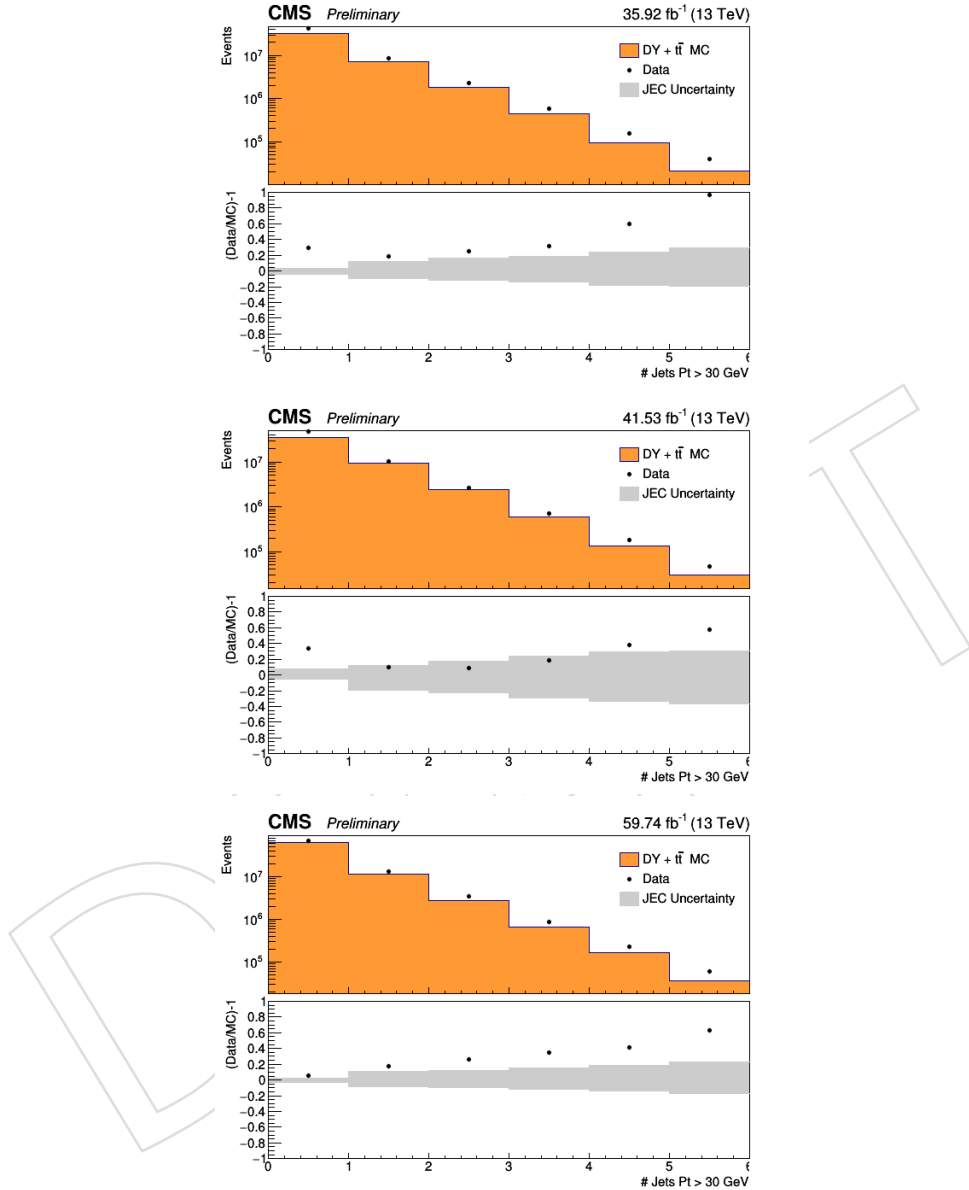


Figure 27: Comparison between data and MC for the jet multiplicity for 2016 (top), 2017 (middle) and 2018 (bottom). $Z \rightarrow \ell\ell + \text{jets}$ events are used. MC is normalized to data. Jet ID and Jet PUID are applied. MC samples include DY and $t\bar{t}$ bar. Data/MC ratio plots are shown in the bottom of each plots, together with the uncertainties (shaded histograms) from Jet Energy Corrections.

449 3.5 Object Summary

- 450 The requirements on all objects used for the analysis with 2016, 2017 or 2018 data are summa-
451 rized in the Table 16. In addition, a “ghost-cleaning” procedure is applied to the muons, as
452 described in Sec. 3.2.1.
- 453 A lepton is declared **loose** if it passes the reconstruction, kinematics and dxy/dz cuts and
454 declared **tight** if it passes in addition the identification, isolation and SIP3D requirements.

DRAFT

Table 16: Summary of physics object selection for the $H \rightarrow ZZ \rightarrow 4\ell$ analysis performed on the 2018 data.

Electrons
$p_T^e > 7 \text{ GeV}$ $ \eta^e < 2.5$
$d_{xy} < 0.5 \text{ cm}$ $d_z < 1 \text{ cm}$
$ SIP_{3D} < 4$
BDT ID with isolation with cuts from Tables 11, 12 and 13
Muons
Global or Tracker Muon
Discard Standalone Muon tracks if reconstructed in muon system only
Discard muons with muonBestTrackType==2 even if they are global or tracker muons
$p_T^- > 5 \text{ GeV}$ $ \eta^\mu < 2.4$
$d_{xy} < 0.5 \text{ cm}$ $d_z < 1 \text{ cm}$
$ SIP_{3D} < 4$
PF muon ID if $p_T < 200 \text{ GeV}$, PF muon ID or High- p_T muon ID (Table 14) if $p_T > 200 \text{ GeV}$
$\mathcal{I}_{\text{PF}}^\mu < 0.35$
FSR photons
$p_T^{\text{fl}} > 2 \text{ GeV}$ $ \eta^\gamma < 2.4$
$\mathcal{I}_{\text{PF}}^\gamma < 1.8$
$\Delta R(\ell, \gamma) < 0.5$ $\frac{\Delta R(\ell, \gamma)}{(p_T^\gamma)^2} < 0.012 \text{ GeV}^{-2}$
Jets
$p_T^{\text{jet}} > 30 \text{ GeV}$ $ \eta^{\text{jet}} < 4.7$
$\Delta R(\ell/\gamma, \text{jet}) > 0.4$
Cut-based jet ID (tight WP)
Jet pileup ID (tight WP)
Deep CSV b-tagging (medium WP)

4 Event Selection

4.1 Trigger Selection

The events are required to have fired the High-Level Trigger paths described in section 2.1.1. Unlike in the Run I analysis, the trigger requirement does not depend on the selected final state: it is always the OR of all HLT paths. The reason is in Run II we will be targeting associated production modes that can come with additional leptons, thus improving trigger efficiency further.

4.2 Vertex Selection

The events are required to have at least one good primary vertex (PV) fulfilling the following criteria: high number of degree of freedom ($N_{PV} > 4$), collisions restricted along the z -axis ($|z_{PV}| < 24$ cm) and small radius of the PV ($r_{PV} < 2$ cm).

4.3 ZZ Candidate Selection

The four-lepton candidates are built from what we call **selected leptons**, which are the tight leptons (defined in sections 3.1.2 and 3.2.1) that pass the $SIP_{3D} < 4$ vertex constraint and the isolation cuts (defined in sections 3.1.2 and 3.2.2), where FSR photons are subtracted as described in Section 3.3. A lepton cross cleaning is applied by discarding electrons which are within $\Delta R < 0.05$ of selected muons.

The construction and selection of four-lepton candidates proceeds according to the following sequence:

1. **Z candidates** are defined as pairs of selected leptons of opposite charge and matching flavour (e^+e^- , $\mu^+\mu^-$) that satisfy $12 < m_{\ell\ell(\gamma)} < 120$ GeV/ c^2 , where the Z candidate mass includes the selected FSR photons if any.

2. **ZZ candidates** are defined as pairs of non-overlapping Z candidates. The Z candidate with reconstructed mass $m_{\ell\ell}$ closest to the nominal Z boson mass is denoted as Z_1 , and the second one is denoted as Z_2 . ZZ candidates are required to satisfy the following list of requirements:

- **Ghost removal** : $\Delta R(\eta, \phi) > 0.02$ between each of the four leptons.
- **lepton p_T** : Two of the four selected leptons should pass $p_{T,i} > 20$ GeV/ c and $p_{T,j} > 10$ GeV/ c . FSR photons are used.
- **QCD suppression**: all four opposite-sign pairs that can be built with the four leptons (regardless of lepton flavor) must satisfy $m_{\ell\ell} > 4$ GeV/ c^2 . Here, selected FSR photons are not used in computing $m_{\ell\ell}$, since a QCD-induced low mass dilepton (eg. J/Ψ) may have photons nearby (e.g. from π_0).
- **Z_1 mass**: $m_{Z_1} > 40$ GeV/ c^2
- **'smart cut'**: defining Z_a and Z_b as the mass-sorted alternative pairing Z candidates (Z_a being the one closest to the nominal Z boson mass), require $\text{NOT}(|m_{Z_a} - m_Z| < |m_{Z_1} - m_Z| \text{ AND } m_{Z_b} < 12)$. Selected FSR photons are included in m_Z 's computations. This cut discards 4μ and $4e$ candidates where the alternative pairing looks like an on-shell Z + low-mass $\ell^+\ell^-$. (NB. In Run I, such a situation was avoided by choosing the best ZZ candidate before applying kinematic cuts to it, most precisely before the $m_{Z_2} > 12$ GeV/ c^2 cut. The present smart cut allows to choose the best ZZ candidate after all kinematic cuts.)

- 497 • **four-lepton invariant mass:** $m_{4\ell} > 70$ GeV/ c^2 (selected FSR photons are in-
498 cluded).

499 3. Events containing at least one selected ZZ candidate form the **signal region**.

500 **4.4 Choice of the best ZZ Candidate**

501 Unlike in the Run I analysis, the best ZZ candidate is now chosen after all kinematic cuts, a
502 change that allows to test other selection strategies for this candidate choice. This is especially
503 relevant for events with more than four selected leptons, having in mind the search for the
504 Higgs boson production modes where associated particles can decay to leptons, such as VH
505 and ttH.

506 For the current analysis, we adopt a different approach compared to Run 1: if more than one
507 ZZ candidate survives the above selection, we choose the one with the highest value of $\mathcal{D}_{\text{bkg}}^{\text{kin}}$
508 (defined in Section ??, except when two candidates consist of the same four leptons in which
509 case the candidate with Z_1 closest in mass to nominal Z boson mass is retained).

DRAFT

5 Background Estimation

5.1 Irreducible Backgrounds

5.1.1 $q\bar{q} \rightarrow ZZ$ Modelling

The $q\bar{q} \rightarrow ZZ$ background is generated at NLO, while the fully differential cross section has been computed at NNLO [46], but are not yet available in a partonic level event generator. Therefore NNLO/NLO k -factors for the $q\bar{q} \rightarrow ZZ$ background process are applied to the POWHEG sample. The inclusive cross sections obtained using the same PDF and renormalization and factorization scales as the POWHEG sample at LO, NLO, and NNLO are shown in Table 17. The NNLO/NLO k -factors are applied in the analysis differentially as a function of $m(ZZ)$.

Additional NLO electroweak corrections which depend on the initial state quark flavor and kinematics are also applied to the $q\bar{q} \rightarrow ZZ$ background process in the region $m(ZZ) > 2m(Z)$ where the corrections have been computed. The differential QCD and electroweak k -factors can be seen in Figure 28.

QCD Order	$\sigma_{2\ell 2\ell'}(\text{fb})$	$\sigma_{4\ell}(\text{fb})$
LO	$218.5^{+16\%}_{-15\%}$	$98.4^{+13\%}_{-13\%}$
NLO	$290.7^{+5\%}_{-8\%}$	$129.5^{+4\%}_{-6\%}$
NNLO	$324.0^{+2\%}_{-3\%}$	$141.2^{+2\%}_{-2\%}$

Table 17: Cross sections for $q\bar{q} \rightarrow ZZ$ production at 13 TeV

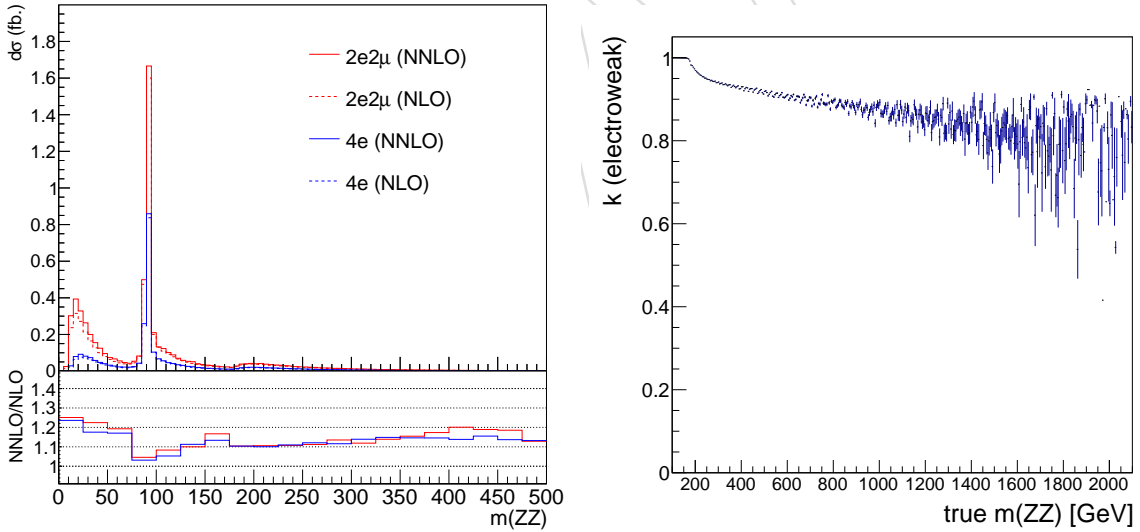


Figure 28: Left: NNLO/NLO QCD K factor for the $q\bar{q} \rightarrow ZZ$ background as a function of $m(ZZ)$ for the 4ℓ and $2\ell 2\ell'$ final states. Right: NLO/NLO electroweak K factor for the $q\bar{q} \rightarrow ZZ$ background as a function of $m(ZZ)$.

5.1.2 $gg \rightarrow ZZ$ Modelling

Event simulation for the $gg \rightarrow ZZ$ background is done at LO with the generator MCFM 7.0 [31, 32, 47]. Although no exact calculation exists beyond the LO for the $gg \rightarrow ZZ$ background, it has been recently shown [48] that the soft collinear approximation is able to describe the

background cross section and the interference term at NNLO. Further calculations also show that the K factors are very similar at NLO for the signal and background [49] and at NNLO for the signal and interference terms [50]. Therefore, the same K factor is used for the signal and background [51]. The NNLO K factor for the signal is obtained as a function of $m_{4\ell}$ using the HNNLO v2 Monte Carlo program [52–54] by calculating the NNLO and LO $gg \rightarrow H \rightarrow 2\ell 2\ell'$ cross sections at the small H boson decay width of 4.07 MeV and taking their ratios. The NNLO as well as the NLO K factors and the cross sections from which they are derived are illustrated in Figure 29, along with the NNLO, NLO and LO cross sections at the SM H boson decay width [55].

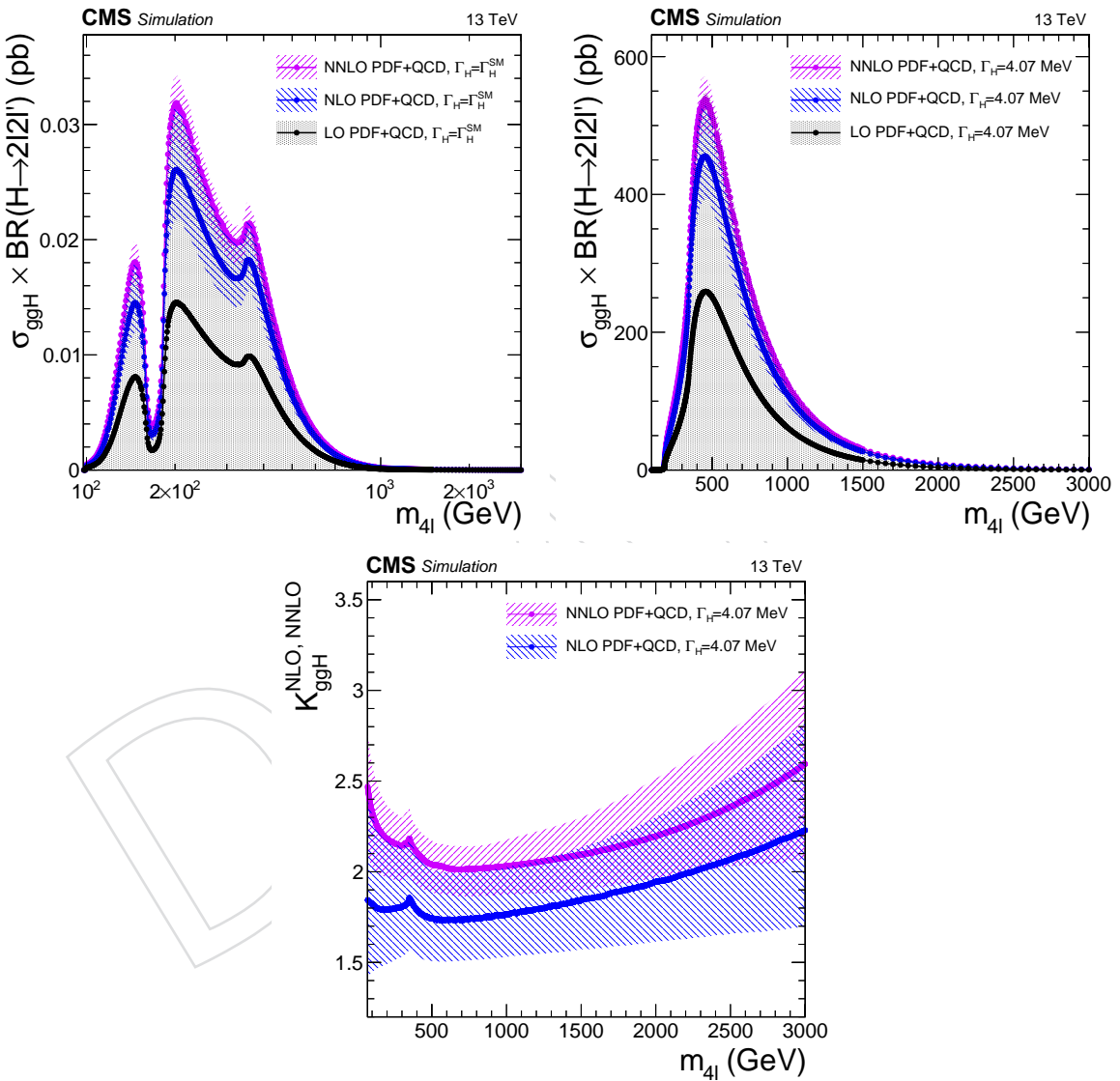


Figure 29: $gg \rightarrow H \rightarrow 2\ell 2\ell'$ cross sections at NNLO, NLO and LO at each H boson pole mass using the SM H boson decay width (top left) or at the fixed and small decay width of 4.07 MeV (top right). The cross sections using the fixed value are used to obtain the K factor for both the signal and the continuum background contributions as a function of $m_{4\ell}$ (bottom).

537 5.2 Reducible Background

538 The reducible background for the $H \rightarrow ZZ \rightarrow 4\ell$ analysis, hereafter called $Z + X$, originates
 539 from processes which contain one or more nonprompt leptons in the four lepton final state. The
 540 main sources of nonprompt leptons are non-isolated electrons and muons coming from decays
 541 of heavy flavour mesons, misreconstructed jets (usually originating from light flavour quarks)
 542 and electrons from γ conversions. In this discussion, we will consider a “fake lepton” any jet
 543 misreconstructed as a lepton and any lepton originating from a heavy meson decay. Similarly,
 544 any electron originating from a photon conversion will be considered a “fake electron”.

545 In the $H \rightarrow ZZ \rightarrow 4\ell$ analysis, the rate of these background processes is estimated by mea-
 546 suring the f_e and f_μ probabilities for fake electrons and fake muons which do pass the **loose**
 547 selection criteria (defined in Section 3.1.1 and 3.2.1) to also pass the final selection criteria (de-
 548 fined in Section 4.3). These probabilities, hereafter referred to as fake ratios or fake rates (FR),
 549 are applied in dedicated control samples in order to extract the expected background yield in
 550 the signal region.

551 In the following section, two independent methods are presented to measure both the yields
 552 and shapes of the reducible background, called Opposite-Sign (OS) method and Same-Sign (SS)
 553 method. The final result combines the outcome of the two approaches. The methods are the
 554 same as in the 2016 analysis, although additional cross checks have been performed.

555 5.2.1 Reducible Background Estimate with Opposite-Sign Leptons

556 **5.2.1.1 Fake Rate Determination (OS method)** In order to measure the lepton fake ra-
 557 tios f_e and f_μ , we select samples of $Z(\ell\ell) + e$ and $Z(\ell\ell) + \mu$ events that are expected to be
 558 completely dominated by final states which include a Z boson and a fake lepton. These events
 559 are required to have two same flavour, opposite charge leptons with $p_T > 20/10$ GeV passing
 560 the tight selection criteria, thus forming the Z candidate. In addition, there is exactly one lep-
 561 ton passing the loose selection criteria as defined above. This lepton is used as the probe lepton
 562 for the fake ratio measurement. The invariant mass of this lepton and the opposite sign lepton
 563 from the reconstructed Z candidate should satisfy $m_{2l} > 4$ GeV.

564 The fake ratios are evaluated using the tight requirement $|M_{inv}(\ell_1, \ell_2) - M_Z| < 7$ GeV, to re-
 565 duce the contribution from photon (asymmetric) conversions populating low masses. The fake
 566 ratios are measured in bins of the transverse momentum of the loose lepton in the barrel and
 567 endcap regions. The electron and muon fake rates are measured within $|M_{inv}(\ell_1, \ell_2) - M_Z| <$
 568 7 GeV and $E_T^{\text{miss}} < 25$ GeV, separately for the 2016, 2017 and 2018 data, and are shown in
 569 Figure 30.

570 **5.2.1.2 Fake Rate Application (OS method)** Two control samples are obtained as sub-
 571 sets of the four lepton events which pass the first step of the selection (*First Z step*, see sec-
 572 tion 4.3), requiring an additional pair of identified loose leptons of same flavour and opposite
 573 charge, that pass the SIP_{3D} , dxy and dz cuts. The events must satisfy all kinematic cuts applied
 574 for the *Higgs phase space* selection (see 4.3).

575 The first control sample is obtained by requiring that the two loose leptons, which do not make
 576 the Z_1 candidate, do not pass the final selection criteria, while the other two leptons pass the
 577 final selection criteria by definition of the Z_1 . This sample is denoted as “2 Prompt + 2 Fail”
 578 (2P+2F) sample. It is expected to be populated with events that intrinsically have only two
 579 prompt leptons (mostly DY , with a small fraction of $t\bar{t}$ and $Z\gamma$ events). The second control
 580 sample is obtained by requiring one of the four leptons not to pass the final identification crite-
 581 ria and selection cuts on SIP , dxy and dz and is denoted as “3 Prompt + 1 Fail” (3P+1F) sample.

582 The other three leptons should pass the final selection criteria.

583 It is expected to be populated with the type of events that populate the 2P+2F region, albeit with
584 different relative proportions, as well as with WZ events that intrinsically have three prompt
585 leptons.

586 The control samples obtained in this way, orthogonal by construction to the signal region, are
587 enriched with fake leptons and are used to estimate the reducible background in the signal
588 region. The invariant mass distribution of events selected in the 2P+2F control sample is shown
589 in Figures 31, 32 and 33.

590 The expected number of reducible background events in the 3P+1F region, N_{3P1F}^{bkg} , can be com-
591 puted from the number of events observed in the 2P+2F control region, N_{2P2F} , by weighting
592 each event in the region with the factor $(\frac{f_i}{1-f_i} + \frac{f_j}{1-f_j})$, where f_i and f_j correspond to the fake
593 ratios of the two loose leptons:

$$N_{3P1F}^{bkg} = \sum \left(\frac{f_i}{1-f_i} + \frac{f_j}{1-f_j} \right) N_{2P2F} \quad (2)$$

594 Figures 34, 35 and 36 shows the invariant mass distributions of the events selected in the 3P+1F
595 control sample, together with the expected reducible background estimated from Eq. 2, stacked
596 on the distribution of WZ and of irreducible background ($ZZ, Z\gamma^* \rightarrow 4\ell$) taken from the sim-
597 ulation.

598 Would the fake rates be measured in a sample that has exactly the same background compo-
599 sition as the 2P+2F sample, the difference between the observed number of events in the 3P+1F
600 sample and the expected background predicted from the 2P+2F sample would solely amount
601 to the (small) WZ and $Z\gamma_{conv}$ contribution. Large differences arise because the fake rates used
602 in Eq. 2 do not properly account for the background composition of the 2P+2F control sample.

603 In particular, the difference seen in Figure 36 between the observed 3P+1F distribution and the
604 expectation from 2P+2F, in the channels with loose electrons (4e and 2 μ 2e), and concentrated
605 at low masses, is due to photon conversions. This is confirmed explicitly by the simulation.
606 The difference between the 3P+1F observation and the prediction from 2P+2F to recover the
607 missing contribution from conversions - and more generally, in principle, to "correct" for the
608 fact that the fake rates do not properly account for the background composition of the 2P+2F
609 sample. More precisely, the expected reducible background in the signal region is given by the
610 sum of two terms :

- 611 • a "2P2F component", obtained from the number of events observed in the 2P+2F
612 control region, N_{2P2F} , by weighting each event in that region with the factor $\frac{f_i}{1-f_i} \frac{f_j}{1-f_j}$,
613 where f_i and f_j correspond to the fake ratios of the two loose leptons;
- 614 • a "3P1F component", obtained from the difference between the number of observed
615 events in the 3P+1F control region, N_{3P1F} , and the expected contribution from the
616 2P+2F region and ZZ processes in the signal region, $N_{3P1F}^{ZZ} + N_{3P1F}^{bkg}$. The N_{3P1F}^{bkg} is
617 given by Eq. 2 and N_{3P1F}^{ZZ} is the contribution from ZZ which is taken from the sim-
618 ulation. The difference $N_{3P1F} - N_{3P1F}^{bkg} - N_{3P1F}^{ZZ}$, which may be negative, is obtained
619 for each (p_T, η) bin of the "F" lepton, and is weighted by $\frac{f_i}{1-f_i}$, where f_i denotes the
620 fake rate of this lepton. This "3P1F component" accounts for the contribution of re-
621 ductible background processes with only one fake lepton (like WZ events), and for

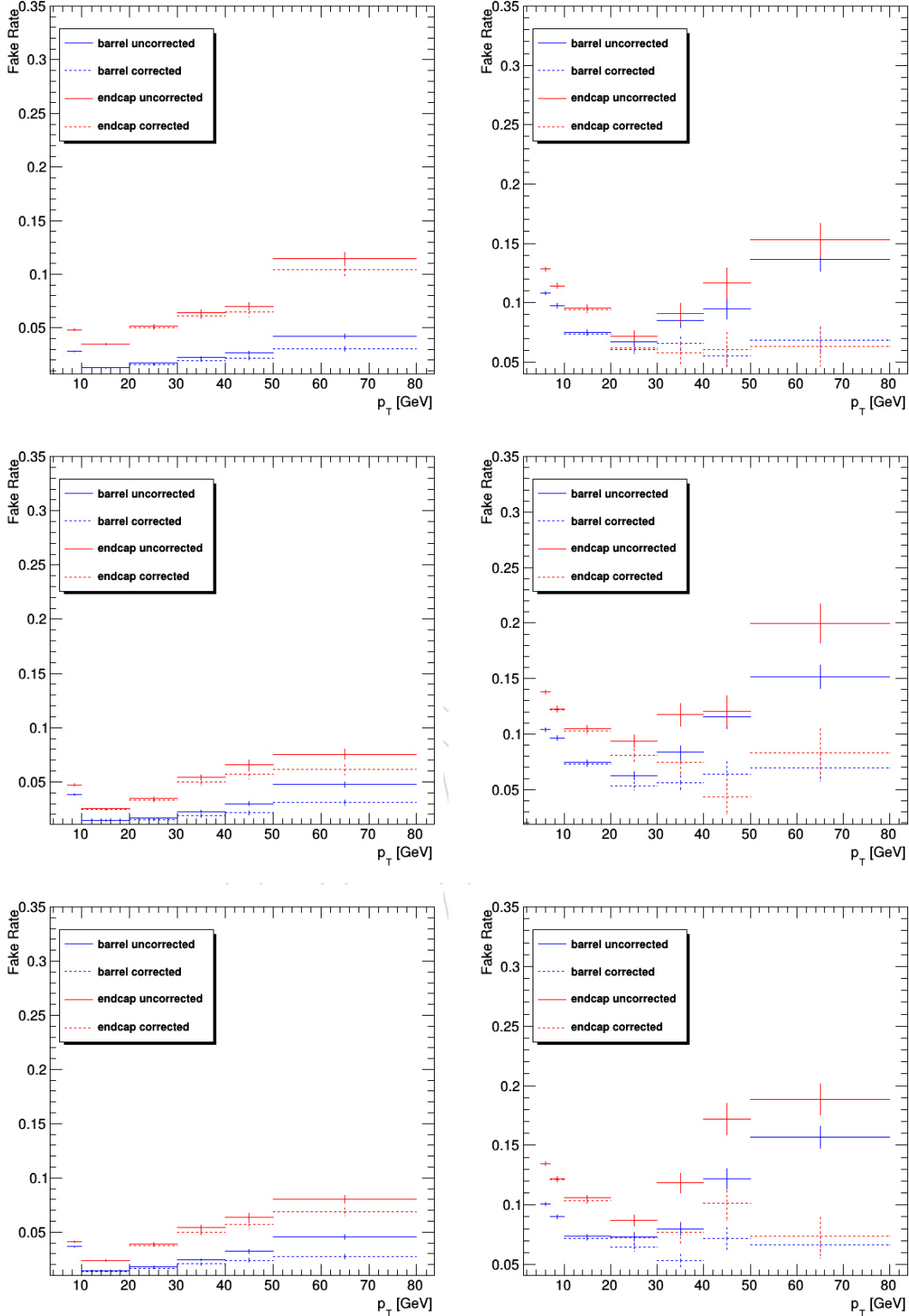


Figure 30: Fake rates as a function of the probe p_T for electrons (left) and muons (right) which satisfy the loose selection criteria, measured in a $Z(\ell\ell) + \ell$ sample in the 2016 (top), 2017 (middle) and 2018 (bottom) data at 13 TeV. The barrel selection includes electrons (muons) up to $|\eta| = 1.479$ (1.2). The fake rates are shown before (dotted lines) and after (plain line) removal of WZ contribution from MC.

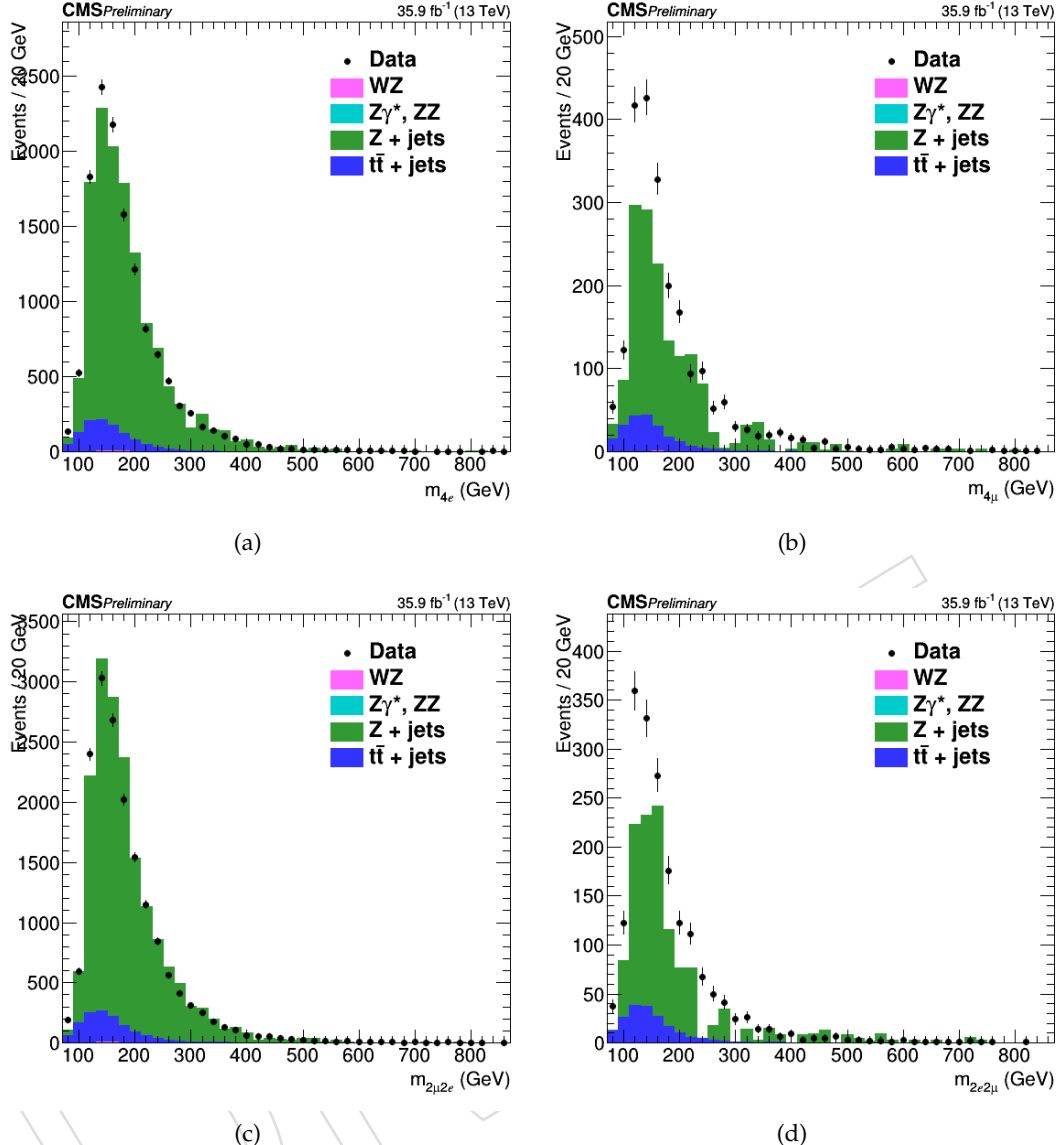


Figure 31: Invariant mass distribution of the events selected in the 2P+2F control sample in the 2016 dataset for all the considered channels: 4e (a), 4 μ (b), 2 μ 2e (c) and 2e2 μ (d).

622 the contribution of other processes (e.g. photon conversions) that are not properly
 623 estimated by the 2P2F component, because of the fake rates used.

Therefore, the full expression for the prediction can be symbolically written as:

$$N_{\text{SR}}^{\text{bkg}} = \sum_i \frac{f_i}{(1-f_i)} (N_{\text{3P1F}} - N_{\text{3P1F}}^{\text{bkg}} - N_{\text{3P1F}}^{\text{ZZ}}) + \sum_j \frac{f_i}{(1-f_i)} \frac{f_j}{(1-f_j)} N_{\text{2P2F}} \quad (3)$$

Previous equation is equivalent to the following:

$$N_{\text{SR}}^{\text{bkg}} = \left(1 - \frac{N_{\text{3P1F}}^{\text{ZZ}}}{N_{\text{3P1F}}}\right) \sum_j \frac{f_a^j}{1-f_a^j} - \sum_i \frac{f_3^i}{1-f_3^i} \frac{f_4^i}{1-f_4^i} \quad (4)$$

624 For channels where the Z_2 candidate is made from two electrons, the contribution of the 3P1F
 625 component is positive, and amounts to typically 30% of the total predicted background.

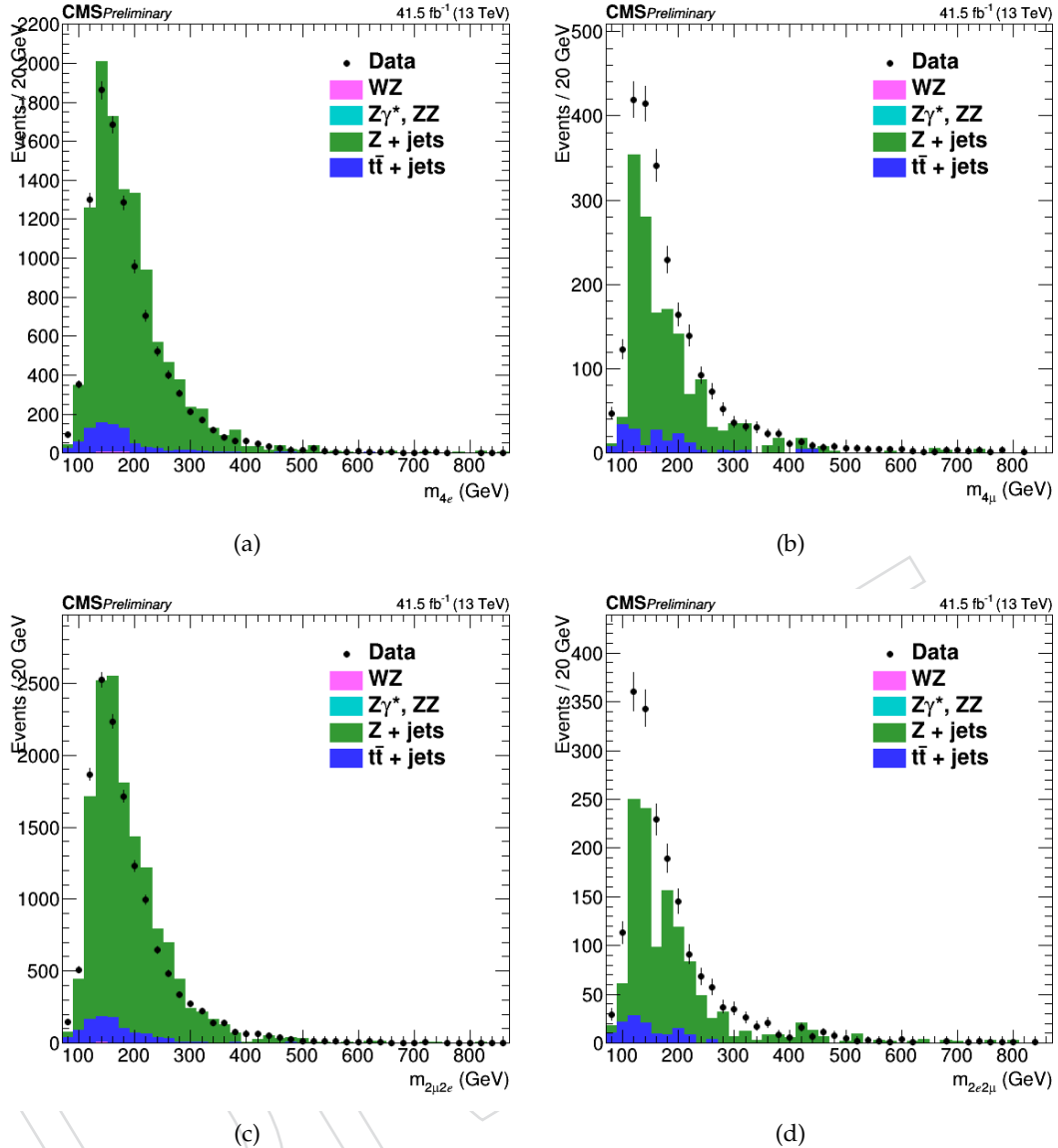


Figure 32: Invariant mass distribution of the events selected in the 2P+2F control sample in the 2017 dataset for all the considered channels: 4e (a), 4 μ (b), 2 μ 2e (c) and 2e2 μ (d).

- 626 For channels with loose muons (4 μ and 2e2 μ), the 3P+1F sample is rather well described by
 627 the prediction from 2P+2F, as seen in Figure 36, and the 3P1F component is mainly driven by
 628 statistical fluctuations in the 3P+1F sample, which are larger than the expectation from WZ
 629 production.
 630 Table 18 shows the expected number of events in the signal regions from the reducible back-
 631 ground processes at 13 TeV for each considered final state and for all three years using the OS
 632 method. The invariant mass distribution of the ZX events obtained from the combination of
 633 the results in the 2P+2F and 3P+1F control samples are shown in Figure 37, 38, 39.

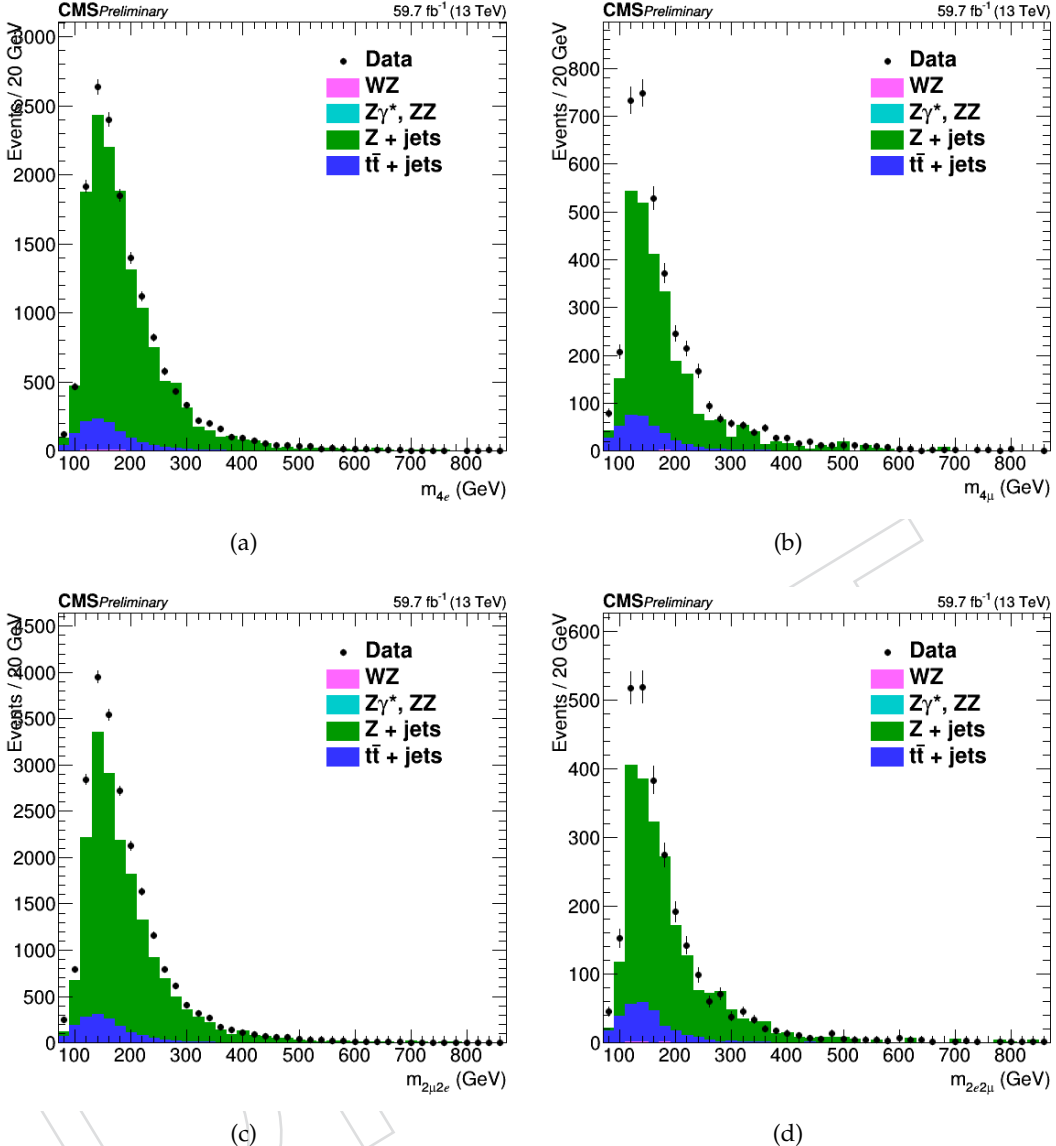


Figure 33: Invariant mass distribution of the events selected in the 2P+2F control sample in the 2018 dataset for all the considered channels: 4e (a), 4 μ (b), 2 μ 2e (c) and 2e2 μ (d).

Channel	4e	4 μ	2e2 μ	2 μ 2e
2016	20.1 ± 6.1	26.9 ± 8.6	25.2 ± 8.0	22.3 ± 6.8
2017	16.2 ± 5.0	32.7 ± 10.3	24.0 ± 7.7	21.3 ± 6.5
2018	25.4 ± 7.7	49.4 ± 15.4	34.2 ± 10.7	33.0 ± 10.0

Table 18: The contribution of reducible background processes in the signal region predicted from measurements in 2016, 2017 and 2018 data using the OS method. The predictions correspond to 35.9 , 41.5 and 59.7 fb^{-1} of data at 13 TeV, respectively.

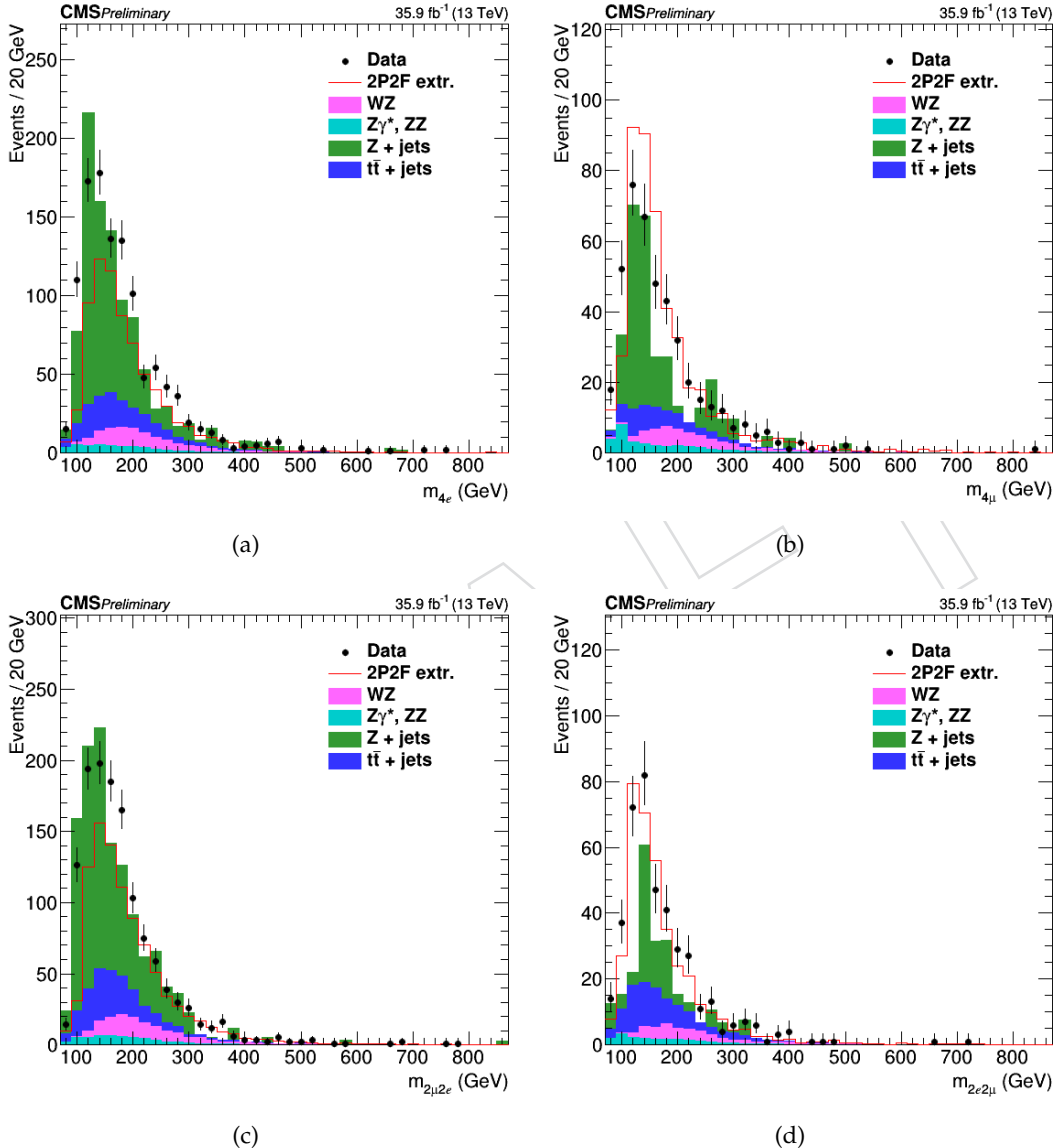


Figure 34: Invariant mass distribution of the events selected in the 3P+1F control sample in the 2016 dataset for all the considered channels: 4e (a), 4μ (b), 2μ2e (c) and 2e2μ (d).

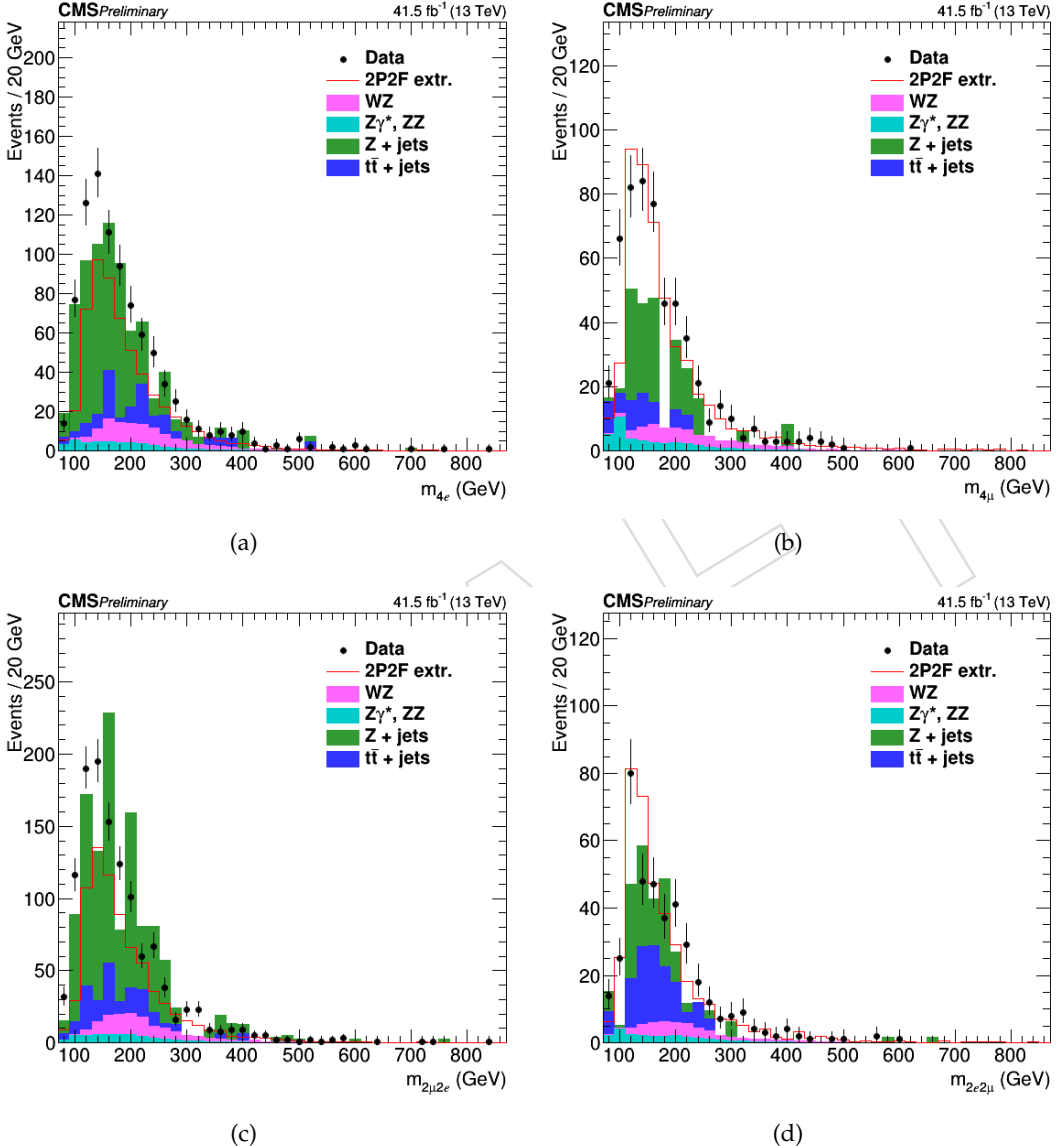


Figure 35: Invariant mass distribution of the events selected in the 3P+1F control sample in the 2017 dataset for all the considered channels: 4e (a), 4 μ (b), 2 μ 2e (c) and 2e2 μ (d).

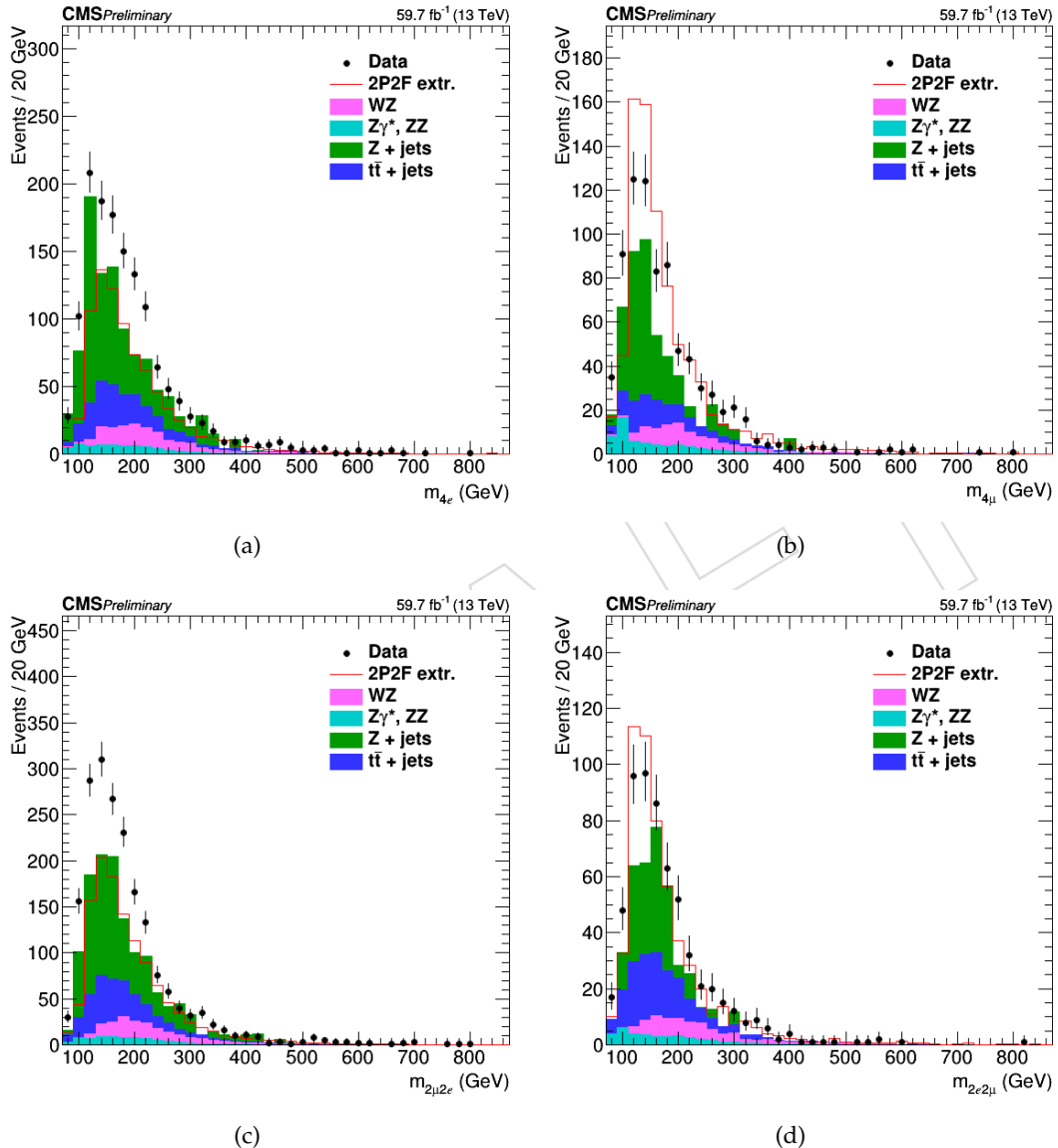


Figure 36: Invariant mass distribution of the events selected in the 3P+1F control sample in the 2018 dataset for all the considered channels: 4e (a), 4 μ (b), 2 μ 2e (c) and 2e2 μ (d).

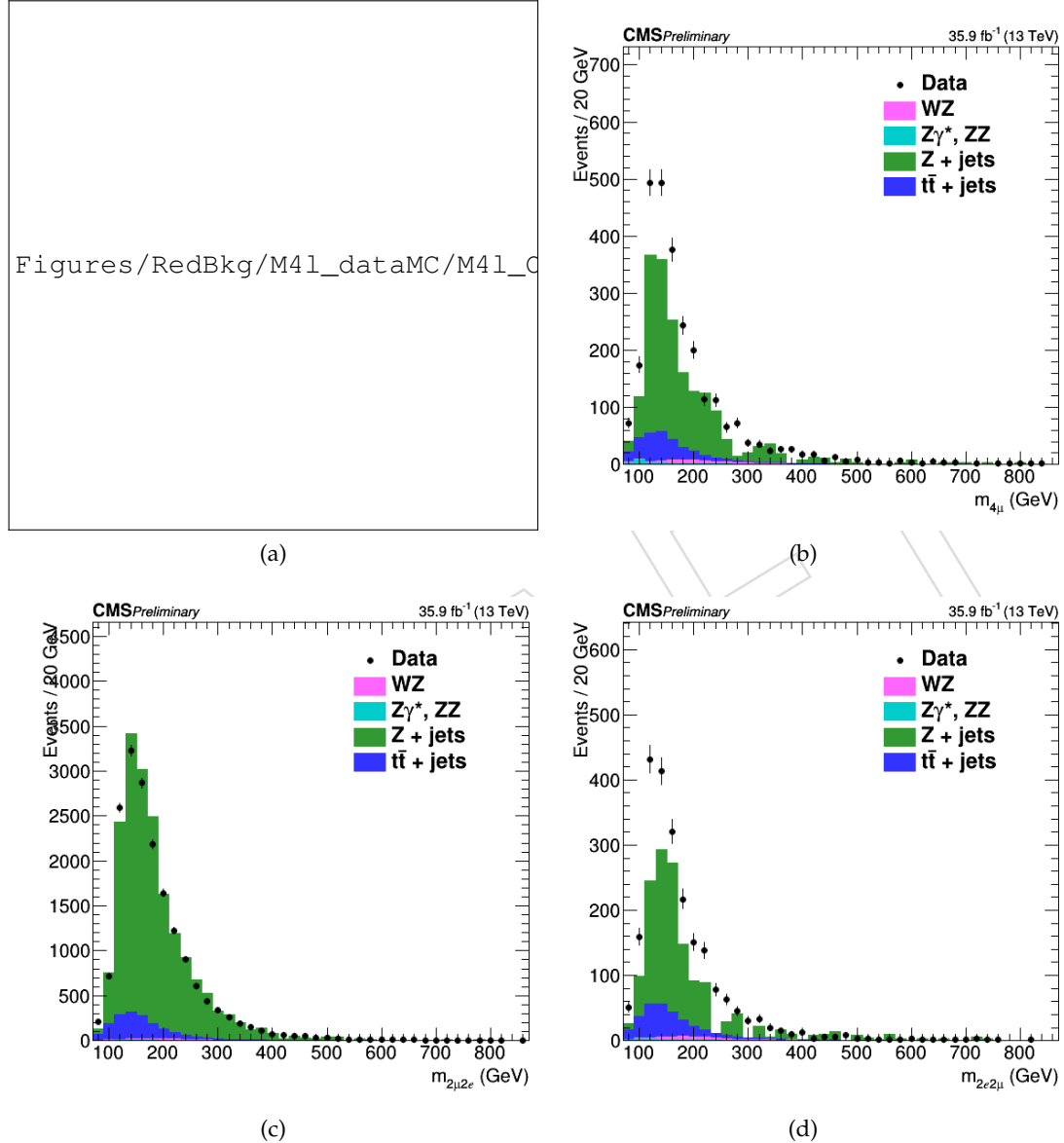


Figure 37: Invariant mass distribution of the events selected in the 2P+2F and 3P+1F control samples in the 2018 dataset for all the considered channels: 4e (a), 4 μ (b), 2 μ 2e (c) and 2e2 μ (d) for 2016 data.

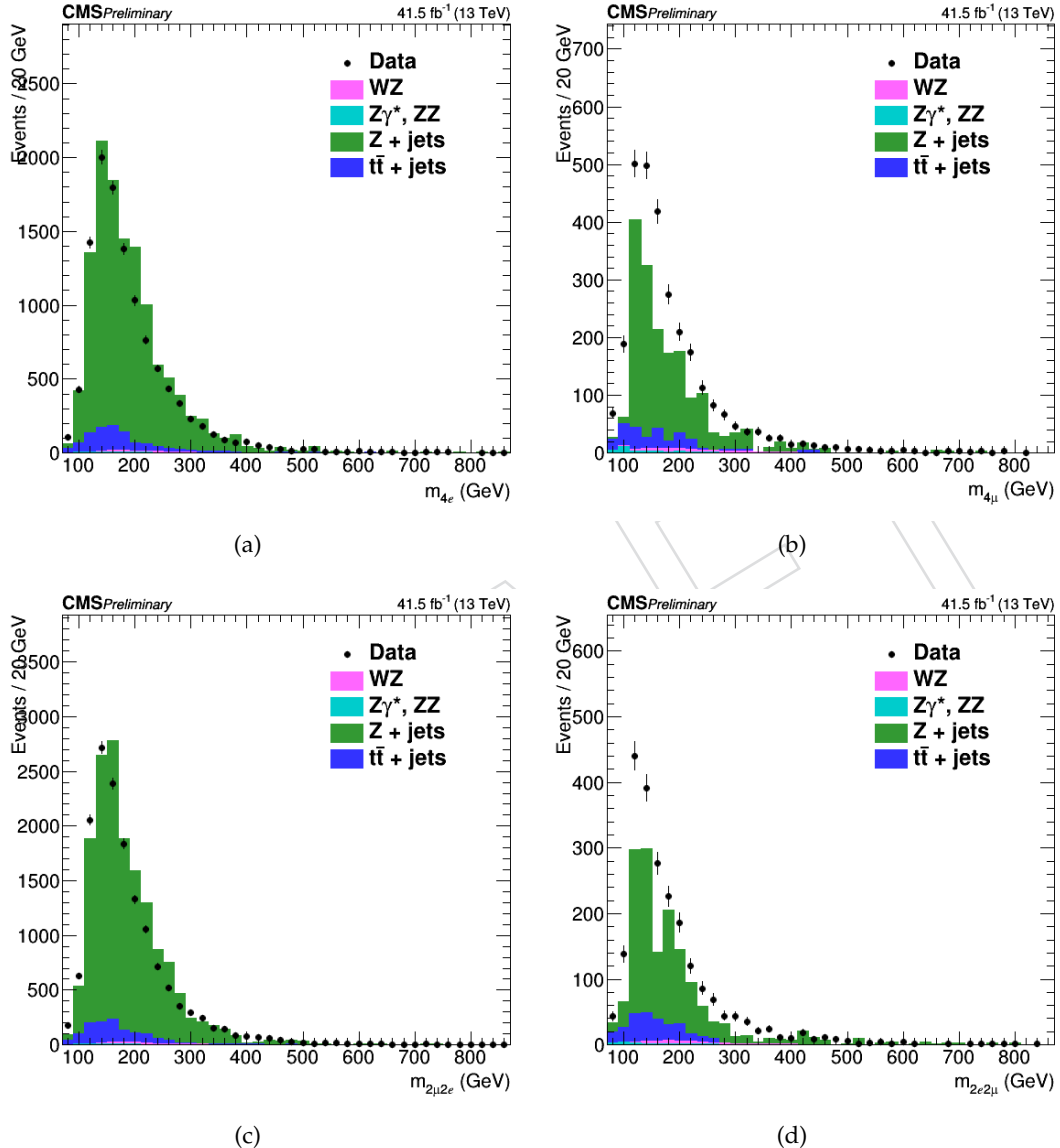


Figure 38: Invariant mass distribution of the events selected in the 2P+2F and 3P+1F control samples in the 2018 dataset for all the considered channels: 4e (a), 4μ (b), 2μ2e (c) and 2e2μ (d) for 2017 data.

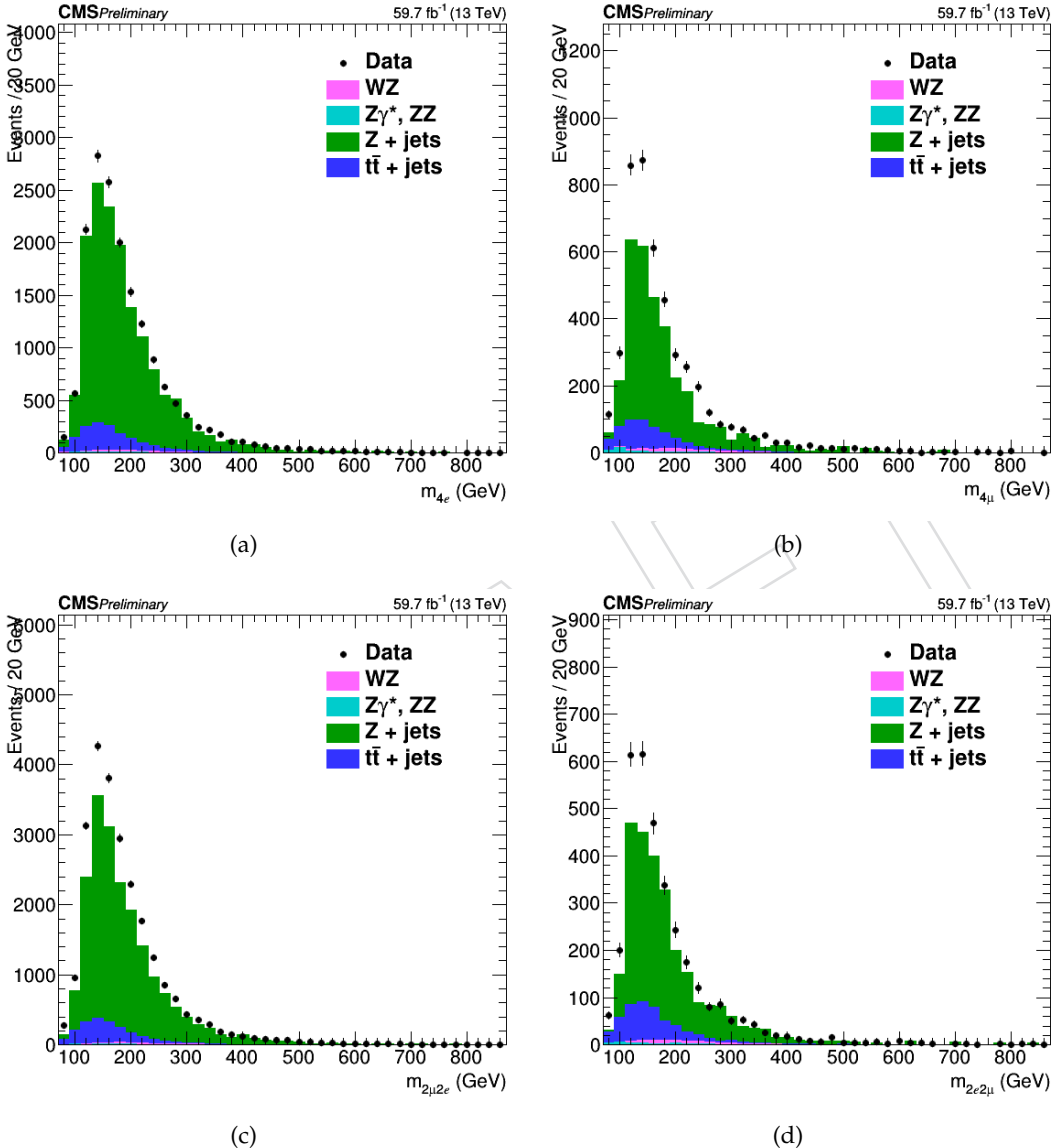


Figure 39: Invariant mass distribution of the events selected in the 2P+2F and 3P+1F control samples in the 2018 dataset for all the considered channels: 4 e (a), 4 μ (b), 2 μ 2 e (c) and 2 e 2 μ (d) for 2018 data.

5.2.2 Reducible Background Estimate with Same-Sign Leptons

This method used to predict the reducible background allows to have an inclusive measurement of all the main reducible backgrounds at the same time.

The control sample is obtained as a subset of the events that satisfy the first step of the selection (*First Z step*, see section 4.3), requiring an additional pair of loose leptons of same sign (to avoid signal contamination) and same flavour (SS-SF: $e^\pm e^\pm, \mu^\pm \mu^\pm$). The SS-SF leptons are requested to pass the SIP_{3D} , dxy and dz cuts, while no identification requirements are imposed. The reconstructed invariant mass of the SS-SF leptons has to satisfy $m_{\ell\ell} > 12$ GeV, $m_{\ell\ell} < 120$ GeV, the reconstructed four-lepton invariant mass is required to satisfy $m_{4\ell} > 100$ GeV/ c^2 , and the QCD suppression cut (see 4.3) is applied. The inclusive number of reducible background events in the signal region is derived from this set of events and from the probability for the two additional leptons to pass the isolation and identification analysis cuts, obtained from the fake rate measurement presented in section 5.2.2.1.

Starting from the control sample previously described, the final reducible background prediction in the signal region is given by the following expression:

$$N_{\text{expect}}^{Z+X} = N^{\text{DATA}} \times \left(\frac{\text{OS}}{\text{SS}}\right)^{\text{MC}} \times f_1 \times f_2 \quad (5)$$

where:

- N^{DATA} is the number of events in the control region,
- $\left(\frac{\text{OS}}{\text{SS}}\right)^{\text{MC}}$ is a correction factor between opposite sign and same sign control samples,
- f_1 and f_2 are the fake rates of each additional loose lepton, parameterised as a function of p_T and η .

5.2.2.1 Fake Rate Determination (SS method)

The lepton fake rates are determined in the very similar way as it was described before for the OS method. Samples of $Z(\ell\ell) + e$ and $Z(\ell\ell) + \mu$ events are selected in the same way except that the mass window around the nominal Z mass is set to $40 \text{ GeV} < M_{\text{inv}}(\ell_1, \ell_2) < 120 \text{ GeV}$, as in the signal region ("SS phase space"). Despite the cut on the missing transverse energy, a contamination of real leptons from WZ events is still visible at high p_T . This contribution is thus subtracted from the final fake rate, using the estimation given by the Monte Carlo. The fake rates for muon are shown in Figure 40 for both muons in the barrel ($|\eta| < 1.2$) and in the endcaps ($|\eta| > 1.2$).

For electrons, events where a radiated photon makes an asymmetric conversion, where one low p_T leg is not identified, contribute to the $Z + e$ sample that is used to measure the electron fake rate. While the requirement $|M_{\text{inv}}(\ell_1, \ell_2) - M_Z| < 7 \text{ GeV}$ ("OS phase space") largely suppresses FSR of photons radiated off the lepton legs, these radiations occur at a much larger rate in the "SS phase space". As a result of this enhanced contribution from conversions, the electron fake rates measured within the SR phase space are larger than the "OS fake rates".

However, the relative fraction of FSR conversions is not the same in the "SS phase space" and in the control sample (defined below) where the fake rates will be applied. A correction accounting for this difference must be applied to the fake rates measured within the SS phase space, in order to obtain average fake rates that are appropriate for the control sample. To determine this correction, several fake rate samples of $Z(l\bar{l}) + e$ events are defined by applying different cuts on $M_{\text{inv}}(\ell_1, \ell_2)$ or on $M_{\text{inv}}(\ell_1, \ell_2, e)$. In addition to the "OS fake rate sample", where $|M_{\text{inv}}(\ell_1, \ell_2) - M_Z| < 7 \text{ GeV}$ ensures a minimal amount of conversions from FSR photons, one defines a sample that is maximally enriched in FSR conversions by $|M_{\text{inv}}(\ell_1, \ell_2, e) - M_Z| < 5 \text{ GeV}$, as well as samples with an intermediate contamination from

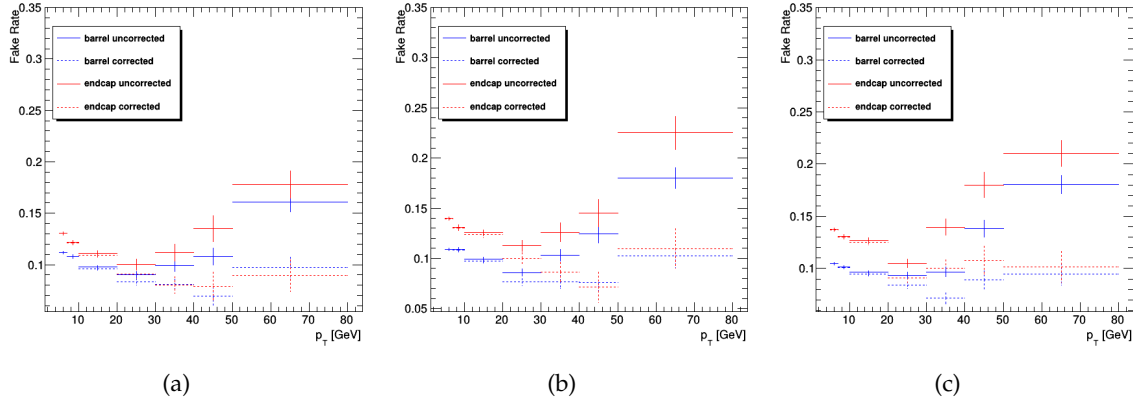


Figure 40: Fake rates as a function of the probe p_T for muons which satisfy the loose selection criteria, measured in a $Z(\ell\ell) + \ell$ sample in the 2016 (top), 2017 (middle) and 2018 (bottom) data at 13 TeV. The barrel selection includes electrons (muons) up to $|\eta| = 1.479$ (1.2). The fake rates are shown before (dotted lines) and after (plain line) the removal of the WZ contribution from the simulation.

675 FSR conversions ($60 \text{ GeV} < M_{\text{inv}}(\ell_1, \ell_2) < 120 \text{ GeV}$). In each sample, one determines in several
676 (p_T, η) bins for the loose electron:

- 677
 - the fake rate ratio;
678 - the average value of the expected inner missing hits ($N_{\text{miss.hits}}$ in the following), vari-
679 able useful to tag conversions.

680 In a given (p_T, η) bin, both the measured fake rate and the average $\langle N_{\text{miss.hits}} \rangle$ are expected
681 to grow linearly with the fraction of conversions. Hence, one expects a linear dependence of
682 the fake rate with respect to $\langle N_{\text{miss.hits}} \rangle$. This linear behaviour is demonstrated in Figure 41,
683 and linear fits are made in each (p_T, η) bin, which relate the fake rate to $\langle N_{\text{miss.hits}} \rangle$. Finally,
684 one looks at the loose electrons in the control sample where the fake rate will be applied, and
685 $\langle N_{\text{miss.hits}} \rangle$ is measured in each (p_T, η) bin. The proper average fake rate corresponding to
686 the control sample is then determined from the linear relation derived previously. Figure 42
687 shows examples of the resulting corrected fake rates, together with the fake rates measured
688 in the SS phase space. It can be seen that the correction for the actual fraction of conversions
689 that is present in the control sample lowers the fake rates considerably with respect to what is
690 measured in the SS phase space. The determination of these corrected fake rates mostly suffers
691 from the limited statistics of the control sample, which translates into a large uncertainty on
692 $\langle N_{\text{miss.hits}} \rangle$, the error on each dot being the fake rate obtained from the linear relations using
693 the error on the $\langle N_{\text{miss.hits}} \rangle$.

694 **5.2.2.2 Fake Rate Application (SS method)** Figure 43 shows the invariant mass distri-
695 bution of events in control samples with SS-SF loose leptons, for channels with loose electrons
696 ($4e$ and $2\mu 2e$) and channels with loose muons (4μ and $2e 2\mu$), for the 2018 dataset at 13 TeV. The
697 prediction from the Monte Carlo simulation is also shown.

698 A good agreement is achieved between data and MC for the channels with loose electrons. The
699 agreement is not as good for loose muons but this has no impact on the final result as only data
700 are used in the end.

701 The differences in rates between OS and SS samples are estimated using data and are used to

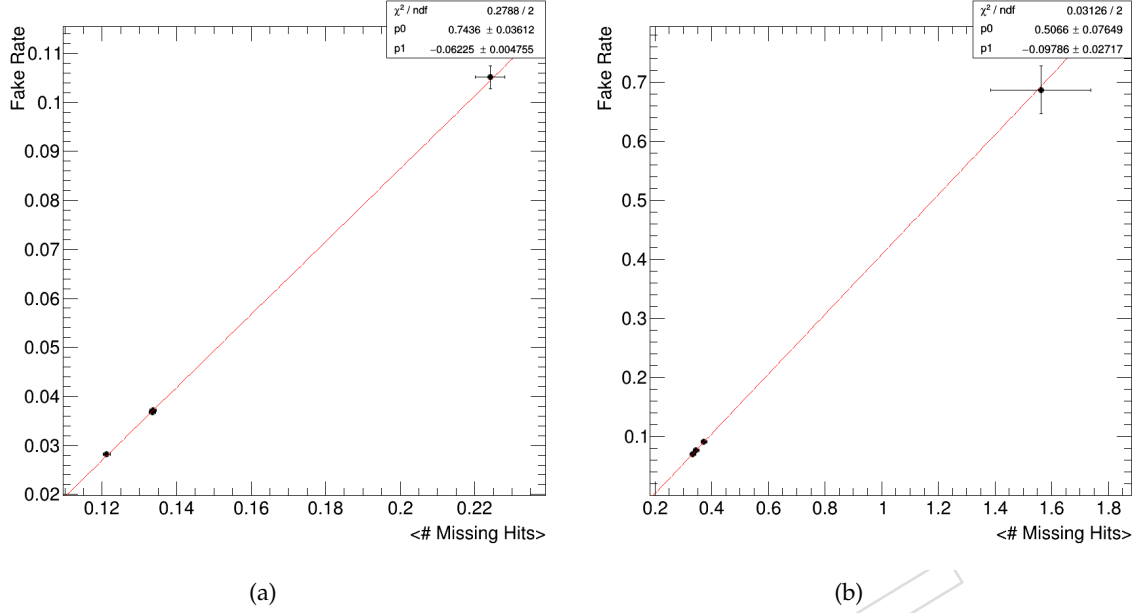


Figure 41: Examples of the correlation between the fake rate and the fraction of loose electrons for which the track has one missing hit in the pixel detector for $7 < p_T < 10$ GeV electrons in the barrel (left) and for $30 < p_T < 40$ GeV electrons in the endcaps (right). Each dot shows the measurements made in a given $Z + \text{loose } e$ sample. Results are produced at 13 TeV with 35.9 fb^{-1} data.

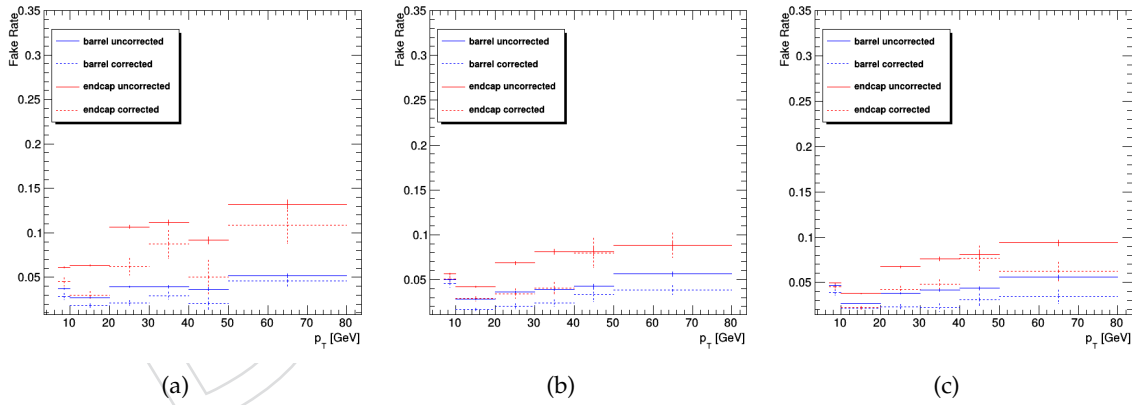


Figure 42: Average fake rates to be applied to the control sample of SS method (plain line), compared to the fake rates measured in the SS phase space (dotted line), for electrons in the barrel (blue) and in the endcaps (red). Results are produced at 13 TeV with 2016, 2017, and 2018 data.

702 compute the correction factor in Eq. 5 for the final data-driven estimation. They are given for
703 each year in Table 19.

704 The event yields expected from the $Z+X$ in the signal region, in the mass range $m_{4\ell} > 70$ GeV/c^2 ,
705 are calculated for each final state. The background is due to the systematic introduced when es-
706 timating the background composition. The total error is obtained with a quadrature sum for the
707 statistical, background composition and correction systematics. Table 20 shows the expected

Channel	4e	2 μ 2e	4 μ	2e2 μ
2016	1.00 ± 0.01	1.00 ± 0.01	1.00 ± 0.03	1.00 ± 0.03
2017	1.01 ± 0.01	1.00 ± 0.01	1.04 ± 0.03	1.01 ± 0.03
2018	1.01 ± 0.01	1.00 ± 0.01	1.03 ± 0.02	1.03 ± 0.02

Table 19: The OS/SS ratios used to estimate the number of ZX events with the SS method for each final state in all three years.

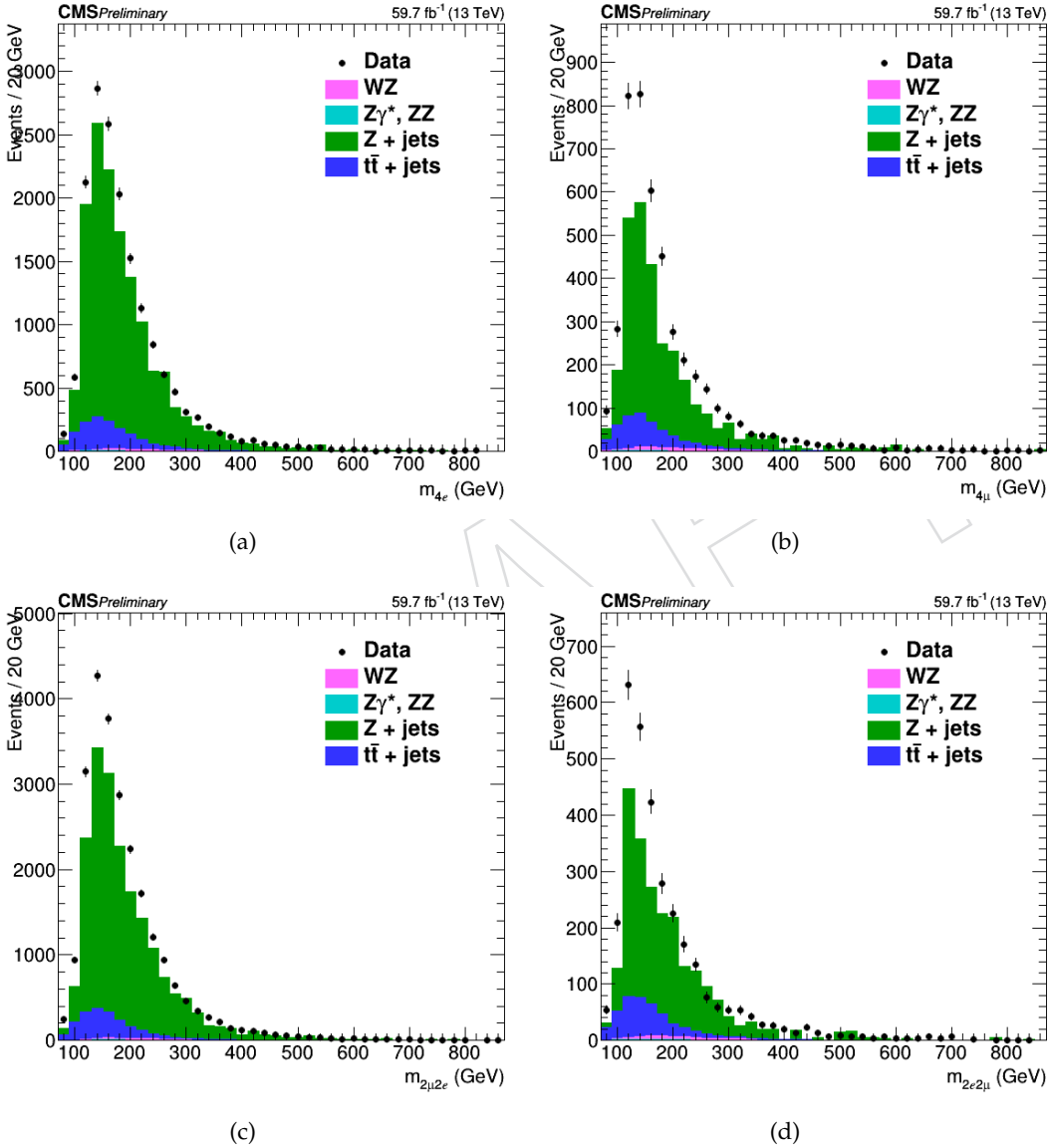


Figure 43: Invariant mass distribution of the events selected in the SS-SF control samples for all the considered final states in 2018 data: 4e (a), 4 μ (b), 2 μ 2e (c) and 2e2 μ (d).

708 number of events in the signal regions from the reducible background processes at 13 TeV for
 709 each considered final state and for all three years using the SS method.

Channel	4e	4 μ	2e2 μ	2 μ 2e
2016	13.0 ± 5.4	29.7 ± 9.1	24.8 ± 7.6	16.7 ± 7.0
2017	10.9 ± 4.0	33.6 ± 10.3	26.3 ± 8.1	14.7 ± 5.5
2018	16.0 ± 5.9	52.2 ± 15.8	37.4 ± 11.4	23.3 ± 8.5

Table 20: The contribution of reducible background processes in the signal region predicted from measurements in 2016, 2017 and 2018 data using the SS method. The predictions correspond to 35.9, 41.5 and 59.7 fb^{-1} of data at 13 TeV, respectively.

710 **5.2.2.3 Fake Rate in the VBF-tagged categories** The FR are currently evaluated inclu-
 711 sively in the analysis: in fact, an average fake rate is used to evaluate ZX yields in each STXS
 712 category instead of dedicated ones. Given that the VBF category can be particularly affected by
 713 this approach, a detailed study of the FR variation in different Z+L phase spaces designed to
 714 mimic VBF has been performed using 2018 data. However, a realistic design of the VBF phase
 715 space is not completely reproducible in the three leptons CR without exploiting the informa-
 716 tion given by the kinematic discriminants. In order to identify events targeting VBF-tagged
 717 categories, the following requirements on jets are applied:

- 718 • an angular separation between the additional lepton and each jet larger than 0.4,
 719 otherwise the jet is discarded;
- 720 • the presence of two or three jets and at most one b tagged jet OR at least four jets
 721 without b tagged jets;
- 722 • an angular separation between the pair of two leading jets larger than 0.5 and a dijet
 723 invariant mass greater than 450 GeV.

724 Furthermore, FR in the CR Z+L with 0/1/2 jets have been studied as well as the FR in the
 725 phase space complementary to the VBF-like one. Figure 45 shows the FR curves obtained
 726 in each category for both electrons and muons in the barrel and endcap region using the SS
 727 method and Figure ?? shows the same distributions using the OS method. While the curve
 728 in the "non VBF-tagged" region is perfectly in agreement with the inclusive one (as a result
 729 of the contribution of the 0/1/2 jet categories), the FR variation in the 0/1/2 jets and VBF-
 730 like categories is significant, especially for muons. As a consequence, large discrepancies are
 731 observed in the final estimated yields in VBF categories (Table 21).

732 In principle, the uncertainty on the background composition of the CR was designed to cover
 733 for this effect, but considering that the effect seems very large, the possible impact on the anal-
 734 ysis has been checked explicitly. An extreme situation has been studied by inflating the Z+X
 735 uncertainty by 100% in the datacards in VBF-tagged categories and comparing stage 0 signal
 736 strengths, both expected and observed, using the standard Z+X uncertainty and inflating it in
 737 VBF categories (Table 22). The results show that the expected uncertainty does not change and
 738 the observed signal strengths change only very slightly (2nd digit) within the uncertainties.

739 In conclusion, the current approach based on an inclusive FR assumed identical for all the
 740 production categories is not correct because FR is indeed different for VBF-tagged categories.
 741 Nevertheless, the final impact on the analysis is found to be not significant due to the kinematic
 742 discriminant used in the fit and the fact that Z+X yields are rather insignificant, so that the
 743 current strategy is kept for this analysis and more effort to have a category specific Z+X estimate
 744 in the future Run 3 analysis will be invested.

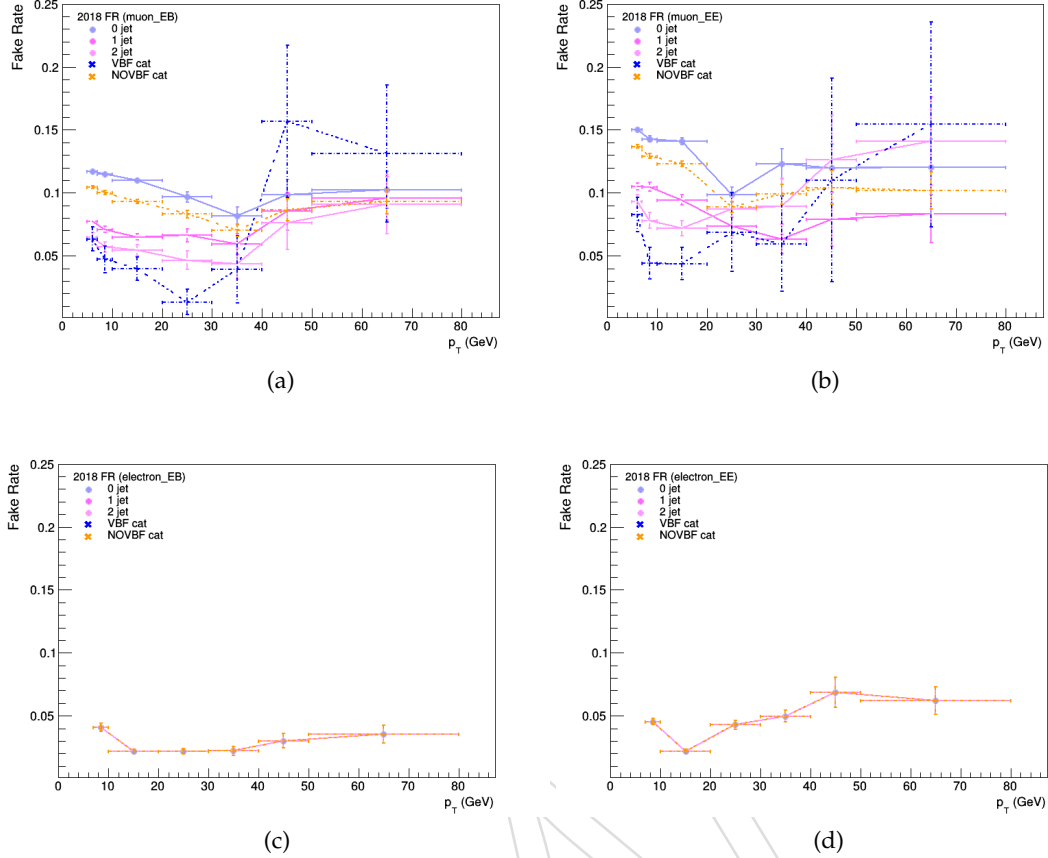


Figure 44: FR curves in the 0/1/2/VBF-tagged and non VBF-tagged categories for muons (top) and electrons (bottom) in the barrel (left) and endcap (right) region obtained using SS method.

Table 21: Comparison between combined ZX yields in the VBF-tagged categories using inclusive and dedicated FR.

CATEGORY	Inclusive FR				Dedicated FR			
	$4l$	4μ	$4e$	$2e2\mu$	$4l$	4μ	$4e$	$2e2\mu$
VBF_1j	1.047	0.391	0.147	0.509	0.663	0.185	0.113	0.365
VBF_2j	0.882	0.295	0.097	0.490	0.054	0.011	0.016	0.028
VBF_2j_mjj_350_700_2j	0.040	0.026	0.003	0.011	0.004	0.000	0.000	0.004
VBF_2j_mjj_GT700_2j	0.016	0.013	0.002	0.001	0.091	0.018	0.039	0.034
VBF_2j_mjj_GT350_3j	0.997	0.444	0.104	0.450	0.001	0.001	0.000	0.000
VBF_GT200_2J	0.021	0.019	0.001	0.001	0.015	0.001	0.001	0.014
Inclusive VBF	3.002	1.188	0.353	1.461	0.828	0.216	0.169	0.444

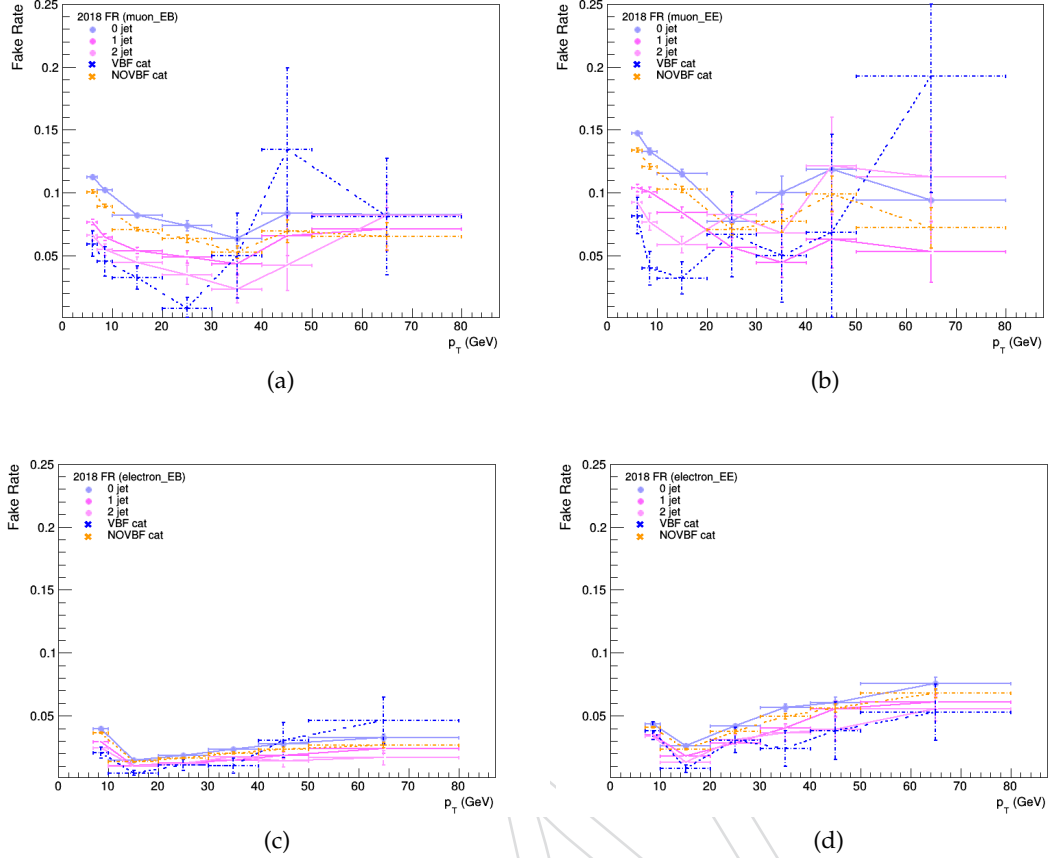


Figure 45: FR curves in the 0/1/2/VBF-tagged and non VBF-tagged categories for muons (top) and electrons (bottom) in the barrel (left) and endcap (right) region obtained using OS method.

Table 22: Comparison between the best-fit values and $\pm 1\sigma$ uncertainties for the expected and observed signal-strength modifiers, inflating ZX uncertainties in VBF categories by 100% and keeping nominal ZX uncertainties.

	Inflated ZX uncertainty		Nominal ZX uncertainty	
	Expected	Observed	Expected	Observed
$\mu_{t\bar{t}H,tH}$	$1.00^{+1.36}_{-0.78}$	$0.23^{+0.95}_{-0.23}$	$1.00^{+1.36}_{-0.78}$	$0.22^{+0.95}_{-0.22}$
μ_{WH}	$1.00^{+2.01}_{-1.00}$	$1.68^{+1.76}_{-1.44}$	$1.00^{+2.01}_{-1.00}$	$1.71^{+1.79}_{-1.71}$
μ_{ZH}	$1.00^{+8.33}_{-1.00}$	$0.00^{+5.24}_{-0.00}$	$1.00^{+8.33}_{-1.00}$	$0.00^{+5.44}_{-0.00}$
μ_{VBF}	$1.00^{+0.56}_{-0.46}$	$0.54^{+0.51}_{-0.41}$	$1.00^{+0.56}_{-0.46}$	$0.56^{+0.50}_{-0.41}$
$\mu_{ggH,b\bar{b}H}$	$1.00^{+0.16}_{-0.14}$	$1.02^{+0.15}_{-0.13}$	$1.00^{+0.16}_{-0.14}$	$1.03^{+0.15}_{-0.13}$

745 5.2.3 Shapes of the $m_{4\ell}$ distribution for the Reducible Background

746 In order to extract the shape of the $m_{4\ell}$ distribution for the reducible background used in the
 747 final analysis, shapes for each category and each final state are studied in the mass range [70,

748 300] GeV in both the SS and OS methods using 2016 dataset. Then the standard [105, 140] GeV
 749 window is used in the final analysis.

750 The study is focused on the SS method because of the better statistics available. A fit to Landau
 751 function is performed to provide the $m_{4\ell}$ shape in each category separately for the $4e$, 4μ , $2\mu 2e$
 752 and $2e 2\mu$ final state, as shown in Figure ???. Since not all the categories are populated enough,
 753 the minimum number of events needed to extract the shape for a single category has been
 754 evaluated; therefore, in the very low populated categories (less than fifty events selected in the
 755 mass window) shapes obtained from the inclusive distributions in each final state are used. On
 756 one hand, the results from the two methods are found to be more or less identical in the 4μ and
 757 $2e 2\mu$ final states; on the other hand, there is some difference in the $4e$ and $2\mu 2e$ distributions
 758 but mainly due to a difference in the yields (Figure 46). Taking into account the merged $2e 2\mu$
 759 and $2\mu 2e$ final state, a fit to Landau function is still performed to obtain the $m_{4\ell}$ shape: in fact,
 760 since the muon final state has a larger contribution, the addition of the $2\mu 2e$ component does
 761 not distort the single Landau shape.

762 Looking at the comparison between the $m_{4\ell}$ distribution for the $Z+X$ background obtained from
 763 the SS and OS methods in each category separately for all the final states, shape differences
 764 between the two methods are found to be not significant.

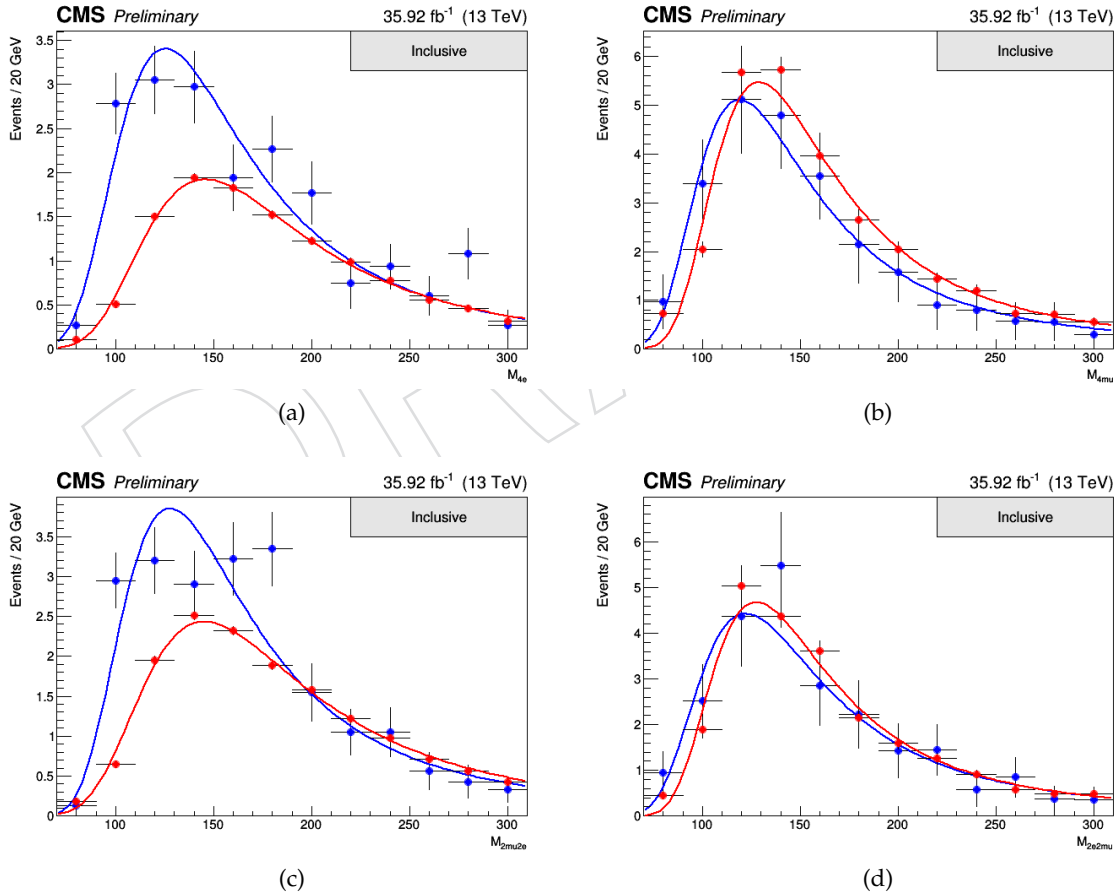


Figure 46: Comparison between the $m_{4\ell}$ distribution for the $Z+X$ reducible background obtained from the SS and OS methods (2016 dataset) in the inclusive category for each considered final state: $4e$ (a), 4μ (b), $2\mu 2e$ (c) and $2e 2\mu$ (d).

765 5.2.4 Uncertainties on Reducible Background estimation methods

766 One of the highest source of uncertainties in the analysis derives from the data-driven estimate
 767 of the reducible background. There are three different sources to be taken into account:

768 **Statistical uncertainty** The statistical uncertainty of the methods is driven by the limited
 769 size of the samples in the control regions where we measure ($Z + \ell$) and where we apply ($Z +$
 770 $\ell\ell$) the fake ratios and it is typically in the range of 1-10%.

771 **Systematic uncertainty due to fake rate variation** A systematic uncertainty given by the
 772 variation of the expected yield considering up and down variations in the fake rate measure-
 773 ment has to be taken into account.

774 **Systematic uncertainty due to background composition** The main source of the total
 775 uncertainty associated to the $Z+X$ estimate is due to the different composition of the reducible
 776 background processes ($DY, t\bar{t}, WZ, Z\gamma^{(*)}$) in the regions where we measure and where we
 777 apply the fake ratios. On one hand, the OS method corrects for the resulting bias via the “3P1F
 778 component” of its prediction. On the other had, the SS method corrects explicitly the electron
 779 fake rates by using the fraction of photon conversions, but no attempt is made to correct the
 780 muon fake rates. To evaluate the sensitivity of the estimate to background composition, the
 781 residual bias in the two methods can be estimated by measuring the fake ratios for individual
 782 background processes in the $Z + \ell$ region in simulated samples: the weighted average of these
 783 individual fake ratios is the fake rate that we measure in simulation. The exact composition of
 784 the background processes in the 2P+2F region where we plan to apply the fake ratios can be
 785 determined from simulation, thereby the individual fake ratios can be reweighted according to
 786 the 2P+2F composition. The difference between the reweighed fake ratio and the average value
 787 can be used as an estimate of the uncertainty on the measurement of the fake ratios. The effect
 788 of this systematic uncertainty is propagated to the final estimates, and it amounts to about 32%
 789 for $4e$, 33% for $2e2\mu$ and 35% for 4μ final state.

790 The final uncertainty associated to the combined $Z+X$ yield is given by the sum in quadrature
 791 of these three contributions considering the full mass range of the m_{4l} distribution in the SS
 792 method. Table 23 shows the $Z+X$ uncertainty for each final state in each year.

Channel	$4e$	4μ	$2e2\mu$
2016	41%	30%	35%
2017	38%	30%	33%
2018	37%	30%	33%

Table 23: Systematic uncertainty associated to the $Z+X$ estimate for each final state in all three years.

793 A shape uncertainty is not associated to the $Z+X$ estimate. In order to evaluate the uncertainty
 794 on the m_{4l} shape, we checked the difference between the shapes of predicted background dis-
 795 tributions for all three channels and between the shapes given by SS and OS methods. The
 796 uncertainty is estimated to be roughly in the range of 5% - 15%. Given that the difference of
 797 the shapes slowly varies with m_{4l} , it is taken as a constant versus m_{4l} and is absorbed into the
 798 much larger uncertainty on the predicted yield of background events.

799 **5.2.5 Combination**

800 Two methods for the reducible background estimation are presented with associated uncer-
 801 tainties in the previous sections. Table 24 shows the summary of the results given by the two
 802 methods combination for each year. The shape systematic uncertainty is absorbed in the statis-
 803 tical and systematic uncertainties on the estimated yields, and the total uncertainties are found
 804 to be of the order of 35–45%. Predictions of the two methods are combined assuming no
 805 correlation between the uncertainties (independent control regions, partially different sources
 806 systematics), and combined mean values are obtained by weighting the individual means ac-
 807 cording to the corresponding variances. For the final modelling of the background, the shape
 808 obtained from the SS method is taken in the mass range [105, 140] GeV: this is due to the
 809 better statistics available in the SS distributions; moreover, studies presented in the previous
 810 section 5.2.3 show no significant differences from the OS method. Figure 47 shows the shape
 811 obtained for one of the STXS categories as an example for each considered final state.

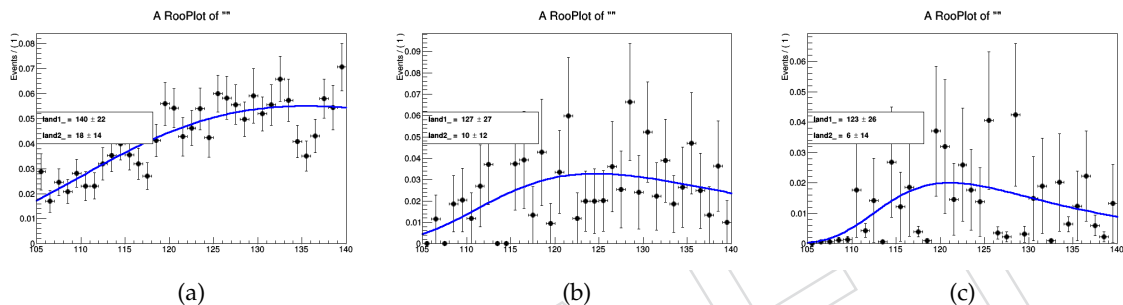


Figure 47: Shape of the $Z+X$ background events in the mass range [105, 140] GeV for the $ggH_0j_{10_200}$ category in the $4e$ final state (a), for the $ggH_1j_{60_120}$ category in the 4μ final state (b) and for the $VBF_2j_mjj_GT350_3j$ in the $2e2\mu$ final state (c).

812 If very low populated categories (less than fifty events selected in the mass window) are con-
 813 sidered, shapes obtained from the inclusive distributions in the given final state are used. This
 814 shape is finally scaled to the yield obtained from the combination of the SS and OS method re-
 815 sults. The yield uncertainty of 40% is able to cover all the discrepancies from the two methods,
 816 indeed shape uncertainty is not included.

817 **5.3 Rare Backgrounds**

818 The triboson backgrounds ZZZ , WZZ , and WWZ and $t\bar{t}Z$, $t\bar{t}WW$, and $t\bar{t}ZZ$ processes are
 819 also considered. These rare backgrounds are all estimated from simulation and are commonly
 820 referred to as the electroweak (EWK) backgrounds.

2016	4e	4μ	$2e2\mu$
Method OS	$20.2 \pm 6.2_{\text{tot.}}$	$27.0 \pm 8.6_{\text{tot.}}$	$47.7 \pm 10.5_{\text{tot.}}$
Method SS	$13.1 \pm 5.5_{\text{tot.}}$	$29.6 \pm 9.0_{\text{tot.}}$	$41.5 \pm 10.3_{\text{tot.}}$
Combined	16.1	28.2	44.4
2017	4e	4μ	$2e2\mu$
Method OS	$16.2 \pm 5.0_{\text{tot.}}$	$32.7 \pm 10.3_{\text{tot.}}$	$45.7 \pm 10.2_{\text{tot.}}$
Method SS	$10.9 \pm 4.1_{\text{tot.}}$	$33.4 \pm 10.3_{\text{tot.}}$	$40.8 \pm 9.7_{\text{tot.}}$
Combined	13.0	33.1	43.1
2018	4e	4μ	$2e2\mu$
Method OS	$25.4 \pm 7.7_{\text{tot.}}$	$50.1 \pm 15.5_{\text{tot.}}$	$67.7 \pm 14.8_{\text{tot.}}$
Method SS	$16.1 \pm 5.9_{\text{tot.}}$	$51.9 \pm 15.8_{\text{tot.}}$	$60.7 \pm 14.2_{\text{tot.}}$
Combined	19.4	50.7	63.9

Table 24: Summary of the results given by the two methods for the prediction of the contribution of reducible background processes in the signal region for all three years. The weighted mean value of the results of the two methods is taken as the final estimate of this contribution, while the uncertainty of the result covers the uncertainties of both methods. The table shows symmetric individual uncertainties for the two methods, while these are treated as asymmetric in the combination and statistical analysis. Results are given for an integrated luminosity of 35.9, 41.5 and 59.7 fb^{-1} in 2016, 2017 and 2018 data, respectively.

821 6 Signal Modelling

822 6.1 Signal modeling of the SM Higgs

823 6.1.1 Signal Corrections

824 For the dominant gluon fusion production mode for the signal, the p_T spectrum has been tuned
 825 using the “hfact” parameter of POWHEG to match closely the Higgs boson p_T spectrum in the
 826 full phase space as predicted by the HRES generator at $\sqrt{s} = 13$ TeV [56]. The agreement can
 827 be seen in Fig. 48. For other mass points, the “hfact” parameter is parametrized as a function
 828 of $m(H)$ as $h\text{fact} = 0.1 \cdot m(H) + 37.5$.

829 We use weights defined in bins of generated Higgs pT and number of generated jets to reweight
 830 our POWHEG signal sample to the NNLOPS one.

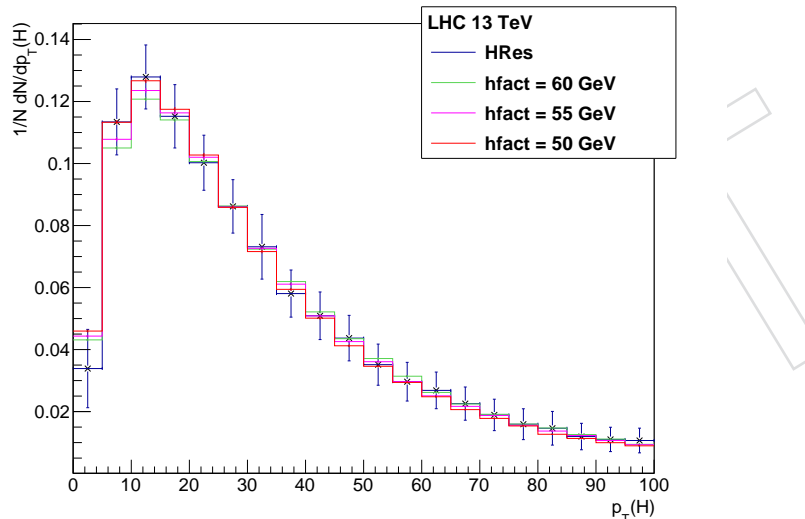


Figure 48: Comparison of POWHEG and HRES p_T spectrum at 13 TeV for different hfact.

831 6.1.2 Signal Normalization

832 The normalization of the Higgs boson signal in the peak region is directly taken from simulation.
 833 Using simulated samples for five m_H points (120, 124, 125, 126 and 130 GeV), polynomial
 834 fits of the expected signal yields in a [105, 140] GeV $m_{4\ell}$ window around the Higgs boson peak
 835 are performed.

836 **6.1.3 Signal Lineshape**

In this section we describe the PDF used to describe the signal shapes for different masses in different Event Categories as explained before. The resolution function model depends only on the leptons quality, while the exact shape depends on the lepton kinematics, and so depend also on the Higgs mass. A Double Crystal-Ball function $f_{dCB}(m_{4\ell} | m_H)$:

$$dCB(\xi) = N \cdot \begin{cases} A \cdot (B + |\xi|)^{-n_L}, & \text{for } \xi < \alpha_L \\ A \cdot (B + |\xi|)^{-n_R}, & \text{for } \xi > \alpha_R \\ \exp(-\xi^2/2), & \text{for } \alpha_L \leq \xi \leq \alpha_R \end{cases} \quad (6)$$

837 where $\xi = (m_{4\ell} - m_H - \Delta m_H)/\sigma_m$. This function has six independent parameters, and is in
 838 intended to capture the Gaussian core (σ_m) of the four-lepton mass resolution function, systematic
 839 mass shift Δm_H of the peak, and the left- and right-hand tail originating from leptons emitting
 840 bremsstrahlung in the tracker material, present for both electrons and muons, and from the non-Gaussian
 841 mis-measurements specific to interactions of electrons with the detector material (two parame-
 842 ters, n and α , for each side of the mean): The prominence of the left-,right-hand tail is defined
 843 by the power n_L, n_R , respectively. The parameters α_L, α_R define where the splicing of the tails and
 844 the core are made, in units of σ_m . Parameters A and B are not independent; they are defined
 845 by requiring the continuity of the function itself and its first derivatives. N is the normalizing
 846 constant.

847 The fitting strategy used to deal with this situation is to use the linear approximation of all the
 848 Double Crystal Ball parameters varying with m_H .

$$params = params_{CB0} + params_{CB1} \times (m_H - 125\text{GeV}) + params_{CB2} \times (m_H - 125\text{GeV})^2 \quad (7)$$

849 Simultaneous fits are performed using 5 mass samples to extract the $params_{CB0}$, $params_{CB1}$ and
 850 $params_{CB2}$. The initial value for the $params_{CB0}$ is obtained by fitting 125 GeV mass sample alone,
 and refitted in the simultaneous fits.

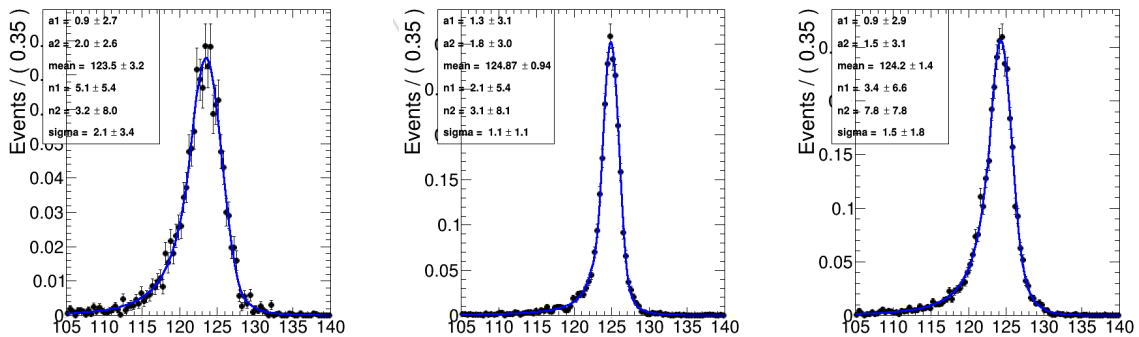


Figure 49: Probability density functions $f(m_{4l}|m_H)$ for signal with $m_H=125$ GeV at the re-
 construction level after the full lepton and event selections are applied. The distributions ob-
 tained from 13 TeV ggH MC samples are fitted with the model described in the text for 4μ
 (left), $4e$ (center) and $2e2\mu$ (right) events. The distribution show the events in the stage 1.1 bin
 ggH_0j_0..10.

852 7 Systematic uncertainties

853 The main experimental uncertainties which affect both signal and background are the uncer-
 854 tainty on the integrated luminosity (from to 2.3% to 2.6%, depending on the data taking period)
 855 and the uncertainty on the lepton identification and reconstruction efficiency (ranging from 1
 856 to 2.5% and from 11 to 15.5% on the overall yields, in the 4μ and $4e$ channels, respectively).
 857 Experimental uncertainties for the reducible background estimation, described in Section 5.1.1,
 858 vary between 6% to 32% from the variation of the fake rates. The mismatch in the composition
 859 of backgrounds between the samples where the fake rate is derived and where it is applied
 860 accounts for about 30%.

861 The uncertainty of the lepton energy scale is assessed by propagating down to the four-leptons
 862 invariant mass the uncertainty associated the lepton momentum corrections on each individual
 863 lepton. The uncertainty is treated as uncorrelated (all up or all down). The new four-leptons
 864 invariant mass obtained this way is then fitted with only the mean value floating. The differ-
 865 ence between the new mean value and the default one gives an estimation of the impact of the
 866 lepton energy scale. The values are reported in the Table 25, together with the estimation of the
 867 impact of lepton momentum resolution, following a similar procedure.

Table 25: Difference (in %) between the nominal mean and width of the four-leptons Higgs mass distribution and those where the lepton momentum scale and resolution uncertainties have been propagated.

	4e	4μ	$2e2\mu$
Scale Difference (%)	0.087	0.049	0.069
Resolution Difference (%)	17	12	17

868 The results obtained this way suggest that the uncertainties from 2016 (20% on the resolution,
 869 0.3% for the $4e$ channel for scale) are still valid.

870 Theoretical uncertainties which affect both the signal and background estimation include un-
 871 certainties from the renormalization and factorization scale and choice of PDF set. The uncer-
 872 tainty from the renormalization and factorization scale is determined by varying these scales
 873 between 0.5 and 2 times their nominal value while keeping their ratio between 0.5 and 2. In the
 874 case of ggF production mode, the QCD scale uncertainty is broken down to 9 different sources.
 875 The renormalization and factorization scale affect the overall cross section, the migration of
 876 the stage1.1 bins in different Higgs pT and number of jets, top loop effects are treated as inde-
 877 pendent uncertainties, and correlated among different stage 1.1 bins. The numbers are shown
 878 in Fig ???. The uncertainty from the PDF set is determined by taking the root mean square of
 879 the variation when using different replicas of the default NNPDF set. PDF uncertainty arises
 880 from uncertainty is also taken into account. On the background, an additional uncertainty of
 881 10% on the K factor used for the $gg \rightarrow ZZ$ prediction is applied as described in Section 5.1. A
 882 systematic uncertainty of 2% on the branching ratio of $H \rightarrow ZZ \rightarrow 4\ell$ only affects the signal
 883 yield. In the case of event categorization, experimental and theoretical uncertainties which ac-
 884 count for possible migration of signal and background events between categories are included.
 885 The main sources of uncertainty on the event categorization include the QCD scale, PDF set,
 886 and the modeling of hadronization and the underlying event. These uncertainties amount to
 887 between 4–20% for the signal and 3–20% for the background depending on the category. The
 888 lower range corresponds to the VBF and VH processes and the upper range corresponds to the
 889 $gg \rightarrow H$ process yield in the VBF-2jet-tagged category. Additional uncertainties come from the
 890 imprecise knowledge of the jet energy scale (from 2% for the $gg \rightarrow H$ yield in the untagged
 891 category to 22% for $gg \rightarrow H$ yield in the VBF-2jet-tagged category) and b-tagging efficiency

892 and mistag rate (up to 10% in the $t\bar{t}H$ -tagged category). In the cross section measurement, the
 893 signal cross section uncertainties arise from theoretical sources are removed.

Table 26: Summary of the experimental systematic uncertainties in the $H \rightarrow 4\ell$ measurements of 2016, 2017 and 2018 data.

Summary of relative systematic uncertainties			
Common experimental uncertainties			
	2016	2017	2018
Luminosity	2.6 %	2.3 %	2.5 %
Lepton identification/reconstruction efficiencies	1.2 – 15.5 %	1.1 – 12 %	0.7 – 11 %
Background related uncertainties			
Reducible background ($Z+X$)	31 – 42 %	31 – 38 %	31 – 37 %
Signal related uncertainties			
Lepton energy scale	0.04 – 0.3 %	0 %	0 %
Lepton energy resolution	20 %	20 %	20 %

Table 27: Summary of the theory systematic uncertainties in the $H \rightarrow 4\ell$ measurements for the inclusive analysis

Summary of inclusive theory uncertainties	
QCD scale (gg)	± 3.9 %
PDF set (gg)	± 3.2 %
Bkg K factor (gg)	± 10 %
QCD scale (VBF)	+0.4/-0.3 %
PDF set (VBF)	± 2.1 %
QCD scale (WH)	+0.5/-0.7 %
PDF set (WH)	± 1.9 %
QCD scale (ZH)	+3.8/-3.1 %
PDF set (ZH)	± 1.6 %
QCD scale ($t\bar{t}H$)	+5.8/-9.2 %
PDF set ($t\bar{t}H$)	± 3.6 %
BR($H \rightarrow ZZ \rightarrow 4\ell$)	2 %
QCD scale ($q\bar{q} \rightarrow ZZ$)	+3.2/-4.2 %
PDF set ($q\bar{q} \rightarrow ZZ$)	+3.1/-3.4 %
Electroweak corrections ($q\bar{q} \rightarrow ZZ$)	± 0.1 %

894 7.1 Systematic uncertainties treatment when combining the data sets

895 In this Section we describe how different systematic uncertainties are treated when combining
 896 the data sets. The theoretical uncertainties are correlated. All the experimental systematics are
 897 treated independently.

8 Yields and distributions

In this section we summarize the status of the analysis after selection, showing the inputs to the final results, namely the event yields and errors in the full signal region and in a restricted $m_{4\ell}$ range, and the distributions of the main kinematic variables in data and MC.

8.1 Signal Region Yields

The number of candidates observed in data and the expected yields for the backgrounds and Higgs boson signal after the full event selection are reported in Table 28 for the full range of $m_{4\ell}$. Table ?? shows the expected and observed yields for each of the 22 event categories, for a $118 < m_{4\ell} < 130$ GeV mass window around the Higgs boson peak.

Table 28: The number of expected background and signal events and number observed candidates after full analysis selection, for each final state, for the full mass range $m_{4\ell} > 70$ GeV, for an integrated luminosity of 137 fb^{-1} . Signal and ZZ backgrounds are estimated from Monte Carlo simulation, Z+X is estimated from data.

Channel	4μ	$4e$	$2e2\mu$	$4l$
qqZZ	1414.85	748.64	1835.05	3998.54
ggZZ	268.48	163.45	399.78	831.70
ZX	112.84	48.62	151.71	313.18
EW bkg	15.13	12.73	27.83	55.69
Sum of backgrounds	1811.30	973.45	2414.36	5199.11
Signal ($m_H = 125$ GeV)	95.27	46.01	118.53	259.82
Total expected	1906.57	1019.46	2532.90	5458.93
Data	1970	1032	2646	5648

8.2 Signal Region Distributions

The reconstructed four-lepton invariant mass distribution is shown in Figure 50 for the full dataset, and compared to expectations from the SM backgrounds, first for the full mass range, and then zooming on the low-mass range and high-mass range. In Figure 51, the same distributions are shown split by final state ($4e$, 4μ , and $2e2\mu$), for the two same mass ranges. In Figure ??, they are split by event category, for the low-mass range. The SM background distributions are obtained combining the rate normalization from data-driven methods and knowledge on shapes taken from the MC samples.

The reconstructed dilepton invariant masses selected as Z_1 and Z_2 are shown in Figures ?? together with their correlation, both full range of $m_{4\ell}$ and focusing on a $118 < m_{4\ell} < 130$ GeV mass window around the Higgs boson peak. Similarly, the decay discriminant $\mathcal{D}_{\text{bkg}}^{\text{kin}}$, $\mathcal{D}_{\text{bkg}}^{\text{VBF+dec}}$ and $\mathcal{D}_{\text{bkg}}^{\text{VH+dec}}$ are shown in Fig. ??, ?? and ?? in this window. The four production mechanism discriminant $\mathcal{D}_{2\text{jet}}$, $\mathcal{D}_{1\text{jet}}$, \mathcal{D}_{WH} , and \mathcal{D}_{ZH} are shown in Fig. ?? in the $118 < m_{4\ell} < 130$ GeV mass window, for events with at least two selected jets (except $\mathcal{D}_{1\text{jet}}$ which is for events with exactly one selected jet). Their correlations with $m_{4\ell}$ are shown in Fig. ??.

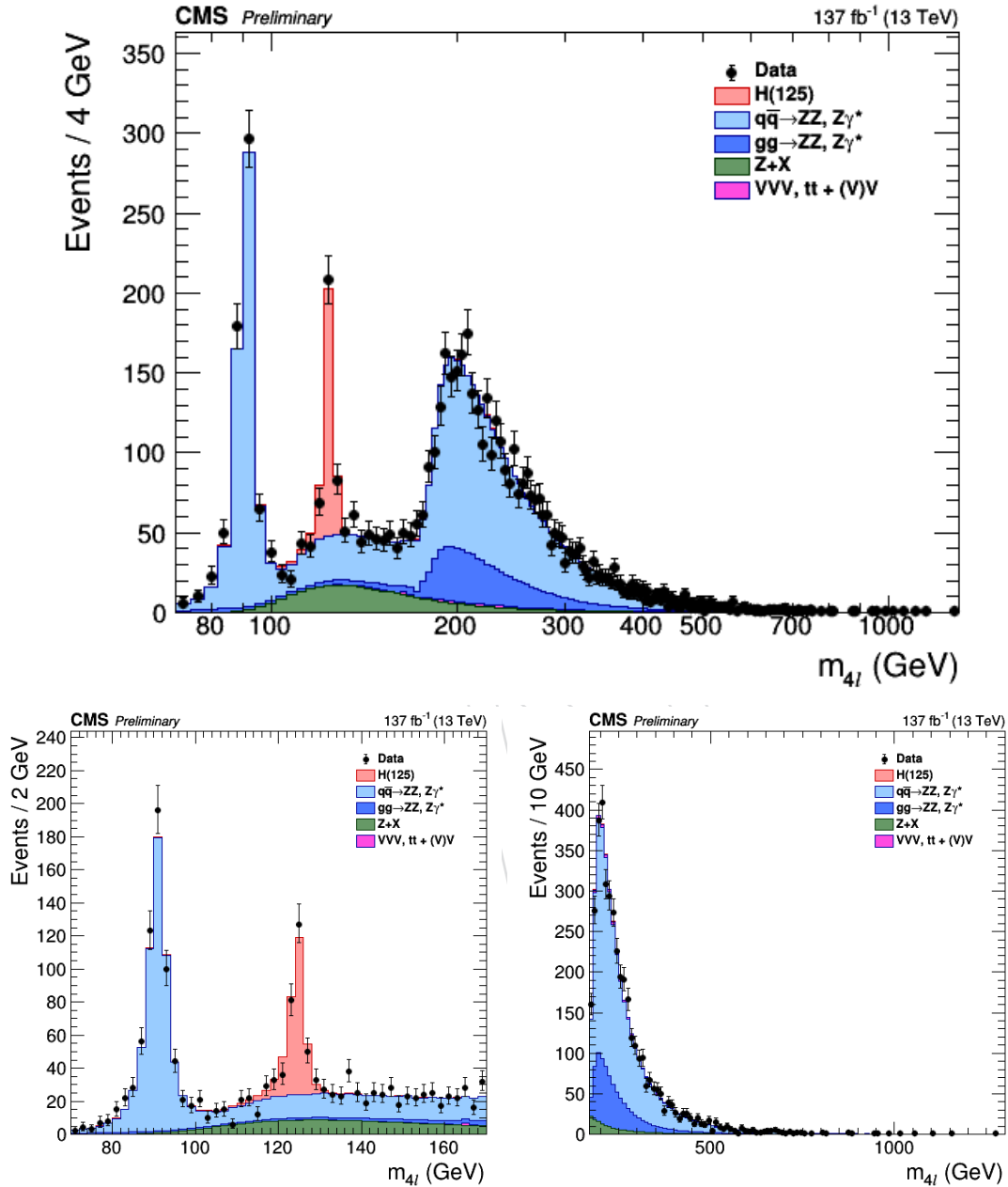


Figure 50: Distribution of the four-lepton reconstructed invariant mass m_{4l} in the full mass range (top) and the low-mass range (bottom left) and high-mass range (bottom right). Points with error bars represent the data and stacked histograms represent expected distributions. The 125 GeV Higgs boson signal and the ZZ backgrounds are normalized to the SM expectation, the $Z + X$ background to the estimation from data.

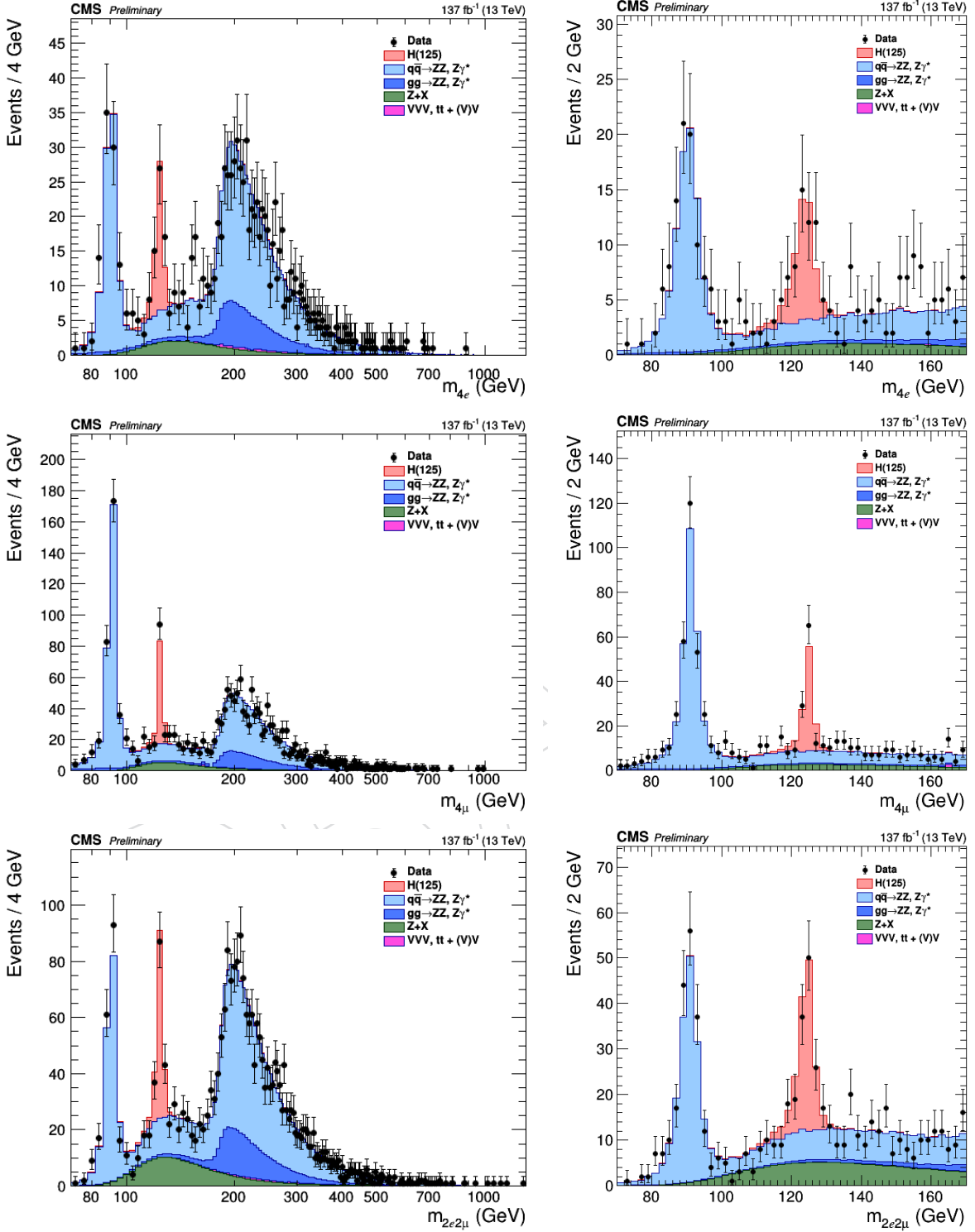
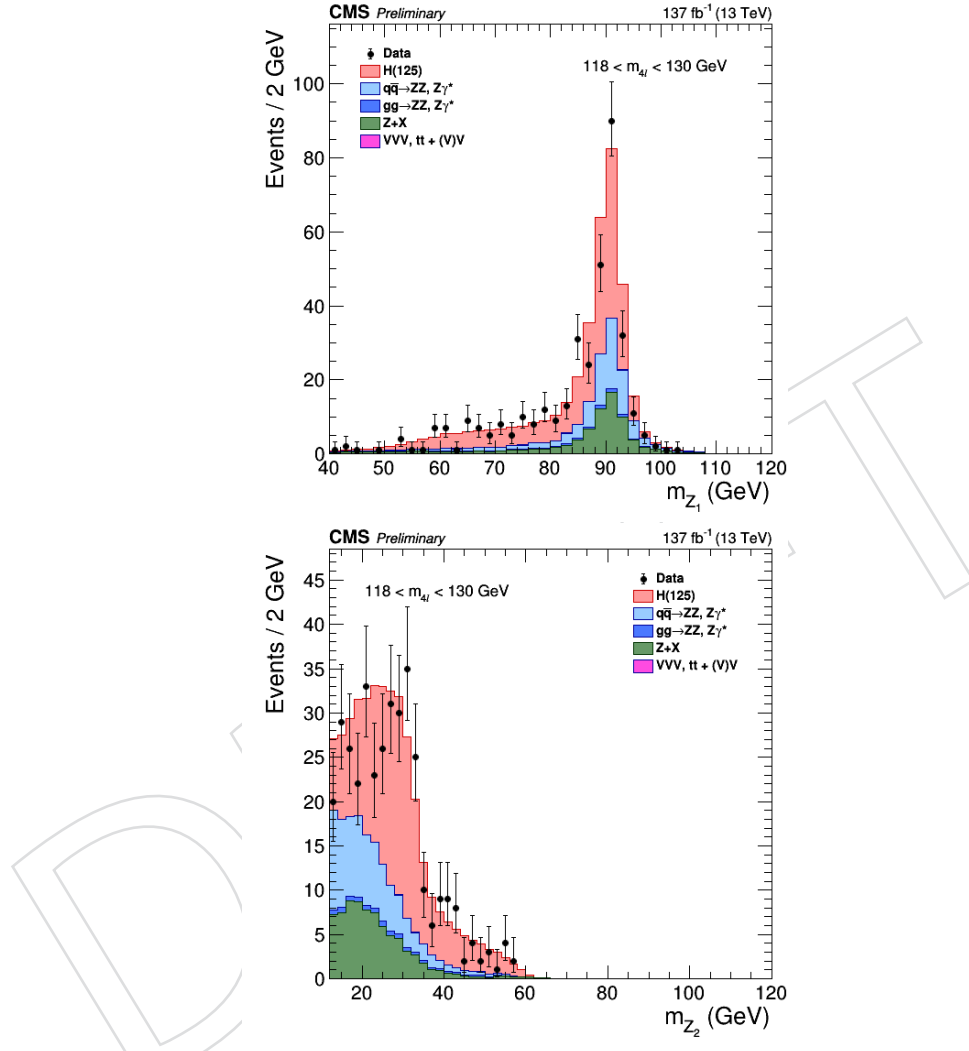


Figure 51: Distribution of the four-lepton reconstructed mass in several sub-channels: $4e$ (top), 4μ (middle), $2e2\mu$ for the low-mass range (bottom) for the full mass range (left) and the low-mass range (right).



Distribution of the Z_1 (left) and Z_2 (right) reconstructed invariant masses for the full mass range (left) and the low mass ($118 < m_{4\ell} < 130$ GeV) range (right). The stacked histograms and the gray scale represent expected distributions, and points represent the data. The 125 GeV Higgs boson signal and the ZZ backgrounds are normalized to the SM expectation, the $Z+X$ background to the estimation from data.

923 **9 Results**

924 In this section, we describe the methods used for the estimation of the significance of the ex-
925 cess of events above the SM backgrounds observed in the low-mass region, and of the signal
926 strength, i.e. its cross section normalized to the one expected for a SM Higgs.

927 To exploit all the properties of the resonance under study or search, a multi-dimensional fit is
928 implemented. For each of the categories defined in Section ??, the variable used in the maxi-
929 mum likelihood fit is:

- 930 1. The four-lepton mass without kinematic refitting $m_{4\ell}$,

DRAFT

9.1 Differential Cross Sections and EFT interpretations

932 **FIXME:** Results to be updated with final processing

933 9.1.1 Fiducial Volume Definition

934 The fiducial volume is defined to match closely the reconstruction level selection and is very
 935 similar to the definition used in Refs. [18]. With respect to the Run 1 analysis, the leptons are
 936 defined as “dressed” leptons rather than Born level leptons. Leptons are dressed by adding the
 937 four-momenta of leptons within $\Delta R < 0.3$ to the bare leptons. The fiducial lepton isolation cri-
 938 teria is also updated to match the Run 2 reconstruction level isolation. Leptons are considered
 939 isolated at generator level if the sum p_T of particles within a cone $\Delta R < 0.3$ is less than 0.35. The
 940 fiducial volume definition can be seen in Table 29. The fiducial volume acceptance for various
 941 SM production modes can be seen in Table 32.

Table 29: Summary of requirements and selections used in the definition of the fiducial phase space for the $H \rightarrow 4\ell$ cross section measurements.

Requirements for the $H \rightarrow 4\ell$ fiducial phase space	
Lepton kinematics and isolation	
leading lepton p_T	$p_T > 20$ GeV
next-to-leading lepton p_T	$p_T > 10$ GeV
additional electrons (muons) p_T	$p_T > 7(5)$ GeV
pseudorapidity of electrons (muons)	$ \eta < 2.5(2.4)$
p_T sum of all stable particles within $\Delta R < 0.3$ from lepton	less than $0.35 \cdot p_T$
Event topology	
existence of at least two SFOS lepton pairs, where leptons satisfy criteria above	
inv. mass of the Z_1 candidate	$40 \text{ GeV} < m(Z_1) < 120 \text{ GeV}$
inv. mass of the Z_2 candidate	$12 \text{ GeV} < m(Z_2) < 120 \text{ GeV}$
distance between selected four leptons	$\Delta R(\ell_i \ell_j) > 0.02$ for any $i \neq j$
inv. mass of any opposite sign lepton pair	$m(\ell^+ \ell^-) > 4 \text{ GeV}$
inv. mass of the selected four leptons	$105 \text{ GeV} < m_{4\ell} < 140 \text{ GeV}$
the selected four leptons must originate from the $H \rightarrow 4\ell$ decay	

942 9.1.2 Measurement Strategy

943 We measure the integrated and differential fiducial cross section for $pp \rightarrow H \rightarrow 4\ell$ by performing
 944 a maximum likelihood fit of the signal and background parameterisations to the observed
 945 4ℓ mass distribution, $N_{\text{obs}}(m_{4\ell})$, and the fiducial cross section (σ_{fid}) is directly extracted from
 946 the fit. The systematic uncertainties are included in the form of nuisance parameters and are
 947 effectively integrated out in the fit procedure. The results are obtained using an asymptotic
 948 approach [57] with a test statistic based on the profile likelihood ratio [58]. This procedure
 949 for the unfolding of the detector effects from the observed distributions is the same as in
 950 Refs. [18] and [59]. In the case of the differential cross section measurements, the finite effi-
 951 ciencies and resolution effects are encoded in a detector response matrix which describes how
 952 events migrate from a given observable bin at the fiducial level to a given bin at the recon-
 953 struction level. This matrix is diagonally dominant, with sizeable off-diagonal elements for
 954 observables involving jets.

955 Following the models for signal and background contributions described above, the number of
 956 expected events in each final state f and in each bin i of a considered observable is expressed as

957 a function of $m_{4\ell}$ given by:

$$\begin{aligned} N_{\text{obs}}^{\text{f},i}(m_{4\ell}) &= N_{\text{fid}}^{\text{f},i}(m_{4\ell}) + N_{\text{nonfid}}^{\text{f},i}(m_{4\ell}) + N_{\text{nonres}}^{\text{f},i}(m_{4\ell}) + N_{\text{bkg}}^{\text{f},i}(m_{4\ell}) \\ &= \epsilon_{i,j}^{\text{f}} \cdot \left(1 + f_{\text{nonfid}}^{\text{f},i}\right) \cdot \sigma_{\text{fid}}^{\text{f},j} \cdot \mathcal{L} \cdot \mathcal{P}_{\text{res}}(m_{4\ell}) \\ &\quad + N_{\text{nonres}}^{\text{f},i} \cdot \mathcal{P}_{\text{nonres}}(m_{4\ell}) + N_{\text{bkg}}^{\text{f},i} \cdot \mathcal{P}_{\text{bkg}}(m_{4\ell}), \end{aligned} \quad (8)$$

958 The parameter $\sigma_{\text{fid}}^{\text{f},j}$ is the signal cross section in bin j of the fiducial phase space, and it is the
959 parameter extracted from the measurement.

960 The shape of the resonant signal contribution, $\mathcal{P}_{\text{res}}(m_{4\ell})$, is described by a double-sided Crystal
961 Ball function as described in Section 6.1.3 whose normalisation is proportional to the fiducial
962 cross section. The shape of the non-resonant signal contribution, $\mathcal{P}_{\text{nonres}}(m_{4\ell})$, which arises
963 from WH, ZH, and $t\bar{t}H$ production where one of the leptons from the Higgs boson decay is
964 lost or not selected, is empirically modelled by a Landau distribution whose shape parameters
965 are constrained in the fit to be within a range determined from simulation. This contribution
966 is treated as a background and hereafter we will refer to this contribution as the “non-resonant
967 signal” contribution.

968 The $\epsilon_{i,j}^{\text{f}}$ represents the detector response matrix that maps the number of expected events in
969 a given observable bin j at the fiducial level to the number of expected events in the bin i at
970 the reconstruction level. The f_{nonfid}^i fraction describes the ratio of the non-fiducial and fiducial
971 signal contribution in bin i at the reconstruction level. The efficiency is measured using signal
972 simulation samples and corrected for residual differences between data and simulation. In
973 the case of the integrated fiducial cross section measurement the efficiencies reduce to a single
974 values.

975 An additional resonant contribution arises from events which are reconstructed but which do
976 not originate from the fiducial phase space. These events are due to detector effects which
977 cause differences between the quantities used for the fiducial phase space definition and the
978 analogous quantities at the reconstruction level. This contribution is treated as background
979 and is referred to as the “non-fiducial signal” contribution. The shape of these events is verified
980 using simulation to be identical to the shape of the fiducial signal and its normalisation is fixed
981 to be a fraction of the fiducial signal component. The value of this fraction, which we denote
982 by f_{nonfid} , which has been determined from simulation for each of the studied signal models.

983 The variation between different models of the factor in the final column of Table 32, $(1 +$
984 $f_{\text{nonfid}})\epsilon$, is directly related to the model dependence of the measurement. The model de-
985 pendence is defined as the variation of the factor $(1 + f_{\text{nonfid}})\epsilon$ when the relative fraction of
986 each the production modes are varied within their experimental constraints. An increase in
987 model dependence compared to Run 1 is observed when using the ZZ candidate selection at
988 reconstruction level where the the candidate with the best $D_{\text{bkg}}^{\text{kin}}$ discriminant value is chosen.
989 Therefore the fiducial cross section measurement is performed with a different event selection
990 algorithm than the other measurements, namely that the ZZ candidate selection is made using
991 the same algorithm as in Run 1.

992 Examples of the efficiency matrices for gluon fusion and VBF production can be seen in Fig. 52.
993 The matrices for the p_{TH} and $N(\text{jets})$ observables are shown.

Table 30: Summary of different Standard Model signal models. The MC samples are from 2016 production.

Signal process	\mathcal{A}_{fid}	ϵ	f_{nonfid}	$(1 + f_{\text{nonfid}})\epsilon$
Individual Higgs boson production modes				
gg \rightarrow H (POWHEG)	0.398	0.592 ± 0.001	0.049 ± 0.001	0.621 ± 0.001
VBF (POWHEG)	0.445	0.601 ± 0.002	0.038 ± 0.001	0.624 ± 0.002
WH (POWHEG+MINLO)	0.314	0.577 ± 0.002	0.068 ± 0.001	0.616 ± 0.002
ZH (POWHEG+MINLO)	0.342	0.592 ± 0.003	0.071 ± 0.002	0.634 ± 0.003
ttH (POWHEG)	0.311	0.572 ± 0.003	0.136 ± 0.003	0.650 ± 0.004

Table 31: Summary of different Standard Model signal models. The MC samples are from 2017 production.

Signal process	\mathcal{A}_{fid}	ϵ	f_{nonfid}	$(1 + f_{\text{nonfid}})\epsilon$
Individual Higgs boson production modes				
gg \rightarrow H (POWHEG)	0.404 ± 0.001	0.593 ± 0.001	0.054 ± 0.001	0.625 ± 0.001
VBF (POWHEG)	0.443 ± 0.001	0.605 ± 0.002	0.045 ± 0.001	0.632 ± 0.002
WH (POWHEG+MINLO)	0.329 ± 0.001	0.589 ± 0.002	0.080 ± 0.001	0.637 ± 0.002
ZH (POWHEG+MINLO)	0.341 ± 0.002	0.593 ± 0.003	0.083 ± 0.002	0.643 ± 0.004
ttH (POWHEG)	0.316 ± 0.002	0.597 ± 0.003	0.172 ± 0.004	0.700 ± 0.004

Table 32: Summary of different Standard Model signal models. The MC samples are from 2018 production. **FIXME: Scale factors not yet applied**

Signal process	\mathcal{A}_{fid}	ϵ	f_{nonfid}	$(1 + f_{\text{nonfid}})\epsilon$
Individual Higgs boson production modes				
gg \rightarrow H (POWHEG)	0.403 ± 0.001	0.630 ± 0.001	0.055 ± 0.001	0.664 ± 0.001
VBF (POWHEG)	0.443 ± 0.001	0.645 ± 0.002	0.043 ± 0.001	0.673 ± 0.002
WH (POWHEG+MINLO)	0.330 ± 0.001	0.632 ± 0.002	0.075 ± 0.001	0.679 ± 0.002
ZH (POWHEG+MINLO)	0.338 ± 0.002	0.638 ± 0.003	0.086 ± 0.003	0.693 ± 0.004
ttH (POWHEG)	0.314 ± 0.002	0.620 ± 0.003	0.184 ± 0.004	0.733 ± 0.004

9.1.3 Measurement results

- The result of the simultaneous fit to the $m_{4\ell}$ spectrum is shown for each final state in Fig. 53.
The fiducial cross section using this definition is measured to be:

$$2.85^{+0.24}_{-0.23}(\text{stat.})^{+0.15}_{-0.14}(\text{sys.}) \text{ fb} \quad (9)$$

- This can be compared to the SM expectation of $\sigma_{\text{fid.}}^{\text{SM}} = 2.72 \pm 0.14 \text{ fb}$.
The expected differential cross section results can be seen in Fig. 57.

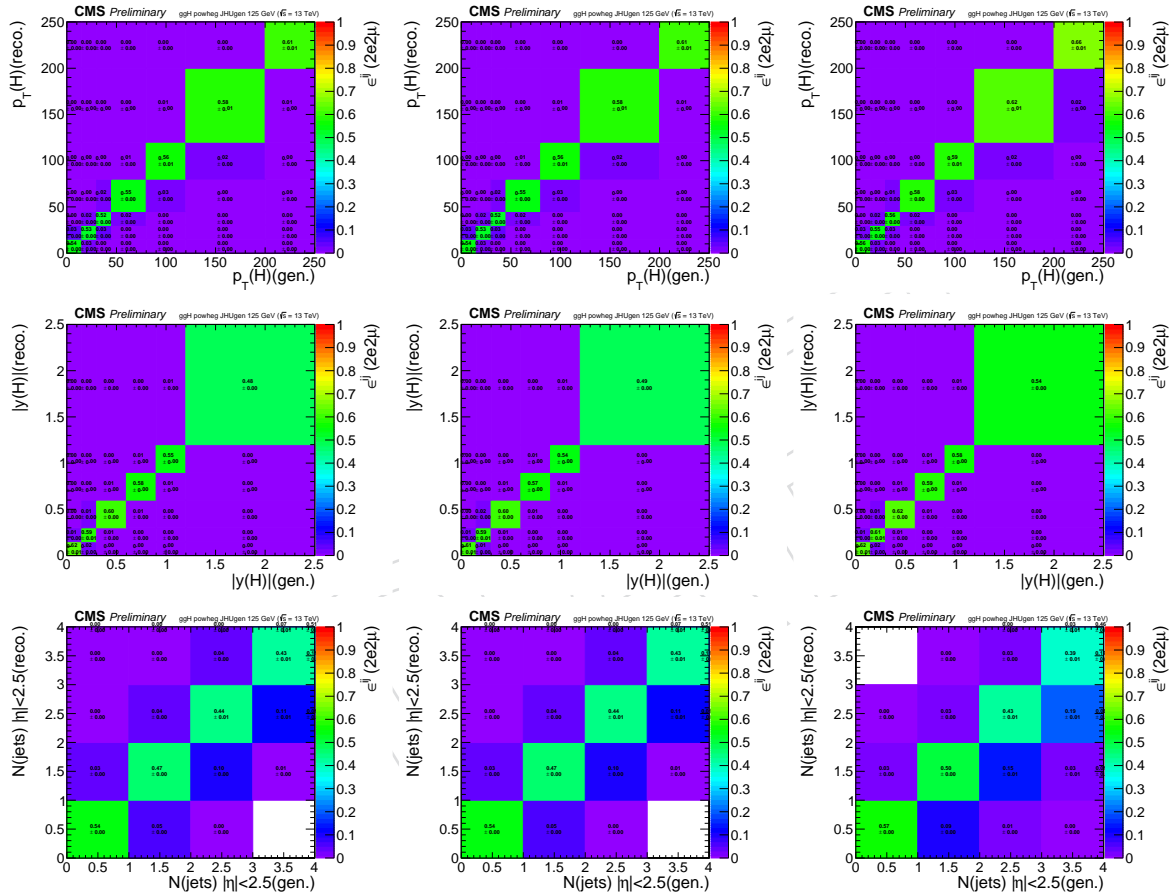


Figure 52: Efficiency matrices for the p_{TH} (top) and yH (middle) and $N(jets)$ (bottom) observables for gluon fusion production modes in the $2e2\mu$ final state in 2016 (left) 2017 (middle) and 2018 (right).

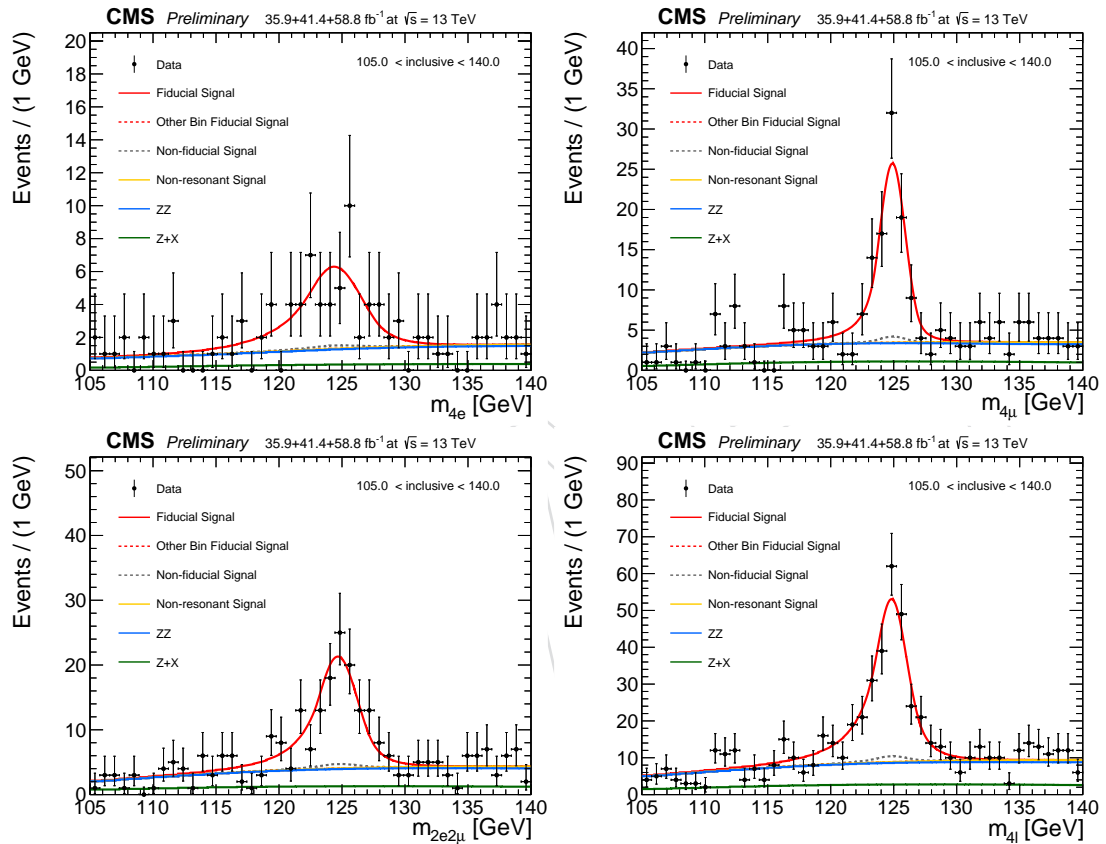


Figure 53: Result of simultaneous fit for the integrated fiducial cross section measurement in each final state. The results are shown for 2018 only.

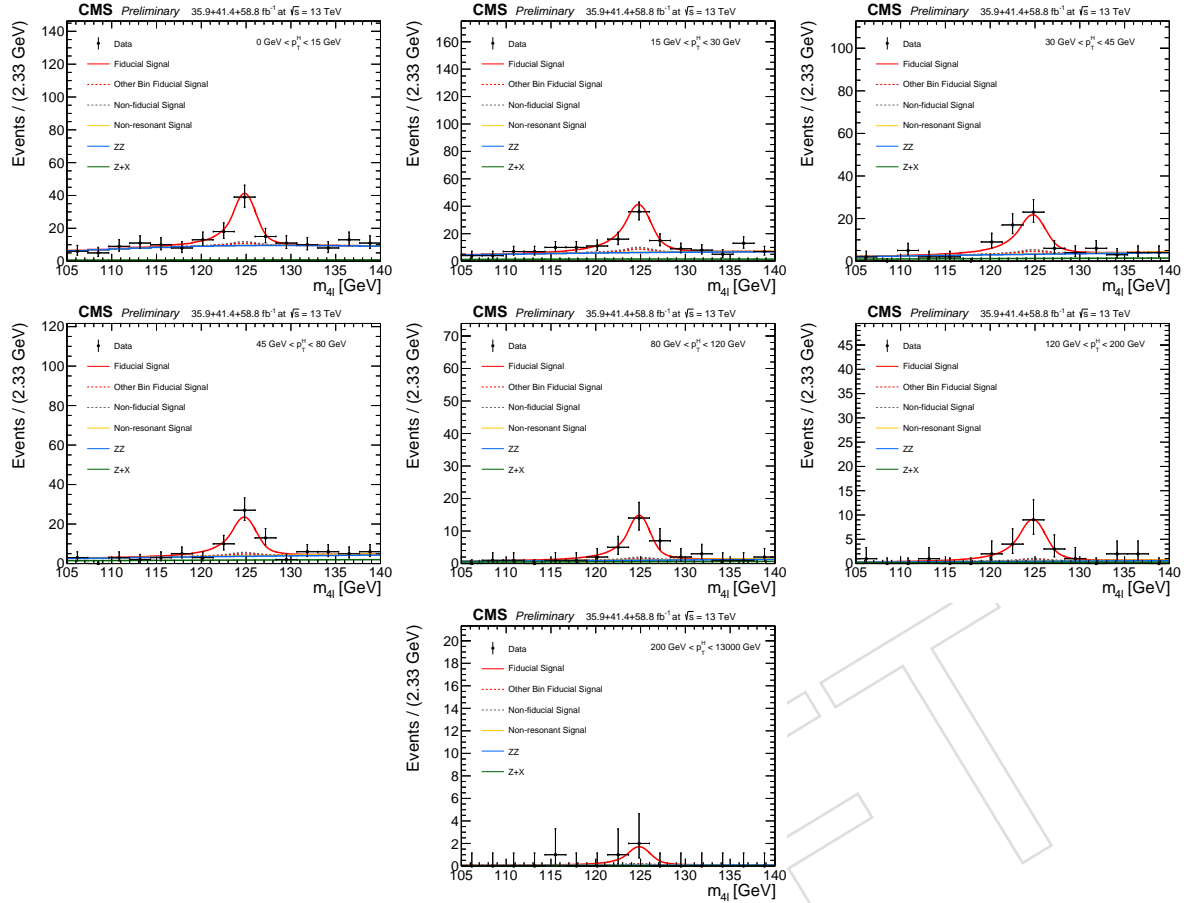


Figure 54: Result of simultaneous fit for the differential fiducial cross section measurement for $p_T(H)$ in each differential bin. The combined 4ℓ final state is shown. The results are shown for 2018 only.

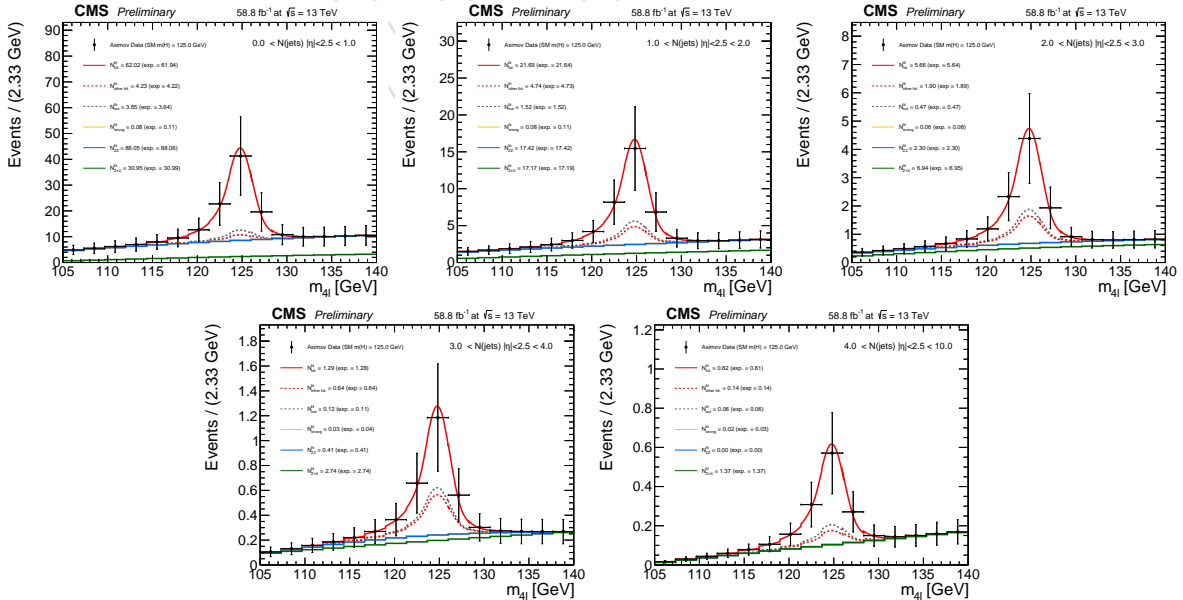


Figure 55: Result of simultaneous fit for the differential fiducial cross section measurement for $N(\text{jets})$ in each differential bin. The combined 4ℓ final state is shown. The results are shown for 2018 only.

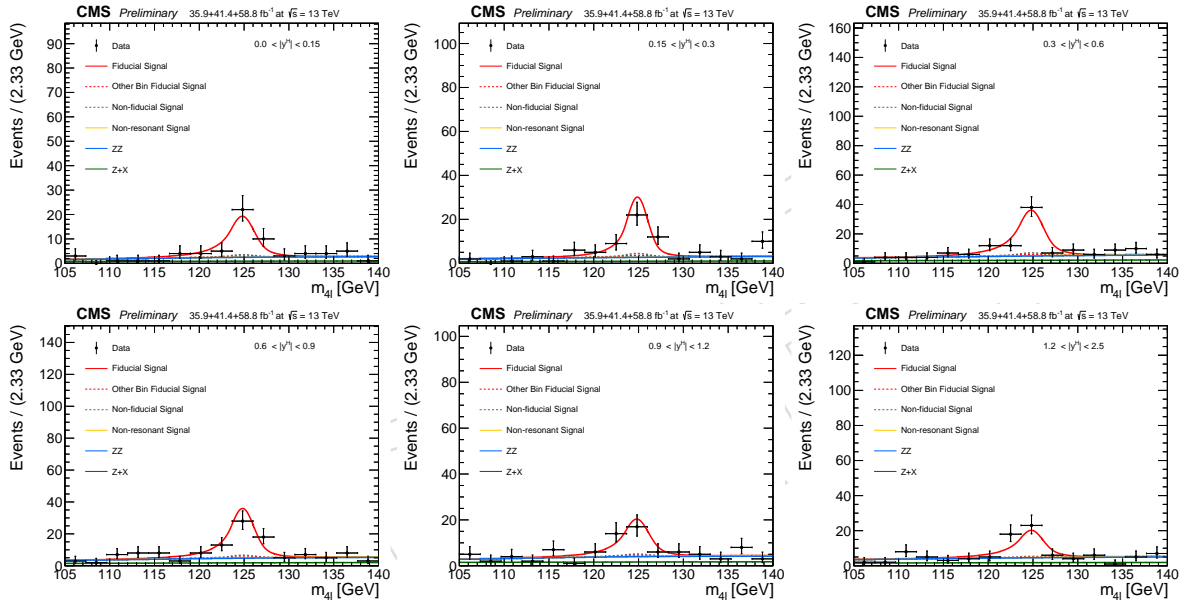


Figure 56: Result of simultaneous fit for the differential fiducial cross section measurement for $y(H)$ in each differential bin. The combined 4ℓ final state is shown. The results are shown for 2018 only.

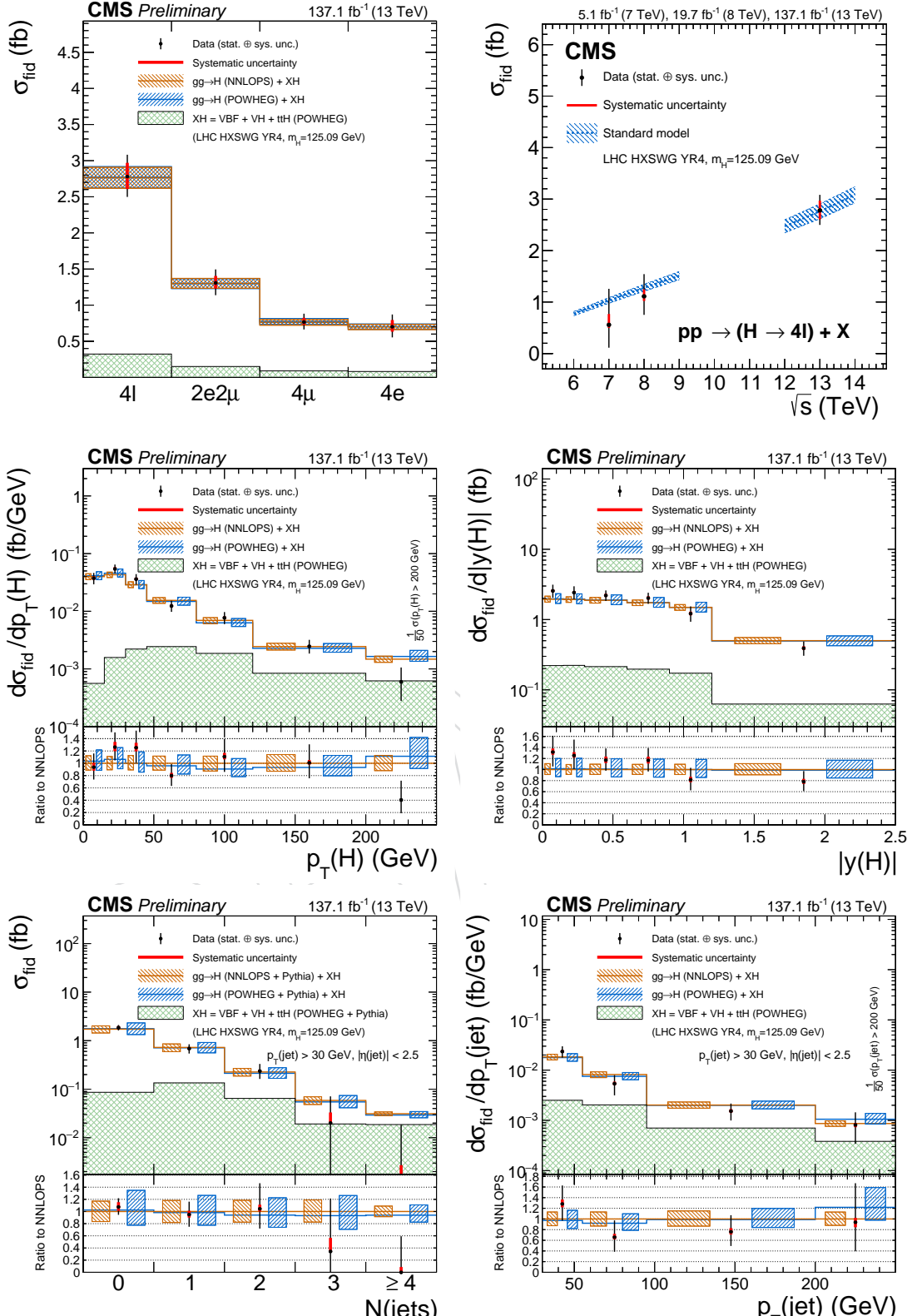


Figure 57: The measured inclusive fiducial cross section in different final states (top left). The measured fiducial cross section as a function of \sqrt{s} (top right). The acceptance is calculated using POWHEG at $\sqrt{s}=13$ TeV and HRES [54?] at $\sqrt{s}=7$ and 8 TeV and the total gluon fusion cross section and uncertainty are taken from Ref. [?]. The fiducial volume for $\sqrt{s}=6-9$ TeV uses the lepton isolation definition from Ref. [18], while for $\sqrt{s}=12-14$ TeV the definition described in the text is used. The results of the differential cross section measurement for $p_T(H)$ (middle left), $|y(H)|$ (middle right) and $N(\text{jets})$ (bottom left), p_T of the leading jet (bottom right). The acceptance and theoretical uncertainties in the differential bins are calculated using POWHEG. The sub-dominant component of the signal (VBF + VH + tH) is denoted as XH.

999 References

- 1000 [1] CMS Collaboration, "Observation of a new boson at a mass of 125 GeV with the CMS
1001 experiment at the LHC", *Phys. Lett. B* **716** (2012) 30,
1002 doi:10.1016/j.physletb.2012.08.021, arXiv:1207.7235.
- 1003 [2] ATLAS Collaboration, "Observation of a new particle in the search for the Standard
1004 Model Higgs boson with the ATLAS detector at the LHC", *Phys. Lett. B* **716** (2012) 1,
1005 doi:10.1016/j.physletb.2012.08.020, arXiv:1207.7214.
- 1006 [3] F. Englert and R. Brout, "Broken Symmetry and the Mass of Gauge Vector Mesons",
1007 *Phys. Rev. Lett.* **13** (1964) 321, doi:10.1103/PhysRevLett.13.321.
- 1008 [4] P. W. Higgs, "Broken symmetries, massless particles and gauge fields", *Phys. Lett.* **12**
1009 (1964) 132, doi:10.1016/0031-9163(64)91136-9.
- 1010 [5] P. W. Higgs, "Broken Symmetries and the Masses of Gauge Bosons", *Phys. Rev. Lett.* **13**
1011 (1964) 508, doi:10.1103/PhysRevLett.13.508.
- 1012 [6] G. Guralnik, C. Hagen, and T. Kibble, "Global Conservation Laws and Massless
1013 Particles", *Phys. Rev. Lett.* **13** (1964) 585, doi:10.1103/PhysRevLett.13.585.
- 1014 [7] P. W. Higgs, "Spontaneous Symmetry Breakdown without Massless Bosons", *Phys. Rev.*
1015 **145** (1966) 1156, doi:10.1103/PhysRev.145.1156.
- 1016 [8] T. Kibble, "Symmetry breaking in nonAbelian gauge theories", *Phys. Rev.* **155** (1967)
1017 1554, doi:10.1103/PhysRev.155.1554.
- 1018 [9] CMS Collaboration, "Precise determination of the mass of the Higgs boson and tests of
1019 compatibility of its couplings with the standard model predictions using proton
1020 collisions at 7 and 8 TeV", *Eur. Phys. J. C* **75** (2015) 212,
1021 doi:10.1140/epjc/s10052-015-3351-7, arXiv:1412.8662.
- 1022 [10] ATLAS Collaboration, "Measurements of the Higgs boson production and decay rates
1023 and coupling strengths using pp collision data at $\sqrt{s} = 7$ and 8 TeV in the ATLAS
1024 experiment", *Eur. Phys. J. C* **76** (2016) doi:10.1140/epjc/s10052-015-3769-y,
1025 arXiv:1507.04548.
- 1026 [11] ATLAS, CMS Collaboration, "Combined Measurement of the Higgs Boson Mass in pp
1027 Collisions at $\sqrt{s} = 7$ and 8 TeV with the ATLAS and CMS Experiments", *Phys. Rev. Lett.*
1028 **114** (2015) 191803, doi:10.1103/PhysRevLett.114.191803, arXiv:1503.07589.
- 1029 [12] CMS Collaboration, "Measurements of the Higgs boson production and decay rates and
1030 constraints on its couplings from a combined ATLAS and CMS analysis of the LHC pp
1031 collision data at $\sqrt{s} = 7$ and 8 TeV", CMS Physics Analysis Summary
1032 CMS-PAS-HIG-15-002, 2015.
- 1033 [13] CMS Collaboration, "Measurement of the properties of a Higgs boson in the four-lepton
1034 final state", *Phys. Rev. D* **89** (2014) 092007, doi:10.1103/PhysRevD.89.092007,
1035 arXiv:1312.5353.
- 1036 [14] CMS Collaboration, "Study of the Mass and Spin-Parity of the Higgs Boson Candidate
1037 via Its Decays to Z Boson Pairs", *Phys. Rev. Lett.* **110** (2013) 081803,
1038 doi:10.1103/PhysRevLett.110.081803, arXiv:1212.6639.

- [15] CMS Collaboration, “Constraints on the spin-parity and anomalous HVV couplings of the Higgs boson in proton collisions at 7 and 8 TeV”, *Phys. Rev. D* **92** (2015) 012004, doi:10.1103/PhysRevD.92.012004, arXiv:1411.3441.
- [16] CMS Collaboration, “Constraints on the Higgs boson width from off-shell production and decay to Z-boson pairs”, *Phys. Lett. B* **736** (2014) 64, doi:10.1016/j.physletb.2014.06.077, arXiv:1405.3455.
- [17] CMS Collaboration, “Limits on the Higgs boson lifetime and width from its decay to four charged leptons”, *Phys. Rev. D* **92** (2015) 072010, doi:10.1103/PhysRevD.92.072010, arXiv:1507.06656.
- [18] CMS Collaboration, “Measurement of differential and integrated fiducial cross sections for higgs boson production in the four-lepton decay channel in pp collisions at $\sqrt{s} = 7$ and 8 tev”, arXiv:1512.08377.
- [19] CMS Collaboration, “Measurements of properties of the higgs boson in the four-lepton final state at $\sqrt{s}=13$ tev with full run ii data”, CMS Physics Analysis Summary CMS-PAS-HIG-19-001, 2019.
- [20] PPD, “Ppd twiki for 2016 data and mc samples”, *CMS Twiki* (2018).
- [21] S. Alioli, P. Nason, C. Oleari, and E. Re, “NLO vector-boson production matched with shower in POWHEG”, *JHEP* **07** (2008) 060, doi:10.1088/1126-6708/2008/07/060, arXiv:0805.4802.
- [22] P. Nason, “A new method for combining NLO QCD with shower Monte Carlo algorithms”, *JHEP* **11** (2004) 040, doi:10.1088/1126-6708/2004/11/040, arXiv:hep-ph/0409146.
- [23] S. Frixione, P. Nason, and C. Oleari, “Matching NLO QCD computations with parton shower simulations: the POWHEG method”, *JHEP* **11** (2007) 070, doi:10.1088/1126-6708/2007/11/070, arXiv:0709.2092.
- [24] E. Bagnaschi, G. Degrassi, P. Slavich, and A. Vicini, “Higgs production via gluon fusion in the POWHEG approach in the SM and in the MSSM”, *JHEP* **02** (2012) 088, doi:10.1007/JHEP02(2012)088, arXiv:1111.2854.
- [25] P. Nason and C. Oleari, “NLO Higgs boson production via vector-boson fusion matched with shower in POWHEG”, *JHEP* **02** (2010) 037, doi:10.1007/JHEP02(2010)037, arXiv:0911.5299.
- [26] H. B. Hartanto, B. Jager, L. Reina, and D. Wackerlo, “Higgs boson production in association with top quarks in the POWHEG BOX”, *Phys. Rev. D* **91** (2015), no. 9, 094003, doi:10.1103/PhysRevD.91.094003, arXiv:1501.04498.
- [27] G. Luisoni, P. Nason, C. Oleari, and F. Tramontano, “ $H\bar{W}^\pm/HZ + 0$ and 1 jet at NLO with the POWHEG BOX interfaced to GoSam and their merging within MiNLO”, *JHEP* **10** (2013) 083, doi:10.1007/JHEP10(2013)083, arXiv:1306.2542.
- [28] Y. Gao et al., “Spin determination of single-produced resonances at hadron colliders”, *Phys. Rev. D* **81** (2010) 075022, doi:10.1103/PhysRevD.81.075022, arXiv:1001.3396. [Erratum: doi:10.1103/PhysRevD.81.079905].

- 1079 [29] NNPDF Collaboration, “Parton distributions for the LHC Run II”, *JHEP* **04** (2015) 040,
1080 doi:[10.1007/JHEP04\(2015\)040](https://doi.org/10.1007/JHEP04(2015)040), arXiv:[1410.8849](https://arxiv.org/abs/1410.8849).
- 1081 [30] P. Nason and G. Zanderighi, “ W^+W^- , WZ and ZZ production in the
1082 POWHEG-BOX-V2”, *Eur. Phys. J.* **C74** (2014), no. 1, 2702,
1083 doi:[10.1140/epjc/s10052-013-2702-5](https://doi.org/10.1140/epjc/s10052-013-2702-5), arXiv:[1311.1365](https://arxiv.org/abs/1311.1365).
- 1084 [31] J. M. Campbell and R. K. Ellis, “MCFM for the Tevatron and the LHC”, *Nucl. Phys. Proc. Suppl.* **205** (2010) 10, doi:[10.1016/j.nuclphysbps.2010.08.011](https://doi.org/10.1016/j.nuclphysbps.2010.08.011),
1085 arXiv:[1007.3492](https://arxiv.org/abs/1007.3492).
- 1087 [32] J. M. Campbell, R. K. Ellis, and C. Williams, “Bounding the Higgs width at the LHC
1088 using full analytic results for $gg \rightarrow e^-e^+\mu^-\mu^+$ ”, *JHEP* **04** (2014) 060,
1089 doi:[10.1007/JHEP04\(2014\)060](https://doi.org/10.1007/JHEP04(2014)060), arXiv:[1311.3589](https://arxiv.org/abs/1311.3589).
- 1090 [33] J. Alwall et al., “The automated computation of tree-level and next-to-leading order
1091 differential cross sections, and their matching to parton shower simulations”, *JHEP* **07**
1092 (2014) 079, doi:[10.1007/JHEP07\(2014\)079](https://doi.org/10.1007/JHEP07(2014)079), arXiv:[1405.0301](https://arxiv.org/abs/1405.0301).
- 1093 [34] CMS Collaboration, “Performance of electron reconstruction and selection with the CMS
1094 detector in proton-proton collisions at $\sqrt{s} = 8$ TeV”, *JINST* **10** (2015) P06005,
1095 doi:[10.1088/1748-0221/10/06/P06005](https://doi.org/10.1088/1748-0221/10/06/P06005).
- 1096 [35] CMS Collaboration, “Measurement of the properties of the higgs boson in the four-lepton
1097 final state at $\sqrt{s} = 13$ tev”, CMS Physics Analysis Note CMS-AN-15-277, 2016.
- 1098 [36] CMS Collaboration, “Measurement of the properties of the Higgs boson in the
1099 four-lepton final state at $\sqrt{s} = 13$ TeV”, CMS Physics Analysis Note CMS-AN-15-277,
1100 2016.
- 1101 [37] R. Salerno and M. Ahmad, “Measurements of properties of the Higgs boson in the
1102 four-lepton final state at $\sqrt{s}=13$ TeV”, *CMS AN* **2016/442** (2016).
- 1103 [38] T. Sculac and D. Sperka, “Measurements of properties of the Higgs boson in the
1104 four-lepton final state at $\sqrt{s}=13$ TeV with 2017 data”, *CMS AN* **2017/342** (2017).
- 1105 [39] CMS Collaboration, “New results on the study of higgs boson production in the
1106 four-lepton final state at $\sqrt{s} = 13$ tev”, CMS Physics Analysis Note CMS-AN-16-217, 2016.
- 1107 [40] E. Brondolin and G. Petrucciani, “Measurement of the muon-tracking efficiency using the
1108 tag and probe method on 2015 runii data”, *CMS AN* **2015/215** (2015).
- 1109 [41] JetMETPOG, “Jet id for 2018”, *CMS Twiki* (2018).
- 1110 [42] JetMETPOG, “Jet pu id for 2017”, *CMS Twiki* (2017).
- 1111 [43] JetMETPOG, “Jec mc for 2018”, *CMS Twiki* (2018).
- 1112 [44] PPD, “L1 pre-firing twiki recipe”, *CMS Twiki* (2018).
- 1113 [45] BTAGPOG, “B-tagging for 2018”, *CMS Twiki* (2018).
- 1114 [46] M. Grazzini, S. Kallweit, and D. Rathlev, “ ZZ production at the LHC: Fiducial cross
1115 sections and distributions in NNLO QCD”, *Phys. Lett. B* **750** (2015) 407 – 410,
1116 doi:<http://dx.doi.org/10.1016/j.physletb.2015.09.055>,
1117 arXiv:[1507.06257](https://arxiv.org/abs/1507.06257).

- [47] J. M. Campbell, R. K. Ellis, and C. Williams, “Vector boson pair production at the LHC”, *JHEP* **07** (2011) 018, doi:10.1007/JHEP07(2011)018, arXiv:1105.0020.
- [48] M. Bonvini et al., “Signal-background interference effects in $gg \rightarrow H \rightarrow WW$ beyond leading order”, *Phys. Rev. D* **88** (2013) 034032, doi:10.1103/PhysRevD.88.034032, arXiv:1304.3053.
- [49] K. Melnikov and M. Dowling, “Production of two Z-bosons in gluon fusion in the heavy top quark approximation”, *Phys. Lett. B* **744** (2015) 43, doi:10.1016/j.physletb.2015.03.030, arXiv:1503.01274.
- [50] C. S. Li, H. T. Li, D. Y. Shao, and J. Wang, “Soft gluon resummation in the signal-background interference process of $gg(\rightarrow h^*) \rightarrow ZZ$ ”, (2015). arXiv:1504.02388.
- [51] G. Passarino, “Higgs CAT”, *Eur. Phys. J. C* **74** (2014) 2866, doi:10.1140/epjc/s10052-014-2866-7, arXiv:1312.2397.
- [52] S. Catani and M. Grazzini, “An NNLO subtraction formalism in hadron collisions and its application to Higgs boson production at the LHC”, *Phys. Rev. Lett.* **98** (2007) 222002, doi:10.1103/PhysRevLett.98.222002, arXiv:hep-ph/0703012.
- [53] M. Grazzini, “NNLO predictions for the Higgs boson signal in the $H \rightarrow WW \rightarrow l\nu l\nu$ and $H \rightarrow ZZ \rightarrow 4l$ decay channels”, *JHEP* **02** (2008) 043, doi:10.1088/1126-6708/2008/02/043, arXiv:0801.3232.
- [54] M. Grazzini and H. Sargsyan, “Heavy-quark mass effects in Higgs boson production at the LHC”, *JHEP* **09** (2013) 129, doi:10.1007/JHEP09(2013)129, arXiv:1306.4581.
- [55] LHC Higgs Cross Section Working Group, “Handbook of LHC Higgs Cross Sections: 3. Higgs Properties”, CERN Report CERN-2013-004, 2013. doi:10.5170/CERN-2013-004, arXiv:1307.1347.
- [56] HZZ, “Higgs boson transverse momentum in powheg and hres”, *CMS meeting* (2015).
- [57] ATLAS and CMS Collaborations, LHC Higgs Combination Group, “Procedure for the lhc higgs boson search combination in summer 2011”, ATL-PHYS-PUB/CMS NOTE 2011-11, 2011/005, CERN, 2011.
- [58] G. Cowan, K. Cranmer, E. Gross, and O. Vitells, “Asymptotic formulae for likelihood-based tests of new physics”, *Eur. Phys. J. C* **71** (2011) 1554, doi:10.1140/epjc/s10052-011-1554-0, 10.1140/epjc/s10052-013-2501-z, arXiv:1007.1727.
- [59] CMS Collaboration, “Measurement of differential cross sections for Higgs boson production in the diphoton decay channel in pp collisions at $\sqrt{s}=8$ TeV”, *Eur. Phys. J. C* **76** (2015) 13, doi:10.1140/epjc/s10052-015-3853-3, arXiv:1508.07819.